





20456912



This is to certify that the  
thesis entitled  
COMBUSTION AND MASS TRANSFER CHARACTERISTICS OF  
LARGE CARBON PARTICLES IN THE GRID REGION  
OF A FLUIDIZED BED COMBUSTOR

presented by

Alexander Seung Choi

has been accepted towards fulfillment  
of the requirements for

Ph.D. degree in Chemical Engineering

  
Major professor

Date April 14, 1988





**RETURNING MATERIALS:**  
Place in book drop to  
remove this checkout from  
your record. FINES will  
be charged if book is  
returned after the date  
stamped below.

--	--	--

COMBUSTION AND MASS TRANSFER CHARACTERISTICS  
OF LARGE CARBON PARTICLES IN THE GRID REGION  
OF A FLUIDIZED BED COMBUSTOR

By

Alexander Seung Choi

A DISSERTATION

Submitted to  
Michigan State University  
in partial fulfillment of the requirements  
for the degree of

DOCTOR OF PHILOSOPHY

Department of Chemical Engineering

1988

2177261

ABSTRACT

COMBUSTION AND MASS TRANSFER CHARACTERISTICS  
OF LARGE CARBON PARTICLES IN THE GRID REGION  
OF A FLUIDIZED BED COMBUSTOR

By

Alexander Seung Choi

A fluidized bed coal combustor is a diluted system in which each burning coal particle is surrounded by many inert bed particles due to its low concentration in the bed. These inert particles present a major resistance to oxygen transfer. Most studies on mass transfer have been for the bubbling region; this study characterizes combustion and mass transfer phenomena in the grid region near the multi-orifice gas distributor where the gas and solids contacting is more efficient.

Single particle experiments measure the combustion rates of large electrode graphite spheres fixed at various positions within the grid region. The results show that the relative importance between mass transfer and chemical kinetics in the overall combustion depend strongly on all operating variables considered such as inert particle size, superficial gas velocity and, most importantly, particle position. Inert particle size is found to determine the rate of gas

leakage into the dense phase as well as the voidage distribution in the dilute phase.

Based on the new definition of the grid region height determined from the reaction point of view, the experimental results are analyzed in light of theories for spouted beds and two-phase flows, and mass transfer correlations are proposed for oxygen transfer in the grid region. The results of theoretical analyses further suggest that a different description of the overall combustion phenomena is needed in the grid region. This description could be combined with some of the bubbling bed models for better prediction of the overall bed performance.

Copyright

by

**Alexander Seung Choi**

1988

To my parents

**Howard C. and Hye Ran Choi**

## **ACKNOWLEDGEMENTS**

I would like to express my deep gratitude to my academic advisor, Professor Martin C. Hawley, for his insight, encouragement, and financial support. I would also like to thank Dr. Anderson for his continued support throughout my stay at Michigan State. Many thanks are due to Dr. Petty, Dr. Jayaraman, Dr. Miller and Dr. Yen for their helpful suggestions. I greatly appreciate the dedicated effort and patience of Dr. Hye Kyung Kim for typing this manuscript. Finally, I am greatly indebted to my family: without their help and support, I would not have been able to finish my education.

## TABLE OF CONTENTS

List of Tables	ix
List of Figures	x
Symbols	xiii
CHAPTER 1: GRID REGION PHENOMENA IN A FLUIDIZED BED AND OBJECTIVES OF THE RESEARCH.	1
1-1. Introduction	2
1-2. Review of Grid Region Phenomena	4
1-2-1. Experimental observations of gas and solids flows in the grid region	5
1-2-2. Development of grid region models	12
1-3. Objectives of the Reserch	17
CHAPTER 2: SINGLE PARTICLE COMBUSTION OF ELECTRODE GRAPHITE SPHERES IN THE GRID REGION OF A FLUIDIZED BED COMBUSTOR	18
2-1. Introduction	19
2-2. Combustion Characteristics of Carbon in a Fluidized Bed Combustor	21
2-3. Definition of the Grid Region	25
2-4. Single Particle Experiments	28
2-4-1. Experimental equipments	28
2-4-2. Experimental procedures	32
2-5. Estimation of Minimum Fluidization Velocities	37
2-6. Experimental Results and Discussion	39
2-6-1. Mode of combustion	39
2-6-2. Estimation of the grid region height	47
2-6-3. Mass transfer characteristics of fixed carbon samples	67
2-6-4. Effects of superficial air velocity on $R_c A$ and $Sh$	73
2-6-5. Effects of inert particle size on $R_c A$ and $Sh$	83
2-6-6. Vertical profiles of mass transfer resistance	89
CHAPTER 3: THEORETICAL ANALYSIS OF MASS TRANSFER CHARACTERISTICS IN THE GRID REGION OF A FLUIDIZED BED COMBUSTOR	94
3-1. Introduction	95
3-2. Review of Studies in Multiparticle-Fluid Systems	
3-2-1. Background	95
3-2-2. Studies on the mechanism of mass transfer in a fluidized bed combustor	96
3-2-3. Studies on the mechanism of mass transfer in other multi-particle fluid systems	100
3-3. Development of Mass Transfer Correlations in the Grid	

	<b>Region</b>	
	3-3-1. Formulation of the problem of mass transfer in a diluted system	103
	3-3-2. Analogy between the grid region and a spouted bed	106
	3-3-3. Axial voidage distributions in the grid region	108
	3-3-4. Axial velocity distributions in the grid region	118
	3-3-5. Development of mass transfer correlations	123
	3-3-6. Discussion	131
3-4.	Estimation of the Dead Zone Height	134
<b>CHAPTER 4:</b>	<b>SUMMARY OF CONCLUSIONS AND SUGGESTIONS FOR FUTURE RESEARCH</b>	<b>138</b>
4-1.	Summary of Conclusions	139
	4-1-1. Conclusions on single particle experiments	140
	4-1-2. Conclusions on the theoretical analyses	142
4-2.	Suggestions for Future Research	144
<b>Appendix</b>		
A-1.	Design of Gas Distributors	147
A-2.	Sample Calculations	
	A-2-1. Particle terminal velocity	149
	A-2-2. Calculation of $\epsilon$ and $u$	150
	A-2-3. Calculation of $R_c$ , $\phi$ and $Sh$	153
A-3.	Experimental Data	156
<b>References</b>		<b>171</b>

## List of Tables

Table 2.1	Physical properties of bed materials	30
Table 2.2	Experimental conditions for single particle combustion of electrode graphite spheres in air at 1163 K and 1 atm	36
Table 2.3	Kinetic and physical data for mass transfer calculations	40
Table 2.4	Comparisons of grid region height with jet penetration length ( $d_s = 460 \mu\text{m}$ , $T_B = 1163 \text{ K}$ )	50
Table 2.5	Experimental grid region height at 1163 K	51
Table 3.1	Values of the parameters used in the calculation of $I_0$  $\rho_p = 2,700 \text{ kg/m}^3$ , $\rho_f = 0.3892 \text{ kg/m}^3$ , $D_o = 6.35 \text{ mm}$	113
Table 3.2	Mean bed voidage calculated from Eq. (3.20) and (3.21)	115
Table 3.3	Estimated values of the dead zone height	136
Table A.1	Experimental results (Run # 1)	156
Table A.2	Experimental results (Run # 2)	156
Table A.3	Experimental results (Run # 3)	157
Table A.4	Experimental results (Run # 4)	157
Table A.5	Experimental results (Run # 5)	158
Table A.6	Experimental results (Run # 6)	158
Table A.7	Experimental results (Run # 7)	159
Table A.8	Experimental results (Run # 8)	159
Table A.9	Experimental results (Run # 9)	160
Table A.10	Experimental results (Run # 10)	160
Table A.11	Experimental results (Run # 11)	161
Table A.12	Experimental results (Run # 12)	161
Table A.13	Experimental results (Run # 13)	162
Table A.14	Experimental results (Run # 14)	162
Table A.15	Experimental results (Run # 15)	163
Table A.16	Experimental results (Run # 16)	163
Table A.17	Experimental results (Run # 17)	164
Table A.18	Experimental results (Run # 18)	164
Table A.19	Experimental results (Run # 19)	165
Table A.20	Experimental results (Run # 20)	165
Table A.21	Experimental results (Run # 21)	166
Table A.22	Experimental results (Run # 22)	166
Table A.23	Experimental results (Run # 23)	167
Table A.24	Experimental results (Run # 24)	167
Table A.25	Experimental results (Run # 25)	168
Table A.26	Experimental results (Run # 26)	168
Table A.27	Experimental results (Run # 27)	169
Table A.28	Experimental results (Run # 28)	169
Table A.29	Experimental results (Run # 29)	170

## List of Figures

Fig. 1.1	Behavior of particles above an orifice: (a),(b) radial profile, (c) vertical profile, from Oki et al. (15).	8
Fig. 2.1	A coal particle burning in the particulate phase of the bubbling region, from La Nauze (34).	20
Fig. 2.2	A schematic sketch of the grid region: (A) dead zone, (B) quasi-dead zone, (C) zone of sluggish particle motion.	27
Fig. 2.3	Experimental fluidized bed unit.	31
Fig. 2.4	Multi-orifice gas distributor used in the study.	32
Fig. 2.5	Fraction of initial diameter and the ratio of densities versus fractional burn-off ( $U_o = 16.6$ m/s, $d_s = 460$ $\mu$ m).	43
Fig. 2.6	Apparent carbon density versus carbon diameter during burn-off ( $U_o = 16.6$ m/s, $d_s = 460$ $\mu$ m).	44
Fig. 2.7	Variations in the Sherwood number and degree of mass transfer control, $\phi$ , with particle diameter during burn-off ( $U_o = 16.6$ m/s, $d_s = 460$ $\mu$ m).	45
Fig. 2.8	Overall combustion rate versus particle diameter for a freely moving graphite sphere ( $U_o = 16.6$ m/s, $d_s = 460$ $\mu$ m).	46
Fig. 2.9	Overall combustion rate versus particle diameter ( $U_o = 22.6$ m/s, $d_s = 620$ $\mu$ m, $z = 1$ inch, $U = 2 U_{mf}$ ).	52
Fig. 2.10	Overall combustion rate versus particle diameter ( $U_o = 22.6$ m/s, $d_s = 620$ $\mu$ m, $z = 2$ inch, $U = 2 U_{mf}$ ).	53
Fig. 2.11	Overall combustion rate versus particle diameter ( $U_o = 22.6$ m/s, $d_s = 620$ $\mu$ m, $z = 3.5$ inch, $U = 2 U_{mf}$ ).	54
Fig. 2.12	Effect of particle position on overall combustion rate ( $U_o = 22.6$ m/s, $d_s = 620$ $\mu$ m, $z = 1, 2, 3.5$ inch, $U = 2 U_{mf}$ ).	55
Fig. 2.13	Overall combustion rate versus particle diameter ( $U_o = 33.8$ m/s, $d_s = 620$ $\mu$ m, $U = 3 U_{mf}$ ).	56
Fig. 2.14	Overall combustion rate versus particle diameter ( $U_o = 45.2$ m/s, $d_s = 620$ $\mu$ m, $U = 4 U_{mf}$ ).	57
Fig. 2.15	Overall combustion rate versus particle diameter ( $U_o = 9.4$ m/s, $d_s = 460$ $\mu$ m, $U = 1.5 U_{mf}$ ).	58
Fig. 2.16	Overall combustion rate versus particle diameter ( $U_o = 12.5$ m/s, $d_s = 460$ $\mu$ m, $z = 1, 3$ inch $U = 1.5 U_{mf}$ ).	59
Fig. 2.17	Overall combustion rate versus particle diameter ( $U_o = 25.0$ m/s, $d_s = 460$ $\mu$ m, $z = 1, 2.25$ inch $U = 4 U_{mf}$ ).	60
Fig. 2.18	Overall combustion rate versus particle diameter ( $U_o = 4.7$ m/s, $d_s = 230$ $\mu$ m, $z = 1, 3$ inch $U = 3 U_{mf}$ ).	61
Fig. 2.19	Overall combustion rate versus particle diameter ( $U_o = 9.4$ m/s, $d_s = 230$ $\mu$ m, $z = 1, 2.25$ inch $U = 6 U_{mf}$ ).	62

Fig. 2.20	Ratio of grid region height to pitch size versus $U/U_{mf}$ , $d_s = 230 \mu\text{m}$ .	63
Fig. 2.21	Ratio of grid region height to pitch size versus $U/U_{mf}$ , $d_s = 460 \mu\text{m}$ .	64
Fig. 2.22	Ratio of grid region height to pitch size versus $U/U_{mf}$ , $d_s = 620 \mu\text{m}$ .	65
Fig. 2.23	Effect of particle position on overall combustion rate in the bubbling region ( $U_o = 25.0 \text{ m/s}$ , $d_s = 460 \mu\text{m}$ , $U = 4 U_{mf}$ ).	66
Fig. 2.24	Variations in Sherwood number with particle diameter ( $U_o = 22.6 \text{ m/s}$ , $d_s = 620 \mu\text{m}$ , $z = 1 \text{ inch}$ , $U = 2 U_{mf}$ ).	68
Fig. 2.25	Variations in Sherwood number with particle diameter ( $U_o = 22.6 \text{ m/s}$ , $d_s = 620 \mu\text{m}$ , $z = 2 \text{ inch}$ , $U = 2 U_{mf}$ ).	69
Fig. 2.26	Variations in Sherwood number with particle diameter ( $U_o = 22.6 \text{ m/s}$ , $d_s = 620 \mu\text{m}$ , $z = 3.5 \text{ inch}$ , $U = 2 U_{mf}$ ).	70
Fig. 2.27	Effect of particle position on Sherwood number ( $U_o = 25.0 \text{ m/s}$ , $d_s = 460 \mu\text{m}$ , $u = 4 U_{mf}$ ).	71
Fig. 2.28	Effect of particle position on Sherwood number above grid region height ( $U_o = 25.0 \text{ m/s}$ , $d_s = 460 \mu\text{m}$ , $z = 2.25, 3, 4 \text{ inch}$ , $u = 4 U_{mf}$ ).	72
Fig. 2.29	Effect of $U$ on overall combustion rate ( $d_s = 620 \mu\text{m}$ , $z = 1 \text{ inch}$ , $u = 2, 3, 4 U_{mf}$ ).	76
Fig. 2.30	Effect of $U$ on the Sherwood number in the dilute phase ( $d_s = 620 \mu\text{m}$ , $z = 1 \text{ inch}$ , $U = 2, 3, 4 U_{mf}$ ).	77
Fig. 2.31	Temperature rise above bed temperature ( $d_s = 620 \mu\text{m}$ , $z = 1 \text{ inch}$ , $U = 2, 3, 4 U_{mf}$ ).	78
Fig. 2.32	Effect of $U$ on the Sherwood number in the dense phase ( $d_s = 620 \mu\text{m}$ , $z = 1 \text{ inch}$ , $U = 2, 3, 4 U_{mf}$ ).	79
Fig. 2.33	Effect of $U$ on the Sherwood number ( $d_s = 230 \mu\text{m}$ , $z = 1 \text{ inch}$ , $U = 3, 4, 6 U_{mf}$ ).	80
Fig. 2.34	Effect of $U$ on the Sherwood number in the dilute phase ( $d_s = 460 \mu\text{m}$ , $z = 1.5 \text{ inch}$ , $U = 1, 2, 4 U_{mf}$ ).	81
Fig. 2.35	Effect of $U$ on the Sherwood number in the dense phase ( $d_s = 460 \mu\text{m}$ , $z = 1 \text{ inch}$ , $U = 1.5, 2, 4 U_{mf}$ ).	82
Fig. 2.36	Effect of inert particle size on overall combustion rate ( $d_s = 230, 460 \mu\text{m}$ , $z = 1 \text{ inch}$ , $U_o = 11 \text{ cm/s}$ ).	85
Fig. 2.37	Effect of inert particle size on the Sherwood number	

	( $d_s = 230, 460 \mu\text{m}$ , $z = 1 \text{ inch}$ , $U_o = 11 \text{ cm/s}$ ).	86
Fig. 2.38	Effect of inert particle size on the Sherwood number in the dilute phase ( $d_s = 230, 460, 620 \mu\text{m}$ , $z = 1 \text{ inch}$ , $U = 4 U_{mf}$ ).	87
Fig. 2.39	Effect of inert particle size on the Sherwood number in the dense phase ( $d_s = 230, 460, 620 \mu\text{m}$ , $z = 1 \text{ inch}$ , $U = 4 U_{mf}$ ).	88
Fig. 2.40	Variations in the Sherwood number along the vertical distance in the dilute phase ( $d_s = 620 \mu\text{m}$ , $z = 1, 2 \text{ inch}$ , $U = 4 U_{mf}$ ).	91
Fig. 2.41	Variations in the Sherwood number along the vertical distance in the dilute phase ( $d_s = 230 \mu\text{m}$ , $z = 1, 2, 2.25 \text{ inch}$ , $U = 6 U_{mf}$ ).	92
Fig. 2.42	Variations in the Sherwood number along the vertical distance in the dense phase ( $d_s = 620 \mu\text{m}$ , $z = 1, 2, 3.5 \text{ inch}$ , $U = 2 U_{mf}$ ).	93
Fig. 3.1	Spouted bed model as applied to the grid region ( , solids flow; +, gas flow).	107
Fig. 3.2	Axial voidage distribution in the dilute phase calculated from Eqs. (3.13) and (3.19).	117
Fig. 3.3	Axial velocity distribution in the dilute phase at $U = 4 U_{mf}$ .	122
Fig. 3.4	Plot of $\ln[(Sh - 2\epsilon)/Sc^{1/3}]$ versus $\ln Re$ in the dilute phase for $0 \leq z < h_e$ .	127
Fig. 3.5	Plot of $\ln[(Sh - 2\epsilon)/Sc^{1/3}]$ versus $\ln Re$ in the dilute phase for $h_e \leq z \leq H$ .	128
Fig. 3.6	Plot of $\ln[(Sh - 2\epsilon)/Sc^{1/3}]$ versus $\ln Re$ in the dense phase for $0 < z \leq H$ .	129
Fig. 3.7	Plot of $\ln[(Sh - 2\epsilon)/Sc^{1/3}]$ versus $\ln Re$ (dilute phase (open symbol), dense phase (closed symbol)).	130
Fig. 3.8	Mass transfer factor versus Reynolds number in a diluted system.	133
Fig. 3.9	Axial velocity distribution in the dense phase at $U = 4 U_{mf}$ .	137
Fig. 4.1	Research plan for the overall combustion modeling.	146

## Symbols

A	external surface area of a carbon particle
$A_o$	preexponential factor, $\text{kgC/m}^2 \text{ s atm}$
Ar	Archimedes number, defined as $d_s^3 \rho_f (\rho_s - \rho_f) g / \mu_f^2$
$C_{Ab}$	concentration of reactant A at the exit of the grid region, moles/liter
$C_{Ao}$	concentration of reactant A entering the bed moles/liter
$C_d$	drag coefficient defined in Eq. (A.7)
$C_D$	orifice discharge coefficient
$C_o$	oxygen concentration entering the bed, $\text{kg/m}^3$
$C_p$	oxygen concentration in the particulate phase, $\text{kg/m}^3$
$C_s$	oxygen concentration at the surface of carbon, $\text{kg/m}^3$
$D_c$	equivalent diameter of a spouted bed, m
$D_g$	diffusivity of oxygen in air, $\text{m}^2/\text{s}$
$D_j$	jet diameter, m
$d_m$	particle moving zone diameter, m
$D_o$	orifice diameter, m
$d_p$	diameter of a carbon or active particle, m
$d_s$	mean diameter of inert particles, m
$E_a$	activation energy of reaction, kcal/mole
g	gravitational acceleration = $9.8 \text{ m/s}^2$
h	jet height, m
$\Delta H$	heat of reaction, kJ/kgC
$H_B$	Bed height, m
$h_d$	dead zone height, m
$h_e$	height of entrance effects, m
H	grid region height, m
$H_{ms}$	maximum spoutable bed depth, m
$I_o - I_2$	constants used in Eqs. (3.12)-(3.16)
$j_D$	mass transfer factor, defined as $k_m Sc^{2/3}/U$
K	fraction of gas visible as bubbles
$k_c$	apparent chemical rate coefficient, $\text{kg C/m}^2 \text{ s atm}$

$k_m$	external mass transfer coefficient, m/s
$k_s$	first-order rate constant, $s^{-1}$
$k_b a_b$	mass transfer coefficient per unit volume of reactor in the bubbling region, $kg/m^3 s$
$k_j a_j$	mass transfer coefficient per unit volume of reactor in the jet region, $kg/m^3 s$
$L, L_{max}$	jet penetration length, m
$L_d$	catalyst loading in the particulate phase, $m^3/m^3$ particulate phase
$L_D$	distributor thickness
$m$	exponent in Eq. (3.20)
$n$	apparent reaction order
$N_b$	bubble frequency, $s^{-1}$
$Pe$	Péclet number, defined as $d_p U/D_g$
$Q_b$	mass flow through bubbles, kg/s
$Q_d$	mass flow through the particulate phase, kg/s
$R$	gas constants = 1.987 cal/g mole K
$R(y_\infty)$	reaction rate per unit weight of catalyst in the particulate phase, kg/s kg
$R_c$	reaction rate per unit external surface area of carbon, $kg/m^2 s$
$Re$	Reynolds number, defined as $\rho_f u d/\mu_f$
$S$	pitch size, m
$Sc$	Schmidt number, defined as $\mu_f/\rho_f D_g$
$Sh$	Sherwood number, defined as $k_m d_p/D_g$
$t$	time, s
$t_e$	time taken for a bubble to form completely, s
$T_p$	particle temperature, K
$U$	superficial gas velocity, m/s
$u_j$	interstitial gas velocity in the dilute phase, m/s
$U_L$	superficial velocity of gas leakage, m/s
$u_R$	relative velocity between gas and solids, m/s
$u_t$	particle terminal velocity, m/s
$V_b$	bubble volume, $m^3$

$V_d$	volume of the particulate phase, $m^3$
$v_j$	particle velocity in the dilute phase, m/s
$\Delta W$	weight loss, kg
$y_b, y_\infty$	mass fraction of reactant in the bubble and particulate phase, respectively.
$z$	axial coordinate, m
$z_b$	distance travelled by bubbles prior to coalescence, m

#### Greek letters

$\beta$	stoichiometric coefficient
$\delta$	gas-solids interphase drag coefficient, defined in Eqs. (3.7) and (3.8)
$\epsilon$	voidage
$\epsilon_b$	mean bed voidage
$\zeta$	dimensionless axial coordinate, $z/H$
$\theta_r$	angle of repose
$\lambda$	constant in Eq. (3.12)
$\mu_f$	gas viscosity
$\xi$	ratio of average channeling length to particulate diameter
$\rho$	density
$\phi$	degree of mass transfer control
$\psi_s$	particle shape factor

#### Subscripts

b	bubble
B	bed
d	dense phase
D	distributor
exp	experimental
f	gas or fluid
j	dilute phase
mf	minimum fluidization
ms	minimum spouting
o	orifice
p	active particle
s	inert particle

**CHAPTER 1**

**GRID REGION PHENOMENA IN A FLUIDIZED BED**

**AND OBJECTIVES OF THE RESEARCH**

## 1-1. Introduction

Fluidized bed coal combustion provides one option for utilizing coal for purpose of energy generation. A major contributing factor to the success of fluidized bed coal combustion technology is the ability of fluidized beds to handle coals of widely varying composition, including low grade coals with high ash content, compared with other contacting devices such as stoker and pulverized coal firing. Fluidized bed combustion also provides a capability of in-bed sulfur capture, which is an important factor from the standpoint of stringent environmental pollution standards imposed by government legislation and regulation. Another important advantage of fluidized bed combustion is its excellent heat and mass transfer rates due to vigorous gas and solids mixing to increase the efficiency of combustion considerably. Especially, gas and solids contacting is known to be more efficient in the grid region near the distributor than higher up in gas fluidized beds so that for fast reactions much of the conversion may take place in this narrow region. As a result, the temperature gradient in the grid region can be quite high, and the presence of stagnant zones near the distributor can cause hot spots resulting in solids agglomeration, gas entry point blockage, and eventual reactor failure in such applications as fluidized bed coal gasification, coal combustion, and exothermic catalytic reactions (1).

For example, industrial pilot plant experiments performed by Cooke et al. (2) in a 1.2 m diameter bed have shown that up to 90 % of the conversion in coal carbonization can take place in the first half meter

of bed height. Cole and Essenhigh (3) also observed that the gas temperature increased from 150°F to 1900°F within 1 inch from the bottom in a fluidized bed coal combustor.

It is also this region that determines the distinct size, shape and frequency of bubbles which in turn affect the overall hydrodynamics, uniformity, and stability of the bed. Therefore, not only from the standpoint of design and scale-up of gas distributor systems but from the important effects of the grid region on the physical and chemical performance of the bed, it is of considerable practical interest to understand correctly how the gas flow through the orifice enters the bed and how it induces such high rates of heat and mass transfer before it is fully established as bubbles and interstitial gas flow (4).

Unlike many other fluidized bed applications of commercial interest, one distinct feature of fluidized bed coal combustion is that not all particles in the bed are active; each burning coal particle in a fluidized bed coal combustor is virtually surrounded by many inert bed particles due to its low concentration in the bed. The shielding effect by these inerts represents a major resistance to the mass transfer of oxygen to the burning carbon particles, which has been the focus of many intensive studies in the past decade. Despite the importance of the grid region on the overall performance of the bed as described above, most studies on mass transfer and reactor modeling, however, have been made exclusively in the bubbling region (5,6,7,8,9,10,11) and there appears to be little work reported in the

literature which focuses its attention on the investigation of high mass transfer rates in the grid region of a fluidized bed combustor.

Considering the fact that many existing bubbling bed models available in the literature may not be used to accurately predict the overall performance of the entire bed without taking into consideration the combustion characteristics in the grid region, it is believed that there is a need for better understanding the grid region whose hydrodynamic as well as thermal features are markedly different from those in the bubbling region.

This research is, therefore, directed toward investigating combustion and mass transfer characteristics of large carbon particles in the grid region of a fluidized bed combustor, which is of crucial importance in combustion modeling studies.

## 1-2. Review of Grid Region Phenomena in a Fluidized Bed

For the purpose of modeling a fluidized bed reactor, one can conveniently divide the bed into two hydrodynamically distinct regions, the bubbling and the grid region. Except for shallow beds, the bubbling region usually occupies much of the reactor volume, and the overall bed uniformity is maintained by vigorous gas and solids mixing induced by fast rising bubbles. However, the increase in bubble size due to coalescence leads to significant gas by-passing and considerable lowering of the reactor performance, particularly with deep beds. On the other hand, hydrodynamics and transport processes in the grid region are far from completely understood due to their complexity, and

this section discusses some of the important features of gas and solids flows and the modeling studies in the grid region near the multiorifice gas distributor.

1-2-1. Experimental observations of gas and solids flows in the grid region

The mode of gas entry through the discrete grid holes into gas fluidized beds has been considered by many to be always in the form of discrete gas jets or spouts with bubbles detaching from the ends of these jets or spouts (12,13,14), as shown in Figure 2.2. Recently, Rowe et al. (4) found from their x-ray study in a three-dimensional bed that gas issuing from the orifice entered the bed in the form of bubbles, instead of a permanent flame-like jet, at sufficiently high gas flow rates. They also found that it was possible to establish a jet when the particles were not fluidized locally and when there were surfaces present to hinder the flow of particles toward the orifice. These findings were later confirmed by others (15,16). Besides the degree of bed fluidization and the presence of surfaces, particle size and particle density are also known to affect the development of gas jets. For a given inlet gas velocity at the orifice, the mode of gas discharge gradually changes from the chain of bubbles to the jet type, as bed particle size increases from fine powders (Geldart Group A) to coarse beads (Geldart Group D) (17).

Regardless of whether a jet or bubbles are formed at the orifice, depending on the presence of the dead zone, recent experimental results further showed that a considerable amount of gas leaks from the void to

the dense phase at the entry point. Yates et al. (18) observed that only about one third of the gas flow entering the bed was visible as bubbles, leading to significant deviations from the classical two-phase theory of fluidization (19) in the lower region of the bed. They concluded that such high rates of gas leakage from a bubble during formation caused the dense phase voidage to increase above its minimum fluidization value, which resulted in good contacting between gas and solid particles and, therefore, high rates of heat and mass transfer. Wen et al. (16) further proposed a mechanism for the formation of jets and bubbles; gas entering a fluidized bed through orifices disperses partially through the bubble or jet boundary to fluidize the entire bed, and bubbles form only at a height where the cumulative leakage is complete and the bed is completely fluidized. In the case of large pitches and small orifice diameters, this condition occurs only above a certain height, and consequently a spout of gas is formed from which bubbles take off (16).

A common way of experimentally measuring the amount of gas leakage is to plot the observed bubble volumes against the ratio of inlet gas flow rate to the frequency of bubble formation which gives rise to a reasonably linear relationship as:

$$V_b = K \frac{Q_o}{N_b} \quad (1.1)$$

K is a proportionality constant which represents the fraction of entering gas visible as bubbles. The value of K depends on the

operating conditions, and reported values at the orifice are usually less than 0.5. One significant outcome of this experimental technique is that it can give an estimate of the grid region height by experimentally observing the distance from the distributor where the value of  $K$  satisfies the distribution of gas flow between bubbles and interstitial flow according to the two-phase theory (19).

Oki et al. (15) measured the averaged local upward particle velocities at various heights above the center orifice of three different types of multi-orifice distributors by using a fiber optic probe. They showed that particles initially accelerated to their maximum velocities beyond which the velocities decreased to the limiting values, which might be related to the velocities of ascending bubbles, as shown in Figure 1.1 (c). It seems to be reasonable to assume that the height of constant upward particle velocity corresponds to the grid region height measured from the hydrodynamic point of view, and it will be interesting to compare with the height where the value of  $K$  satisfies the two-phase theory. It can also be seen from Figure 1.1 (c) that for the same air velocity, the maximum particle velocity as well as the vertical velocity profile for the distributor which has a larger pitch size are considerably different from those with smaller pitch sizes.

In view of current interest in combustion and gasification of coal in fluidized beds, Ghadiri and Clift (20) measured jet penetration length by noting the erosion marks on the wall of an air-fluidized bed of sand at  $800^{\circ}\text{C}$ , and found that all correlations at ambient conditions

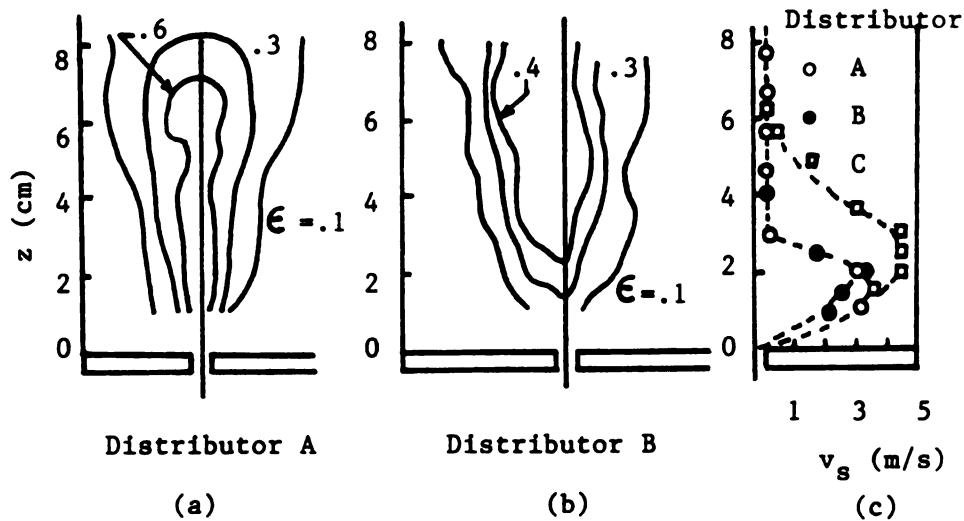


Fig. 1.1 Behavior of particles above an orifice: (a),(b) radial profile, (c) vertical profile, from Oki et al. (15).

except that of Merry (14) grossly overpredicted jet penetration length under their experimental conditions. They further argued that since the particle motion is very rapid in the vicinity of a developing bubble chain at the tip of a jet, wall erosion may occur beyond the point at which the jet degenerates into bubbles. Since a distribution orifice should be located close to the wall in order to have distinct erosion marks, it seems that the experimental technique employed by Ghadiri and Clift (20) might have overpredicted jet penetration length due to wall effects. However, one significant outcome of their experiment is that correlations for jet penetration length at ambient conditions cannot reliably be extended for use at much higher temperatures, and this is particularly true when there is a reaction involved in the grid region. An extensive survey of jet penetration length studies and correlations is made by Massimila (17), and some of

the widely used correlations for jet penetration length are given below.

Merry (14):

$$\frac{L}{D_o} = 5.2 \left( \frac{\rho_f D_o}{\rho_s d_s} \right)^{0.3} \left[ 1.3 \left( \frac{U_o^2}{g D_o} \right)^{0.2} - 1 \right] \quad (1.2)$$

Yang and Keairns (21):

$$\frac{L}{D_o} = 15.0 \left( \frac{\rho_f}{\rho_s - \rho_f} \frac{U_o^2}{g D_o} \right)^{0.187} \quad (1.3)$$

Wen et al. (22) :

$$\frac{L}{D_o} = 814.2 \left( \frac{\rho_s d_s}{\rho_f D_o} \right)^{-0.585} \left( \frac{\rho_f D_o U_o}{\mu_f} \right)^{-0.654} \left( \frac{U_o^2}{g D_o} \right)^{0.47} \quad (1.4)$$

Zenz (55):

$$0.0144 \frac{L_{\max}}{D_o} + 1.3 = 0.5 \log (\rho_f U_o^2) \quad (1.5)$$

where  $L$  is jet penetration length,  $D_o$  orifice diameter,  $U_o$  mean gas velocity at the orifice,  $\mu_f$  gas viscosity,  $d_s$  particle diameter, and  $\rho_f$  and  $\rho_s$  are gas and solids densities, respectively.

The experimental measurement of the grid region height is also possible with the use of a highly sensitive temperature measuring device. Fan et al. (23) measured the transient axial particle and gas temperature profiles near the distributor in a three-dimensional gas fluidized bed by means of suction and bare thermocouples. They found from the analysis of experimental results at temperatures not higher than  $100^\circ\text{C}$  that the height required for the temperature of gas and particles to be equalized is approximately the height of jet penetration defined as the length of jet before breaking up into bubbles. They also found that the particle temperature rose rapidly near the distributor to a maximum, due to the existence of the dead zone, while the grid region height decreased as the gas flow rate increased. The key assumptions made in their analysis were that the region between the adjacent grid holes was so packed with particles that a bare thermocouple would come into close and direct contact with relatively immobile particles at all times and that the jetting region was free of solids.

It is, however, known that particles are indeed entrained into the voids formed above the orifice (24), which in turn results in the modification of the streamlines for the fluidizing fluid. Considering the statistical nature of jetting phenomena, Oki et al. (15) obtained the time averages of jet lengths in terms of void fractions with the

use of an optical-fiber array probe. They found that the jet boundary was diffusive in nature; the change in solids concentration was gradual over the whole radial dimensions of the jet, as shown in Figure 1.1 (a) and (b). Their results clearly show that a significant amount of solids are present even in the core of the jet and that solids occupy almost 90 % of the jet volume at the boundary if the jet boundary is defined as where solids change their upward motion to downward one. The rate of solids entrainment immediately above the orifice is probably enhanced by the low resistance to the radial flow of the dense phase and by the concurrent flow of entrained gas (25).

Hirato et al. (26) measured the particle velocities in a large three-dimensional fluidized bed using a spring plate detector with strain gauge. Their results showed that due to the presence of many small bubbles above the distributor, both upward and downward velocities of particles near the distributor were small enough to assume that particles moved in a radial direction rather than in an axial direction.

Ishida et al. (27) made interesting observations on the behavior of particles in the jet using a linearly-arrayed multi-fiber optical probe. Their detailed analysis of the experimental results showed that the concentration of particles in the jet was not uniform; particles tended to form swarms, and dense and dilute swarms of particles passed alternatively through the jet. This periodic appearance of particle swarms may indicate that the solids entrainment into the jet does not take place uniformly in time and it will be useful to measure the times

between two successive dense swarms to see if they are related to the frequency of bubble formation.

In a bed with auxiliary gas flow, fluidizing gas is also known to be entrained into the jet from the dense phase up to a certain distance from the orifice, jet gas eventually re-entering the dense phase from there on. Depending on particle size and density, the inversion in the direction of gas flow between the jet and the dense phase occurs at difference distances from the orifice (25).

#### 1-2-2. Development of grid region models

As pointed out earlier, many models which have been proposed in the literature for the bubbling region of gas fluidized beds cannot properly describe the high rates of heat and mass transfer and high conversion rates near the distributor, especially for fast reactions. In order to complete the modeling of fluidized bed reactors, it is, therefore, necessary to have a separate description of gas and solids behavior in the grid region which can then be combined with many existing bubbling bed models for better prediction of the overall performance of the bed.

Behie and Kehoe (13) proposed a simple two-phase model by assuming that gas enters the bed as well-mixed grid jets with plug flow in the axial direction and that the jets break up into bubbles and interstitial gas flow at a certain distance  $h$  above the distributor with a dense phase perfectly mixed throughout the bed. The equations describing their model are

jet region ( $0 \leq z \leq h$ ):

$$Q_o \frac{dy_j}{dz} + k_j a_j A (y_j - y_\infty) = 0 \quad (1.6)$$

bubble phase ( $h < z \leq H_B$ ):

$$Q_b \frac{dy_b}{dz} + k_b a_b A (y_b - y_\infty) = 0 \quad (1.7)$$

dense phase ( $0 \leq z \leq H_B$ ):

$$Q_d (y_{d_o} - y_\infty) + k_j a_j A \int_0^h (y_j - y_\infty) dz \\ + k_b a_b A \int_h^{H_B} (y_b - y_\infty) dz = L_d V_d \rho_s R(y_\infty) \quad (1.8)$$

and 
$$Q_o = Q_b + Q_d \quad (1.9)$$

where  $y$ 's and  $Q$ 's are mass fractions and flow rates of reacting gas respectively,  $k_j a_j$  and  $k_b a_b$  are mass transfer coefficients per unit volume of reactor for the jet and bubbling regions, respectively, and  $L_d V_d \rho_s R(y_\infty)$  represents the total reaction rate in the dense phase.

They showed experimentally that  $k_j a_j$  is much greater than  $k_b a_b$  (28),

and they assumed a first-order gas-solids reaction with no diffusional limitations in the dense phase. With a bed 0.6 m deep, their calculations showed that their model predicted a conversion of 84 %, while the bubble model with  $h = 0$  predicted a conversion of only 11 % for fast reactions. For slow reactions, the difference in conversion rate was much less significant since mass transfer resistance did not limit the rate as severely (13). One key assumption made in the Behie and Kehoe model was that there was no entrainment of solid particles into the jet. However, as shown experimentally by others (15,24,26,27), particles are indeed entrained into the voids formed above an orifice, and it is known that even very low concentrations of solids in dilute phase regions of the bed can have a considerable effect on overall conversion for highly exothermic reactions such as fluidized bed coal combustion (29).

Grace and De Lasa (30) set out to test the sensitivity of the jet model by Behie and Kehoe (13) to the mode of gas mixing in the dense phase by considering two extreme cases of gas mixing. In the first case, the entire dense phase was assumed to be a stagnant region with no vertical gas flow within it, while mass transfer of gas between the dense phase and the jet and bubbles was allowed by assuming different interphase mass transfer coefficients. In the other case, they considered the dense phase to consist of two regions, a stagnant region from the distributor to the top of the jet and the remaining dense phase in the bed with perfect mixing. Qualitatively, both cases predicted much higher conversion for a fast reaction as in the jet model by Behie and Kehoe (13) than pure bubble models.

Yates et al. (18) developed a simple model of gas entry into the bed in which a large part of gas that ultimately forms a bubble with restricted mass transfer to the particles first enters the dense phase for a brief period during which appreciable chemical reactions can occur if it is a fast reaction. For a pseudohomogeneous first-order reaction between gas and solids, the fraction of reactant A remaining unconverted in the bubble at the exit of the grid region was given as:

$$\frac{C_{Ab}}{C_{Ao}} = K + (1-K) \exp [-0.5 (1-\epsilon_d) k_s t_e] \quad (1.10)$$

where  $K$  - fraction of gas flow visible as bubbles at the orifice

$\epsilon_d$  - dense phase voidage in the grid region

$k_s$  - first-order rate constant

$t_e$  - time taken for the bubble to form completely

Yang et al. (31) later refined this model by Yates et al. (18) by introducing the residence time distribution function of the gas in the dense phase prior to entering the bubble, instead of just assuming it to be  $0.5 t_e$ . Further tests of the model using the oxidative catalytic dehydrogenation in air of butene-1 to butadiene showed a qualitative correspondence between experimental observations and model predictions in the trend of decreasing conversion with increasing orifice flow rate (31). They seemed to exclude the gas-solids reaction in the bubble wake which was estimated to occupy approximately one-fourth of the

volume of the sphere centered on the bubble, and the parameters used in their model, especially the relationship between the expanded dense phase voidage and orifice flow rate, needed to be estimated accurately from careful experiments in order to improve model predictions.

Patrose and Caram (32) studied two-dimensional modeling of the carbon oxidation reactions in the grid jet in a fluidized bed coal combustor for the purpose of assessing the extent of reactions that can occur due to solids entrainment into the jet. Their overall picture of the grid region was similar to that of Behie and Kehoe (13); the main difference was that the reactions took place only in the jet phase in the former model, while the fluidized dense phase surrounding the jet was the reaction zone in the latter. The effect of the inert bed particles on the diffusion of oxygen to burning particles in the jet was ignored just by using the well-known correlation by Ranz and Marshall (33) for a single sphere in an infinite medium. Although no comparison was made with experimental data, their simulation results showed that the solids entrainment rates were high enough to consume all the oxygen in the entering air and absorb the heat released from the combustion.

Recognition of the importance of the grid region on the overall performance of fluidized bed reactors did not appear in the literature until 70's and only a handful of works on the grid region modeling have been reported since then. As briefly summarized here, the modeling is still at an early stage of development, and more fundamental experimental works on the complicated behavior of gas and solids flows and their effects on the transport properties and the chemical

reactions in the grid region are needed for any further improvement of existing models.

1-3. Objectives of the Research

This study examines combustion and mass transfer characteristics of large carbon particles in the grid region of a fluidized bed combustor. Briefly, the research is directed toward:

- (1) single particle experiments of measuring combustion rates of electrode graphite spheres fixed at various locations in the grid region for each set of operating variables such as inert bed particle size and superficial air velocity.
- (2) estimation of the grid region height, the dead zone height and external mass transfer coefficient local to a carbon particle from the results of single particle experiments.
- (3) development of mass transfer correlations for oxygen transfer to a burning carbon particle in the dilute and dense phases of the grid region.

It is the ultimate aim of this study that results of both experimental and theoretical works described above can contribute significantly to the combustion modeling of the grid region.

**CHAPTER 2**

**SINGLE PARTICLE COMBUSTION OF ELECTRODE GRAPHITE SPHERES**

**IN THE GRID REGION OF A FLUIDIZED BED COMBUSTOR**

## 2-1. Introduction

The rate of combustion of single carbon particles in a fluidized bed of inert particles is an overall result of physical processes such as transport of heat and mass and chemical reactions taking place in and around the carbon particles. Figure 2.1 shows a carbon particle burning in the bubbling region of a fluidized bed. According to the two-phase theory of fluidization (19), there are two sources of oxygen for the combustion of a carbon particle which spends most of its time in the particulate phase; mass transfer of oxygen from gas flowing through the particulate phase at a velocity of  $U_{mf}/\epsilon_{mf}$  and from bubbles rising at a velocity of  $U_b$ . Oxygen flowing with bubbles must diffuse out of the bubble and through the particulate phase to reach the active surface of burning carbon particles. As outlined by La Nauze (34), the advantage of single particle experiments is the elimination of the bubble-particulate phase interchange resistance which allows the oxygen concentration in the particulate phase to be taken as that of the inlet gas. In the grid region, this advantage is equally well preserved, since the resistance to oxygen transfer from the jet forming right above the orifice to the dense phase between two adjacent jets can also be ignored due to low oxygen consumption involved in single particle experiments. If the chemical reactivity of a specific type of carbon is carefully measured or known, the external mass transfer resistance by the inert particles around the burning carbon particle can be estimated once the overall rate of combustion is measured from suitable experiment.

Unlike in the bubbling region, the combustion rates of carbon particles fixed in the grid region are expected to depend strongly upon the particle position due to the presence of gas jets and the dense phase consisting of relatively immobile inert particles. This chapter discusses the single particle experiments of measuring the combustion rates of electrode graphite spheres fixed at various locations within the grid region near the multi-orifice gas distributor. The experimental results will be analyzed in light of the experimental observations of gas and solids flows in the grid region, as discussed in Chapter 1, and the external mass transfer coefficients local to a carbon particle will also be calculated from the combustion data.

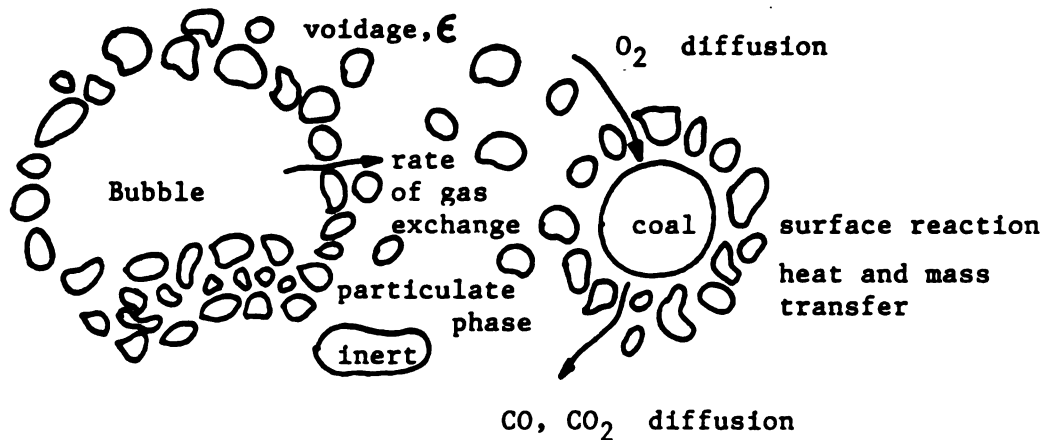
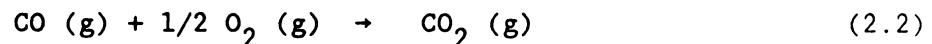
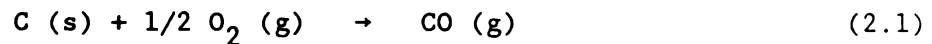


Fig. 2.1 A coal particle burning in the particulate phase of the bubbling region, from La Nauze (34).

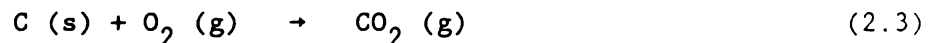
2-2. Combustion Characteristics of Carbon in a Fluidized Bed  
Combustor

Despite many intensive studies, the mechanism of the C-O<sub>2</sub> reaction is probably the least understood among carbon gasification reactions of commercial interest. An excellent review has been given by Laurendeau (35).

As shown in Figure 2.1, oxygen diffuses through the gaseous boundary layer around the burning carbon particle to the active surface where it reacts with carbon to form CO and CO<sub>2</sub>, with the CO/CO<sub>2</sub> ratio increasing substantially at higher temperatures and lower pressures. Under the typical conditions for atmospheric combustion, it appears as a consensus that solid carbon reacts with oxygen to form CO only according to Eq.(2.1), with subsequent CO oxidation taking place in the gaseous boundary layer according to Eq.(2.2):



The homogeneous reaction by Eq.(2.2) contributes approximately two third of the heat produced by the overall heterogeneous reaction:



$$\Delta H_{\text{rxn}, 1163\text{K}} = -33,000 \text{ kJ/kgC}$$

Hence, it is of considerable importance in heat and mass balance of combustion to know just how much of the heat produced by CO oxidation is used to heat the carbon particle. This is still the subject of intense controversy due to the lack of adequate experimental techniques of measuring the precise location of CO oxidation. Using the kinetic expression by Howard et al. (36) for CO oxidation in postflame gases, Ross and Davidson (6) calculated the approximate radius of CO oxidation zone and concluded that CO burns close to the carbon particles with diameters ranging from 0.5 to 2 mm. The theoretical analysis by Caram and Amundson (37) also shows that the escape of CO does not occur until the particle diameter decreases below 0.1 mm. Although some degree of CO escape into the surrounding particulate phase takes place depending on the velocity and temperature of the gas phase (38), it is generally assumed in many studies (7,8,39) that for large carbon particles of diameter greater than 3 mm the conversion of solid carbon to CO<sub>2</sub> occurs essentially at the surface of carbon particles according to Eq.(2.3). Consequently, large carbon particles burn at much higher temperatures than the bed up to 250 K above, and the combustion has been shown to be controlled mainly by diffusion of oxygen through the particulate phase due to high reaction rates (6,7,8,38,39,45).

The combustion rate, expressed as the weight of carbon consumed per unit external surface area of the particle, is given by:

$$R_c = k_c C_s^n = \beta k_m (C_p - C_s), \text{ kgC/m}^2\text{s} \quad (2.4)$$

where  $k_c$  is the apparent chemical rate coefficient including any intraparticle diffusional effects,  $n$  is the apparent reaction order of combustion,  $C_s$  is the oxygen concentration at the surface of the carbon particle,  $k_m$  is the external mass transfer coefficient in the dense or particulate phase including the boundary layer diffusion,  $C_p$  is the oxygen concentration in the dense phase, and  $\beta$  is the stoichiometric coefficient which takes the value of  $3/4$  if the overall reaction is  $C + 1/2 O_2 \rightarrow CO$  and  $3/8$  if the overall reaction is  $C + O_2 \rightarrow CO_2$ .

Eq.(2.4) merely states that during steady-state combustion the amount of carbon consumed at the surface must be balanced by that of oxygen transferred to the surface through the stoichiometric coefficient  $\beta$ .

By eliminating the unknown  $C_s$ , Eq.(2.4) can be written as:

$$R_c = k_c [ (1 - \phi) C_o ]^n \quad (2.5)$$

where  $\phi$  is the degree of mass transfer control, defined as  $R_c / R_{cm}$ ,  $R_{cm}$  is the maximum possible combustion rate when the combustion is controlled only by mass transfer of oxygen local to the carbon, i.e.  $C_s = 0$ , and  $C_p$  has been replaced by  $C_o$ , the oxygen concentration of incoming air for single particle experiments.

The combustion rate,  $R_c$ , is calculated directly from the weight and diameter data during burn-off. For one interval of  $t$  second burning:

$$R_c = \Delta W / t \pi d_p^2 \quad (2.6)$$

where  $\Delta W$  is the weight loss, and  $d_p$  is the average particle diameter during a combustion interval of  $t$  seconds.

The apparent chemical rate coefficient,  $k_c$ , is usually given in Arrhenius form as:

$$k_c = A_o \exp [ -E_a / RT_p ] \quad (2.7)$$

where  $T_p$  is the average particle temperature during burn-off. The preexponential factor,  $A_o$ , the apparent activation energy,  $E_a$ , and the apparent order,  $n$ , are determined from separate kinetic experiments for a specific type of carbon. At the present time, there are numerous kinetic data reported in the literature for various types of coal chars and purified carbons, and excellent reviews have been given by Smith (41,42).

Assuming that the heterogenous reaction in Eq.(2.3) has the apparent order of one, as is done in many studies for temperatures greater than 1,000 K, Eq.(2.5) can be rewritten as:

$$R_c = C_o / (1/k_c + d_p / \beta \text{ Sh } D_g) \quad (2.8)$$

where  $\text{Sh}$  is the Sherwood number, defined as  $k_m d_p / D_g$ , and  $D_g$  is the diffusivity of oxygen in air. The reciprocal of the terms in the

bracket in Eq.(2.8) can be regarded as the overall rate coefficient, which clearly shows the effects of both chemical kinetics and local mass transfer on combustion of carbon particles.

As noted earlier, the degree of mass transfer control,  $\phi$ , is expected to decrease from unity as the particle size decreases during burn-off, and can be calculated from Eq.(2.5) once the combustion rates and the kinetic data are obtained from experiments. The dimensionless mass transfer coefficient,  $Sh$ , is then calculated from:

$$Sh = \frac{k_m d_p}{D_g} = \frac{R_c d_p}{\beta \phi D_g C_o} \quad (2.9)$$

### 2-3. Definition of the Grid Region

As shown in Figure 2.2, the gas flow in the grid region near the multi-orifice gas distributor is mainly in the form of gas jets forming right at the orifice and small bubbles detaching from these jets, and we call this region of relatively low solids concentration the dilute phase. Gas also leaks throughout the jet boundary to fluidize the region between two adjacent vertical jets, and the mobility of bed particles in this dense phase is expected to increase from that in the packed bed at the distributor to that in the bubbling region at some distance above.

Here we define the grid region height,  $H$ , to be the vertical distance from the distributor to a height where bubbles first begin to deviate from their vertical path due to the bed momentum. It is worth

noting that this definition of the grid region height is similar in concept to that of the jet penetration length by Knowlton and Hirsan (43). Hence, above H, the time averaged bed voidage is uniform everywhere at  $\epsilon_b$ , the mean bed voidage including bubbles. Furthermore, combustion and mass transfer characteristics should be the same regardless of particle position above the grid region height due to the overall uniformity of the bubbling region.

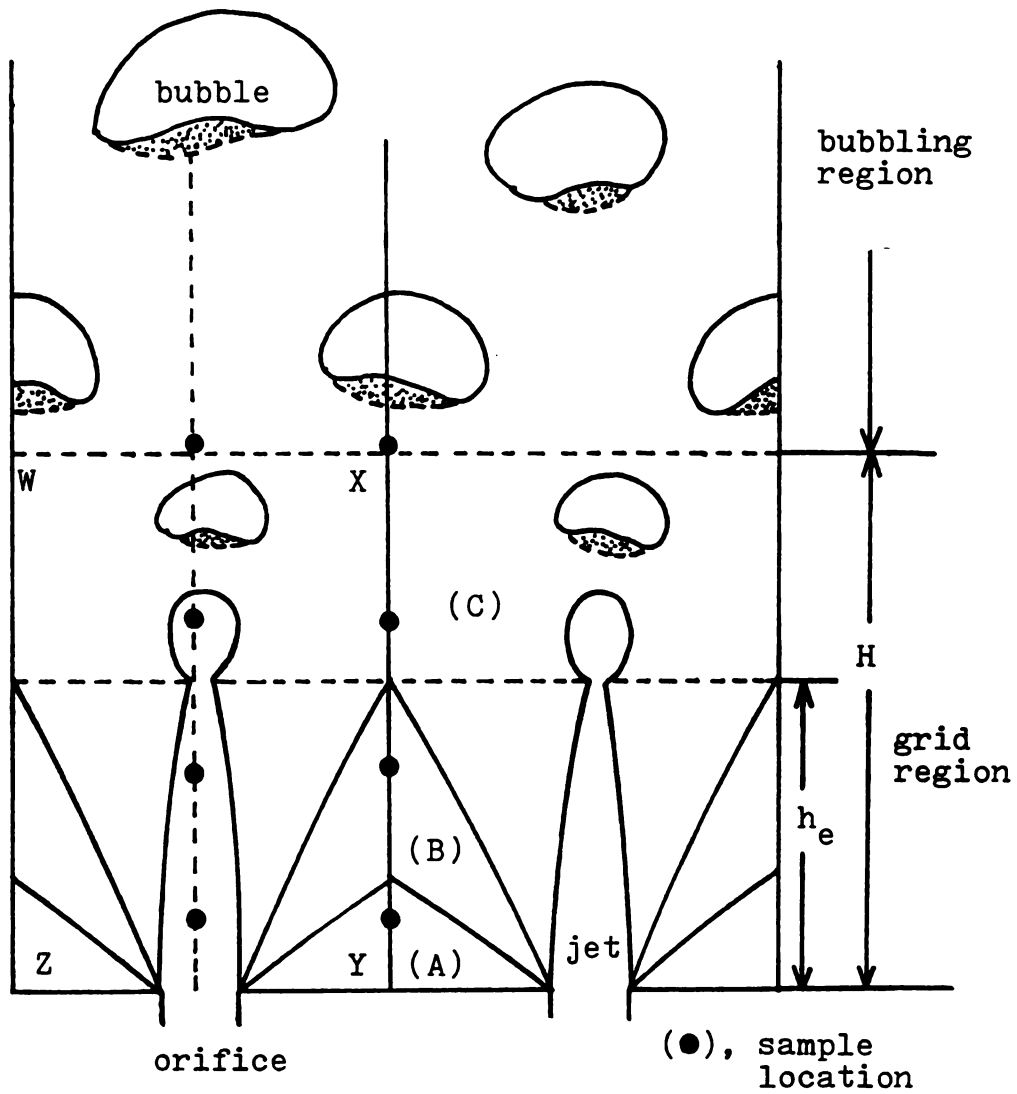


Figure 2.2 A schematic sketch of the grid region ( (A), dead zone; (B), quasi-dead zone; (C), zone of sluggish particle motion ).

## 2-4. Single Particle Experiments

This section discusses the experimental equipment and procedures of measuring combustion rates of single electrode graphite spheres fixed at various locations within the grid region.

### 2-4-1. Experimental equipment

A schematic sketch of the experimental fluidized bed unit is shown in Figure 2.3. The bed is 15.5 cm I.D. and 43.5 cm high, and is made of 6.4 mm thick stainless steel. The gas distributor consists of two identical plates, each having seven 6.4 mm diameter holes in a triangular pitch with pitch size 5.56 cm, as shown in Figure 2.4. In order to ensure a uniform gas distribution, the thickness of each distributor plate was estimated to be about 4.5 mm for a bed of silica sand, 20 cm high at minimum fluidization and mean particle diameter of 0.2 mm or greater. See Appendix A.1 for the calculational method of determining the thickness. A layer of stainless steel mesh wire of 0.15 mm aperture is inserted between the two distributor plates to retain the sand during shut-downs.

The bed is heated externally by four quarter-circular 40.64 cm high nickel-chrome heating units of 1625 W each at 230 V with Lindberg control console of the proportional-integral type. The spacing between the bed and the cylindrical heating unit is kept at 2.5 cm, and the whole bed assembly is insulated by a one-inch thick blanket of High Alumina Ceramic Fiber. In order to prevent any significant heat loss through the gas distributor, the inlet gas stream is first heated by

the heating tape and then by the main heating unit in the plenum chamber, before it enters the bed.

Laboratory air saturated at 90 psig and ultra pure nitrogen are used as fluidizing gases. The flow rate of each gas is monitored by a high resolution variable area flowmeter for low flow rates and by a variable area bypass flowmeter for high flow rates, each with a needle valve. The instantaneous switch from one gas to the other is made by a highly sensitive three-way valve, and the dynamic pressure of each gas stream is measured by a pressure gauge.

Silica sand of three different mean particle sizes is used as inert bed particles, and electrode graphite spheres of 1 cm initial diameter are used as carbon samples. Table 2.1 summarizes the physical properties of silica sand and electrode graphite spheres used in this study. A thin chromel-alumel thermocouple of 63.5 cm long and Inconel 600 sheath of 1.02 mm O.D. is dipped into an alumina base adhesive and inserted into a 1.07 mm hole drilled straight halfway to the center of each graphite sphere for the measurement of particle temperatures. The long thermocouple-carbon sphere assembly is then supported rigidly by passing it through a stainless steel tube of 1.27 mm I.D. which is in turn held tightly by a precision clamp for an exact positioning of the graphite spheres within the grid region. A separate chromel-alumel thermocouple monitors the bed temperature continuously, and all temperatures are recorded by highly sensitive digital readout meters. The weight and particle diameter of each graphite sphere are measured with the use of an analytical balance and a micrometer, respectively.

Table 2.1 Physical properties of bed materials

---

Silica sand :  $\rho_s = 2700 \text{ Kg/m}^3$

---

$d_s$ ( $\mu\text{m}$ )	$U_{mf}^*$ (cm/s) at 1163 K	$\epsilon_{mf}^*$ at 1163K
230	1.85	0.4
460	7.35	0.4
620	13.25	0.4

---

Electrode graphite spheres<sup>\*\*</sup>: Initial diameter  $\approx 1 \text{ cm}$   
 $\rho_p = 1600 \text{ Kg / m}^3$   
porosity = 20 % by volume  
Impurity level  $\approx 1,000 \text{ ppm}$

---

\* See Section 2-5 for the calculations.

\*\* Manufactured by Bay Carbon, Bay City, Michigan.

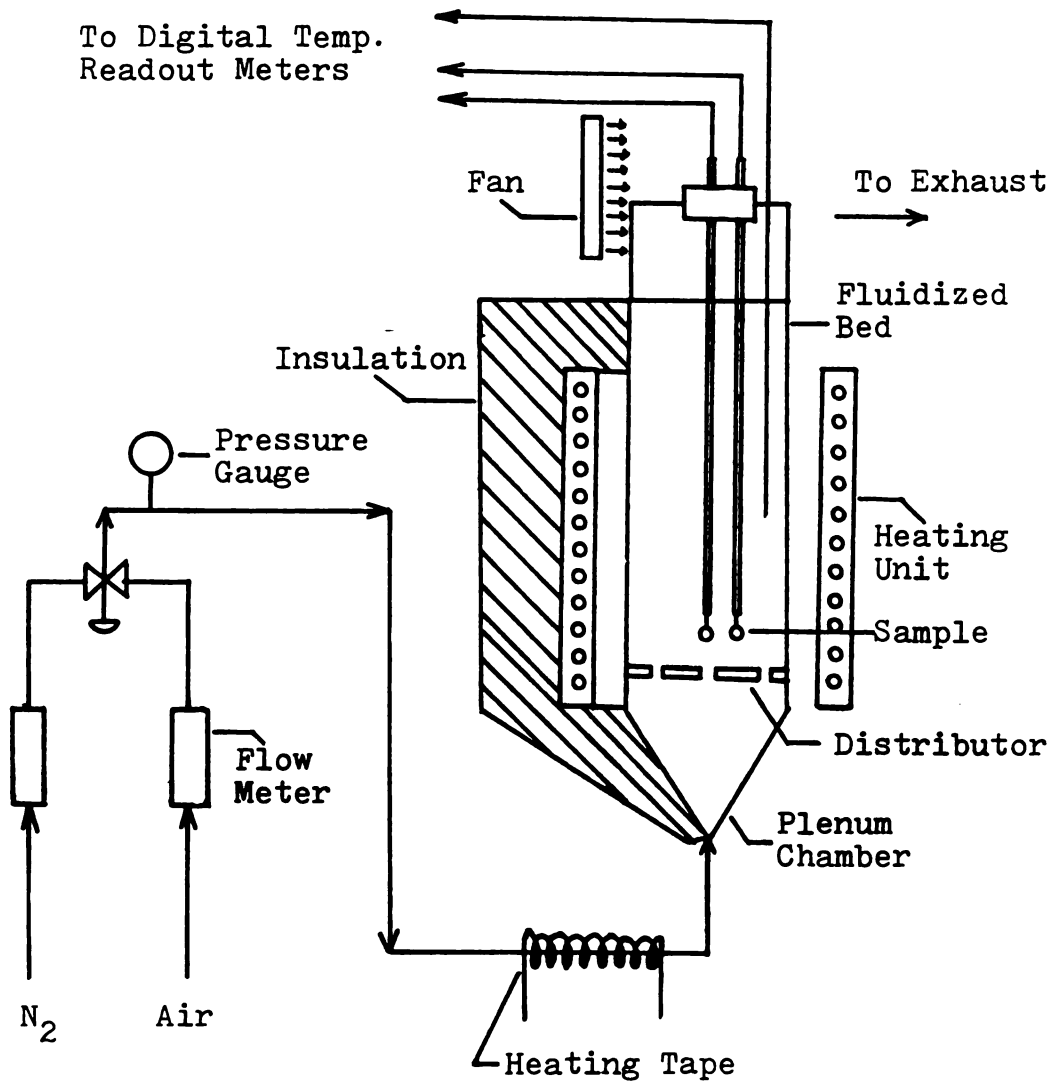


Figure 2.3 Experimental fluidized bed unit.

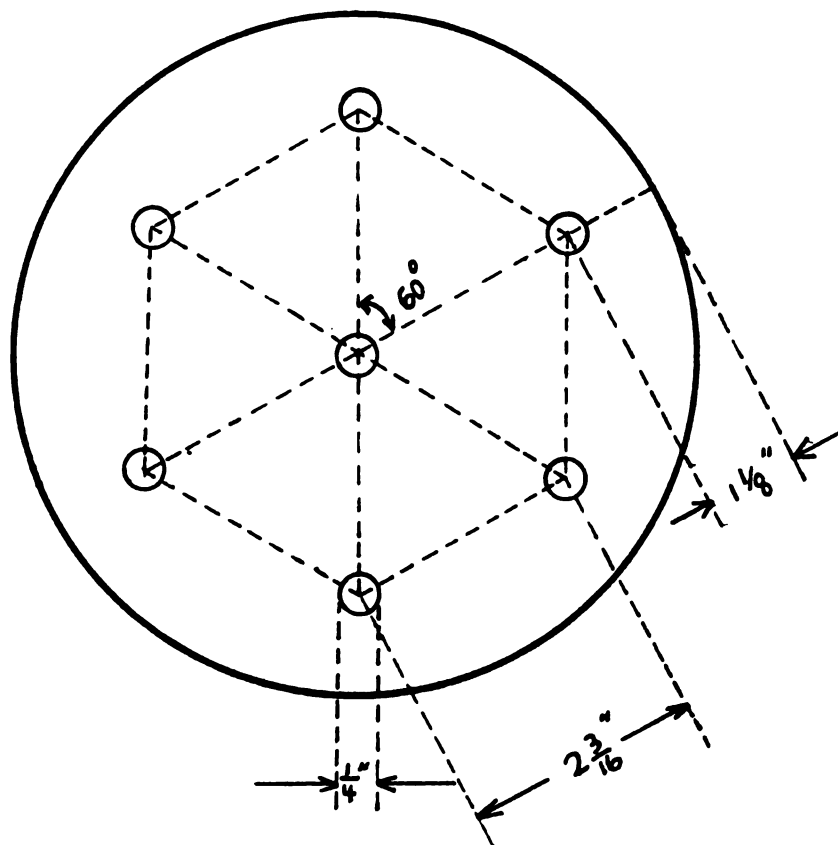


Figure 2.4 Multiorifice gas distributor.

#### 2-4-2. Experimental procedures

The mode of combustion of electrode graphite spheres has to be determined first. An electrode graphite sphere attached to a thin, flexible nichrome wire is dropped into a hot bed of sand fluidized by  $N_2$  at 1163 K. The wire is long enough to ensure the freedom of particle movement in all directions, including the grid region. After the carbon particle reaches the bed temperature, usually within one minute, the fluidizing gas is quickly switched to air using a three-way valve. After a predetermined time, depending on the particle reactivity, the gas is switched back to  $N_2$  to stop further combustion. The carbon sample is then quickly removed from the bed and transferred into a liquid nitrogen container for cooling. After the weight and diameter of the graphite sphere are measured, the carbon sample is put back into the hot bed and heated in  $N_2$  up to the bed temperature, after which the gas is switched again to air to continue the combustion. The same sequence of procedures is repeated, until the carbon sample burns down to a size too small to be held by the wire.

The ratio of the particle diameter to its initial value,  $d/d_0$ , is plotted against the fractional burn-off,  $f$ , to see if the combustion follows the shrinking sphere mode. The apparent density of the carbon sample during each interval of combustion is also calculated from the weight and diameter data. The relationship between apparent density and particle diameter is used later in the analysis of the experimental results involving fixed carbon samples. Since the particle moves

freely within the entire bed, the combustion rates measured are the overall ones which reflect the combustion characteristics both in the bubbling and in the grid region. It should be noted here that many studies (7,8,44,45) imposed some restrictions on the particle movement so that the combustion rates were measured exclusively in the bubbling region.

After the combustion mode of electrode graphite spheres has been examined, the next step is to measure the burning rates at various locations in the grid region. As shown in Figure 2.2, a graphite sphere is fixed at a location along the axis of the jet, while another graphite sphere is fixed at the same vertical distance from the distributor along the axis of the dense phase. The method of holding each carbon sample rigidly at its position has been described in the previous section. While the bed is fluidized with  $N_2$ , both carbon samples are heated until the temperature of each carbon measured with a thermocouple cease to change. Unlike in the bubbling region, the bed temperature may not be uniform in the grid region due to entrance effects, especially very near the distributor. The fluidizing gas is then quickly switched to air, and the particle temperatures are continuously recorded on a digital readout meter during combustion. After a predetermined time, again depending on the particle reactivity, the gas is switched back to  $N_2$  to stop further combustion, and the carbon samples are quickly removed from the bed simply by lifting the clamp. After cooling in the liquid nitrogen container, three perpendicular dimensions of each of the carbon samples are carefully measured, after which they are returned to their specified positions in

the bed fluidized with  $N_2$ . The same sequence of procedures is repeated until both carbon samples burn down to a size too small to be held by thermocouples.

Due to a slight distortion in the spherical shape during combustion, the diameter of each carbon sphere is calculated as the average of three perpendicular dimensions, and the weight loss due to combustion is estimated from the apparent density-particle diameter relationship obtained earlier. The bed temperature in the bubbling region is also monitored with the use of a separate thermocouple so that the temperature differences between each of the carbon samples and the bed as well as the temperature gradient within the entire bed can be obtained experimentally. As shown in Figure 2.2, the vertical distance of fixed carbon samples can be varied from very near the distributor to the grid region height,  $H$ , where the two burning rates are expected to become approximately equal. The effects of superficial air velocity and inert particle size on the combustion rates are also to be examined, and Table 2.2 summarizes the experimental conditions considered in this study.

Table 2.2 Experimental conditions for single particle combustion  
of electrode graphite spheres in air at 1163 K and 1 atm\*

Run number	$d_p$ ( $\mu\text{m}$ )	U (cm/s)	$U/U_{mf}$	$U_o$ (m/s)	fixed sample position (cm)**
1	460	11.0	1.5	9.4	2.54
2	460	11.0	1.5	9.4	6.35
3	460	11.0	1.5	9.4	7.62
4	460	11.0	1.5	9.4	8.26
5	460	14.7	2.0	12.5	2.54
6	460	14.7	2.0	12.5	7.62
7	460	29.4	4.0	25.0	2.54
8	460	29.4	4.0	25.0	5.72
9	460	29.4	4.0	25.0	7.62
10	460	29.4	4.0	25.0	10.16
11	230	5.5	3.0	4.7	2.54
12	230	5.5	3.0	4.7	5.08
13	230	5.5	3.0	4.7	7.62
14	230	7.3	4.0	6.2	2.54
15	230	7.3	4.0	6.2	5.08
16	230	7.3	4.0	6.2	7.00
17	230	11.0	6.0	9.4	2.54
18	230	11.0	6.0	9.4	5.08
19	230	11.0	6.0	9.4	5.72
20	620	26.5	2.0	22.6	2.54
21	620	26.5	2.0	22.6	5.08
22	620	26.5	2.0	22.6	8.90
23	620	39.7	3.0	33.8	2.54
24	620	39.7	3.0	33.8	5.08
25	620	39.7	3.0	33.8	7.62
26	620	53.0	4.0	45.1	2.54
27	620	53.0	4.0	45.1	5.08
28	620	29.0	2.2	25.0	2.54
29	620	29.0	2.2	25.0	5.08

- \* Static bed height = 20 cm.
- \*\* Denotes the vertical distance of two carbon samples from the distributor, one fixed in the dilute phase and the other fixed in the dense phase.

## 2-5. Estimation of the Minimum Fluidization Velocity, $U_{mf}$

The experimental fluidized bed unit described in the previous section is not equipped with a pressure-measuring device for the estimation of  $U_{mf}$  at high temperatures. Unlike in the bubbling region where a burning particle spend most of its time in the particulate phase, the minimum fluidization velocity is not expected to play an important role in the grid region, since there is no significant quantity of bubbles present to affect the bed hydrodynamics as severely as in the bubbling region. However, reasonable values of  $U_{mf}$  for silica sand are needed in the theoretical analyses given in Chapter 3, and we resort to use the available correlations for its estimation.

At the moment, there are numerous empirical correlations available in the literature for an order-of-magnitude estimation of  $U_{mf}$  for various bed materials at ambient conditions. For example, Wen and Yu (46) suggested the following formula:

$$\frac{d_s U_{mf} \rho_f}{\mu_f} = \left[ 33.7^2 + 0.0408 \frac{d_s^3 \rho_f (\rho_s - \rho_f) g}{\mu_f^2} \right]^{1/2} - 33.7 \quad (2.10)$$

Eq. (2.10) can be used as a first approximation if the particulate phase voidage,  $\epsilon_{mf}$ , and the particle sphericity,  $\phi_s$ , are unknown, and similar correlations have been suggested by many investigators (47,48,49).

As for the prediction of the minimum fluidization velocity at the conditions of practical importance such as high temperatures and pressures, Bin (50) concluded recently that the Ergun (51) equation can be applied successfully to predict the values of  $U_{mf}$  at different conditions provided that experimentally determined values of  $U_{mf}$  and  $\epsilon_{mf}$  at ambient conditions from experiments with air or nitrogen are used. Note here that Bin (50) assumed that  $\epsilon_{mf}$  and  $\phi_s$  calculated as fitting parameters remain essentially constant over the entire range of operating variables. On the other hand, Stubington et al. (52) suggested measuring  $U_{mf}$  directly at different conditions, since  $\phi_s$ 's are difficult to determine for a coal-derived char and  $\epsilon_{mf}$  may vary with temperature. The variation of  $\epsilon_{mf}$  with temperature and pressure was verified experimentally and explained in terms of variation in the interparticle forces due to changing fluid-flow conditions around the particle by Mathur et al. (53).

Due to the difficulties associated with accurately measuring  $\epsilon_{mf}$  and  $\phi_s$  at high temperatures, the values for  $U_{mf}$  in Table 2.1 have been calculated using Eq. (2.10) with its parameters evaluated at 1163 K and 1 atm. Noting the fact that free bubbling occurs at or a little above

$U_{mf}$  for Geldart Group B particles such as silica sands used in this study, the accuracy of  $U_{mf}$ 's in Table 2.1 has been checked by visual observations, and the discrepancy between the calculated  $U_{mf}$ 's and the observed ones is within 10 %. The particulate phase voidages at minimum fluidization in Table 2.1 have been assumed to be constant at 0.4 for sand as in the study by La Nauze et al. (8).

## 2-6. Results of Single Particle Experiments and Discussions

The experimental results of single particle combustion described in Section 2-4 are presented and discussed in this section.

### 2-6-1. Mode of combustion

Many combustion studies (7,40) have concluded that carbon particles burn primarily in a shrinking sphere mode. It can be seen in Figure 2.5 that the data of fractional diameter,  $d/d_0$ , lie considerably above the curve for the shrinking sphere combustion at high fractional burn-off, which indicates a significant internal burning as evidenced by large reduction in the apparent density. Due to its less reactive nature than coal chars and petroleum cokes, the reaction rate of electrode graphite spheres appears to be low enough for oxygen to penetrate a little farther into the inner pore surfaces before it reacts with carbon. The apparent densities are plotted against the particle diameter in Figure 2.6, and Eq. (2.11) is shown to predict the

apparent density within  $\pm 5\%$  accuracy for the range of particle sizes considered:

$$\rho_p = 600 d_p^{0.4}, \text{ kg/m}^3 \quad (2.11)$$

where  $d_p$  is in mm. It should be noted here that Eq. (2.11) is used to calculate the overall combustion rates of fixed carbon samples from the diameter data obtained during burn-off.

The calculation of Sherwood number in Eq. (2.9) requires the overall kinetic data of graphite combustion along with the values of  $D_g$  and  $C_o$ . Field et al. (54) re-examined the previous data using large carbons such as electrode carbon samples of 10 - 15 mm diameter, and suggested the apparent kinetic parameters tabulated in Table 2.3. Due to the similarities in the size, porosity and type of carbon, we have assumed that the combustion kinetics of electrode graphite spheres used in this study is well represented by those in Table 2.3.

Table 2.3 Kinetic and physical data for mass transfer calculations

---

Overall reaction :	$C + O_2 \rightarrow CO_2$	(2.3)
Kinetic data :	$n = 1$	
	$A_o = 87,000 \text{ kg/m}^2 \text{ s atm}^n$	
	$E_a = 36 \text{ kcal/mole}$	
	$950 \leq T_p \leq 1,600 \text{ K}, \quad 0.01 \leq P_{O_2} \leq 0.21 \text{ atm}$	

---

Physical data :

$$D_g = 0.0002542 \text{ m}^2/\text{s}$$

$$C_o = 0.0707 \text{ kg/m}^3$$

at 1163 K and 1 atm

---

The Sherwood numbers thus calculated for a freely moving graphite sphere are shown in Figure 2.7 to be fitted quite well by Eq. (2.12):

$$\epsilon_{mf} (j_D)_{mf} \text{Re}_{mf}^m = 0.105 + 1.505 \left[ \frac{d_p}{d_s} \right]^{-1.05}, \quad (2.12)$$

$$\text{for } 0.1 < \text{Re}_{mf} < 20 \text{ and } 1 \leq d_p/d_s < 200,$$

$$\text{where } m = 0.35 + 0.29 (d_p/d_s)^{-0.50},$$

$$\text{mass transfer factor } (j_D)_{mf} = k_m \text{Sc}^{2/3} / U_{mf},$$

$\text{Re}_{mf} = U_{mf} d_p \rho_f / \mu_f (1 - \epsilon_{mf})$ , and  $d_p$  and  $d_s$  are the carbon and bed inert particle size, respectively. Eq. (2.12) is an empirical

correlation derived by Prins et al. (9) near ambient conditions, and has been shown to correlate well other combustion data at extreme conditions (9). The good agreement between Eq (2.12) and our data in Figure 2.7 thus seems to validate the assumption of using the kinetic data by Field et al. (54) for our electrode graphite samples.

As expected, the degree of mass transfer control for a freely moving graphite sphere is shown in Figure 2.7 to decrease with

decreasing particle size with their values being substantially less than unity. This is another indication of the chemical kinetics having a more pronounced effect on the combustion of electrode graphite samples than more reactive petroleum cokes (7). Throughout the calculations of  $Sh$  and  $\phi$ , the particle temperature was assumed to be constant at 1233 K during burn-off, i.e. 70 K above the bed temperature, which was verified to be reasonably valid in a separate experiment using a flexible thermocouple.

The overall combustion rate in Eq. (2.8) can be rewritten as:

$$R_c A = \frac{d_p^2}{c_1 d_p / Sh + c_2} = c_3 d_p^N, \quad (2.13)$$

where  $c$ 's are constants. If the Sherwood number is large, i.e. the combustion rate is controlled purely by the chemical kinetics,  $N$  takes the values of 2. On the other hand, if the Sherwood number is small or the rate is controlled by mass transfer,  $N$  becomes unity. As shown in Figure 2.8, the combustion of electrode graphite samples is controlled solely by the chemical kinetics at 1073 K due to its low reactivity, and the influence of mass transfer becomes significant at 1163 K. The analysis given above is based on the assumption of the Sherwood number remaining constant during burn-off. As will be shown later in Section 2-6, the Sherwood number indeed decreases with increasing burn-off %, and the accuracy of Eq. (2.13) is, therefore, questionable in determining the relative influence of the chemical kinetics and mass transfer in the combustion of carbons.

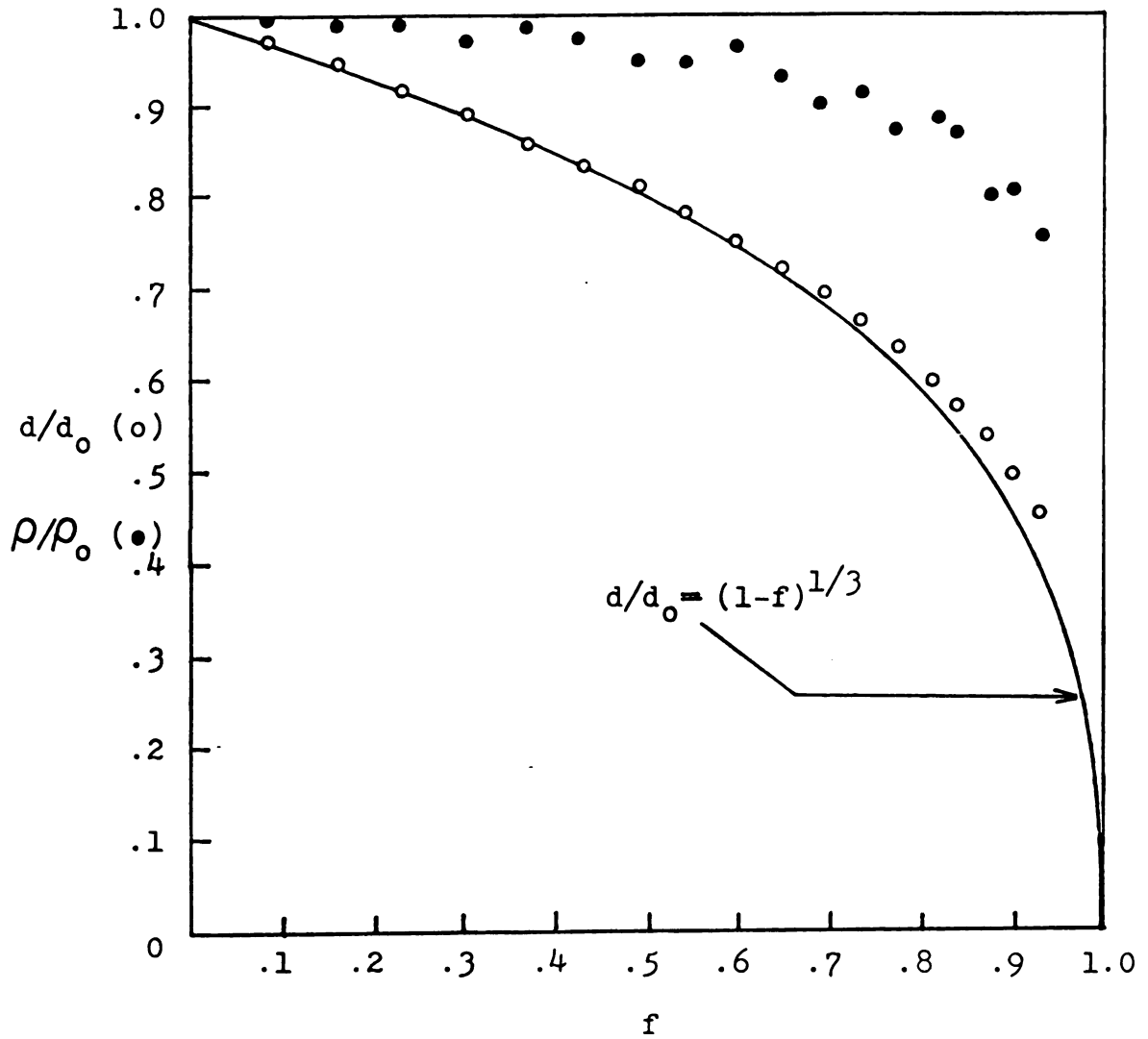


Figure 2.5 Fraction of initial diameter and the ratio of densities versus fractional burn-off,  $f$  ( $T_B = 1163$  K,  $U_0 = 16.6$  m/s,  $d_s = 460$   $\mu\text{m}$ ).

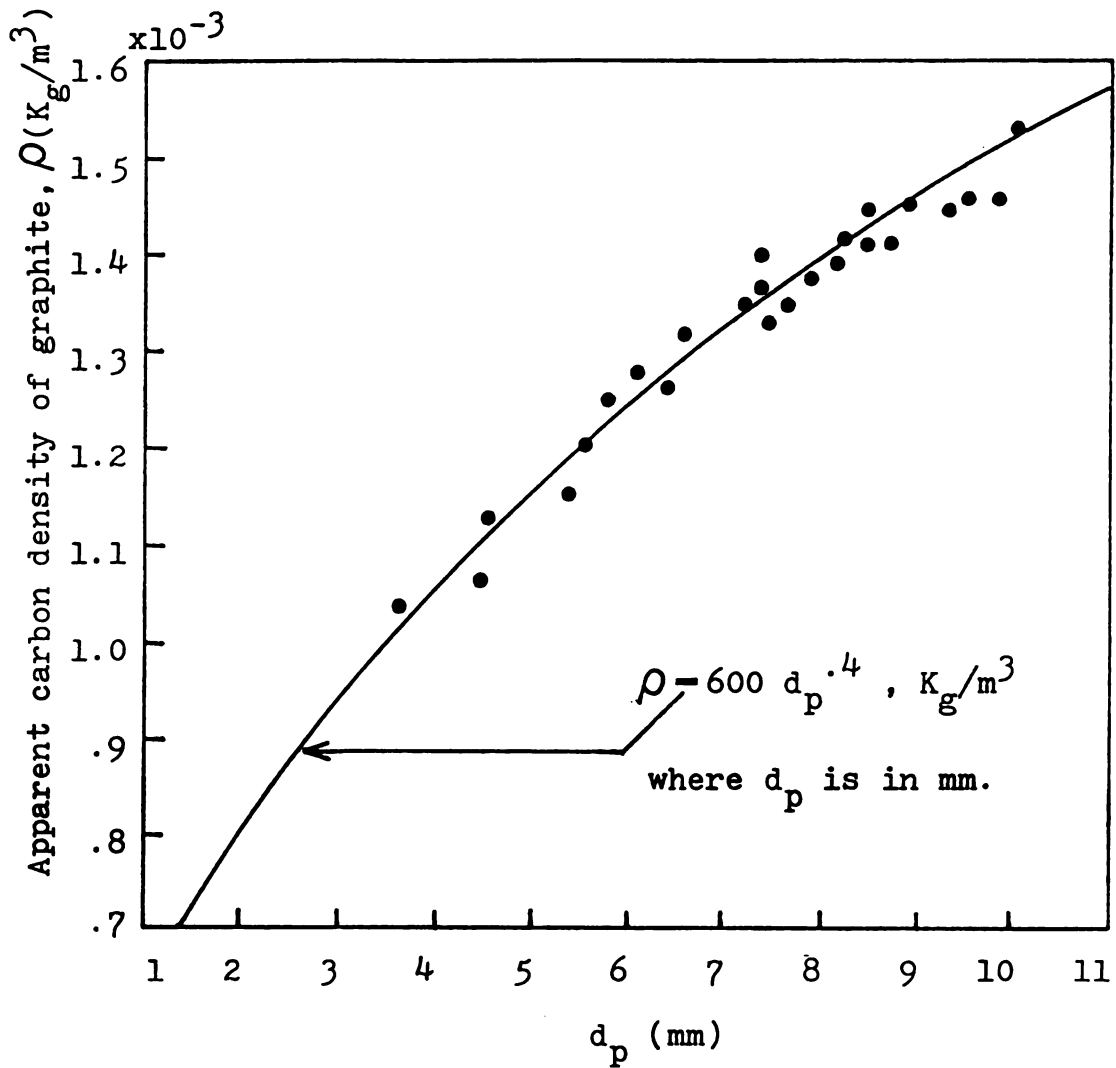


Figure 2.6 Apparent carbon density versus carbon diameter during burn-off ( $T_B = 1163$  K,  $U_0 = 16.6$  m/s,  $d_s = 460$   $\mu\text{m}$  ).

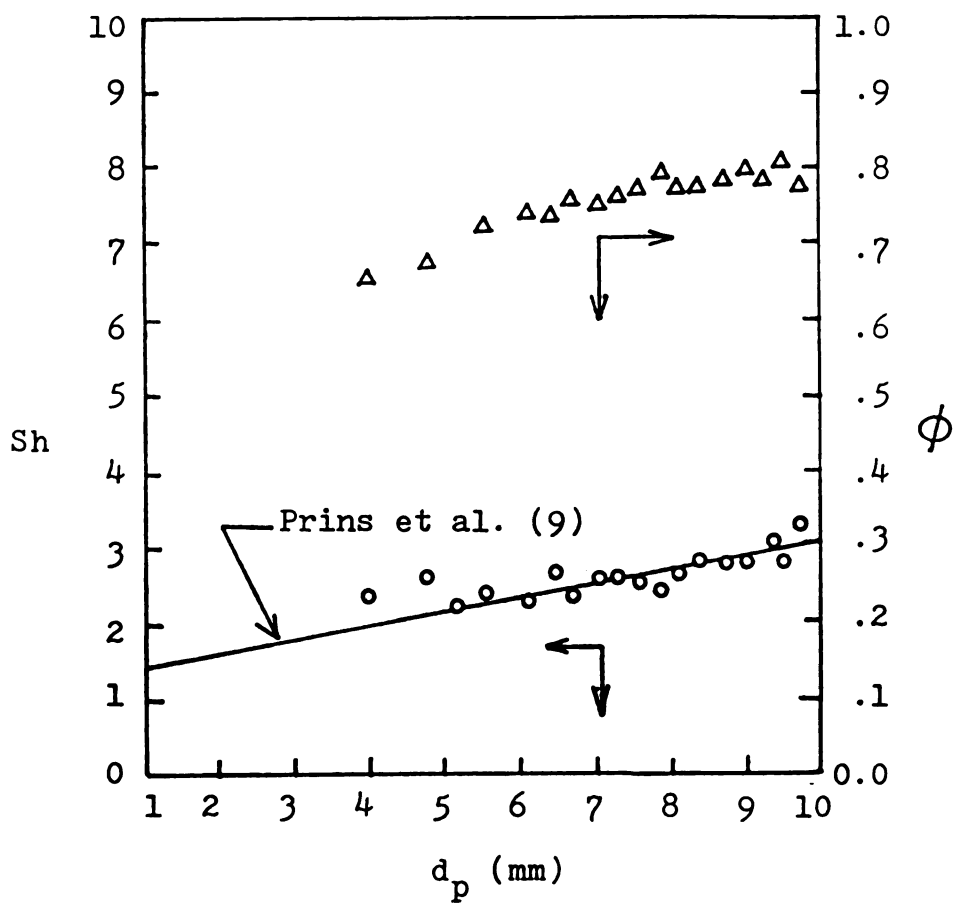


Figure 2.7 Variations in Sherwood number and degree of mass transfer control,  $\phi$ , with particle diameter during burn-off ( $T_B = 1163$  K,  $U_o = 16.6$  m/s,  $d_s = 460$   $\mu\text{m}$  ).

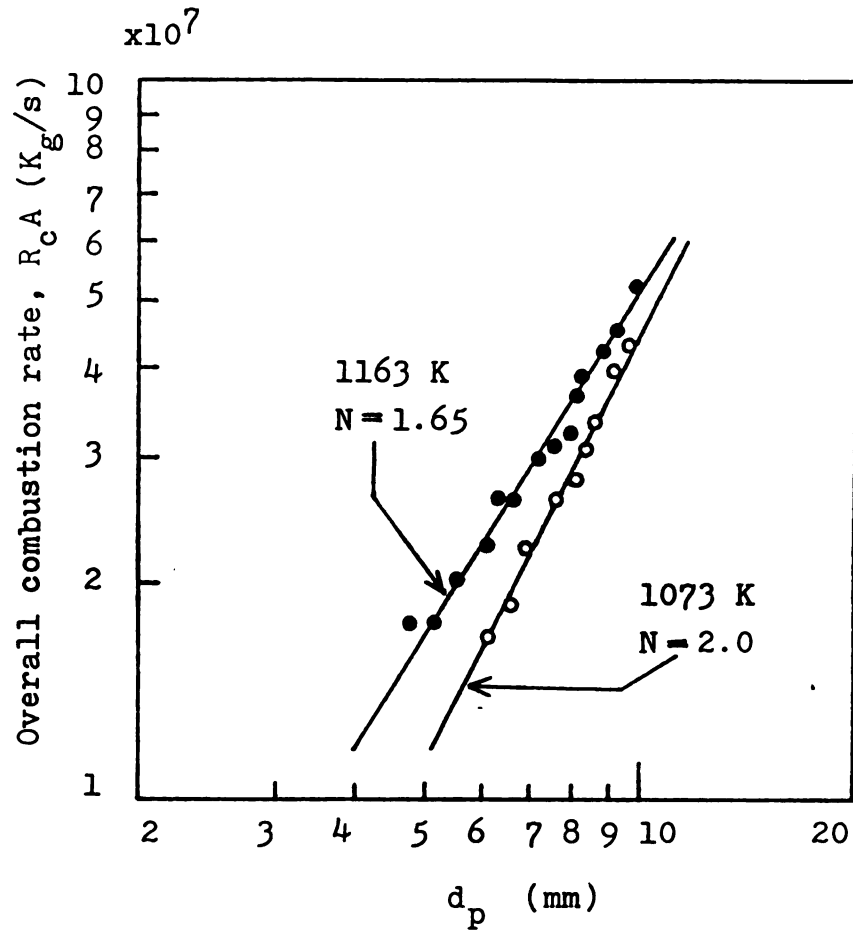


Figure 2.8 Overall combustion rate versus particle diameter for a freely moving graphite sphere ( $U_o = 16.6$  m/s,  $d_s = 460$   $\mu m$  ).

## 2-6-2. Estimation of the grid region height

Figures 2.9 - 2.11 are log-log plots of overall combustion rate versus carbon particle diameter in a bed of silica sand of mean diameter  $620 \mu\text{m}$  with superficial air velocity being twice that at minimum fluidization. At 1 inch above the distributor (Figure 2.9), the combustion rates of a graphite sphere fixed in the dilute phase are shown to be at least twice as high as those in the dense phase. While the difference between the two combustion rates is still significantly large at 2 inches above (Figure 2.10), they become approximately equal at 3.5 inches above the distributor (Figure 2.11).

As the vertical distance from the distributor or the axial distance increases, the cumulative amount of solids entrained into the jet increases, while the amount of gas remaining in the jet decreases due to the gas leakage into the dense phase throughout the jet height. Hence, the overall effect is to increase the mass transfer resistance local to a burning carbon particle and to decrease the convective transport of oxygen by the bulk gas, which results in lowering the overall combustion rates in the dilute phase, as shown in Figure 2.12.

Particles between two adjacent vertical jets near the distributor are relatively immobile, and the combustion in this dead zone is expected to closely resemble that in a packed bed. Above the dead zone, there is a region of sluggish particle motion, called the quasi-dead zone above which the so-called intermittenly mixed region exists (23). It is, therefore, expected that the combustion rate of a carbon particle fixed in the dense phase increases with increasing vertical

distance, until it eventually becomes equal to the combustion rate of a carbon particle fixed in the dilute phase at the same vertical distance, as shown in Figure 2.12. This vertical distance of two equal combustion rates can be regarded as the grid region height measured from the reaction point of view. The accurate measurement of the grid region height is of great practical importance in the modeling study of the entire bed.

As the superficial air velocity increases, the grid region height is shown in Figures 2.13 and 2.14 to decrease from 3.5 inches at  $U = 2 U_{mf}$  to 3 inches at  $U = 3 U_{mf}$  and 2 inches at  $U = 4 U_{mf}$ . The same trend is also observed in beds of sand of mean diameters  $460 \mu\text{m}$  (Figures 2.15 - 2.17) and  $230 \mu\text{m}$  (Figures 2.18 and 2.19). The experimental grid region heights are further tabulated in Table 2.5, and compared in Table 2.4 with the jet penetration length calculated from Eqs. (1.2)-(1.5). As shown in Table 2.4, all correlations predict the trend opposite to our results, since they do not take into account the fact that the dense phase becomes completely fluidized at lower heights with increasing gas flow rate.

Based on the theory of spouted beds by Lefroy and Davidson (56), Fakhimi et al (57) derived the following expression for the height of entrance effect,  $h_e$ :

$$h_e = 0.51 S (S/d_s)^{0.33} \sin^{-1} (U_{mf}/U), \quad (2.14)$$

where  $S$  is the orifice spacing or the pitch size. It should be noted here that  $h_e$  was defined as the vertical distance from the distributor at which the dense phase becomes fluidized (57). Hence, according to Wen et al. (16), bubbles should form at  $z = h_e$ , as shown in Figure 2.2. Furthermore, the values of  $h_e$  should always be smaller than those of the grid region height, except at minimum fluidization, as shown in Figures 2.20 - 2.22 for  $U$  somewhat greater than  $2 U_{mf}$ . For  $U$  less than  $2 U_{mf}$ , Eq. (2.14) significantly overpredicted the experimental results of Fakhimi et al. (57) in a three dimensional bed of sand of  $350 \mu\text{m}$  mean diameter, and its limited application near minimum fluidization is indicated by the dashed portion of the curve in each of Figures 2.20 - 2.22. This is unfortunate because  $H$  and  $h_e$  should become equal at minimum fluidization due to the absence of bubbles in the bed and Eq. (2.14) could otherwise be used to determine the grid region height at minimum fluidization,  $H_{mf}$ . As will be shown in Chapter 3,  $H_{mf}$  is an important parameter in the grid region study and is difficult to measure due to factors explained in Section 2-5. As shown in Figures 2.20 - 2.22,  $H_{mf}$ 's have been estimated by extrapolating the data to  $U = U_{mf}$ , and tabulated in Table 2.5. However, Eq. (2.14) still seems to be the only one of its kind which correctly predicts the trend of decreasing grid region height with increasing gas flow rate. Eq. (2.14) may also be used to estimate the portion of the grid region occupied by the bubbles or the distance travelled by bubbles prior to coalescence.

This is denoted by  $z_b$  in Figures 2.20 - 2.22, and is shown to increase with increasing  $U$  except for  $d_s = 620 \mu\text{m}$ .

The grid region height for  $460 \mu\text{m}$  sand is given in Table 2.5 as 5.7 cm or 2.25 inch at  $U = 4 U_{mf}$ . As shown in Figure 2.23, the overall combustion rates are the same, regardless of fixed particle position above the grid region height, which indeed verifies the uniformity of the bubbling region. Figure 2.23 further indicates that the grid region height, as defined in Section 2-3, is the correct measure of dividing the bed for the modeling purpose. The values of  $H$  in Table 2.5 also show that the grid region occupies up to 40 % of the entire volume of the bed, which suggests that the grid region cannot be ignored in the overall modeling study.

Table 2.4 Comparison of grid region height with jet penetration length ( $d_s = 460 \mu\text{m}$ ,  $T_B = 1163 \text{ K}$ )

correlations	$U/U_{mf} = 2.0$	$U/U_{mf} = 4.0$
Merry (14)	2.7 cm	3.7 cm
Yang and Keairns (21)	7.9 cm	10.2 cm
Wen et al. (22)	7.5 cm	9.3 cm
Zenz (55)	7.6 cm	17.3 cm
Fakhimi (57)	7.3 cm	3.5 cm
Present work	7.6 cm	5.7 cm

Table 2.5 Experimental grid region heights at 1163 K

Inert particle size	$U/U_{mf}$	H(cm)	$h_e^{**}$ (cm)
230	1.0	8.8*	27.2
	3.0	7.6	5.9
	4.0	7.0	4.4
	6.0	5.7	2.9
460	1.0	9.0*	21.7
	1.5	8.3	10.1
	2.0	7.6	7.3
	4.0	5.7	3.5
620	1.0	11.2*	19.6
	2.0	8.9	6.5
	3.0	7.6	4.3
	4.0	5.1	3.2

\* Extrapolated values.

\*\* Calculated from Eq. (2.14).

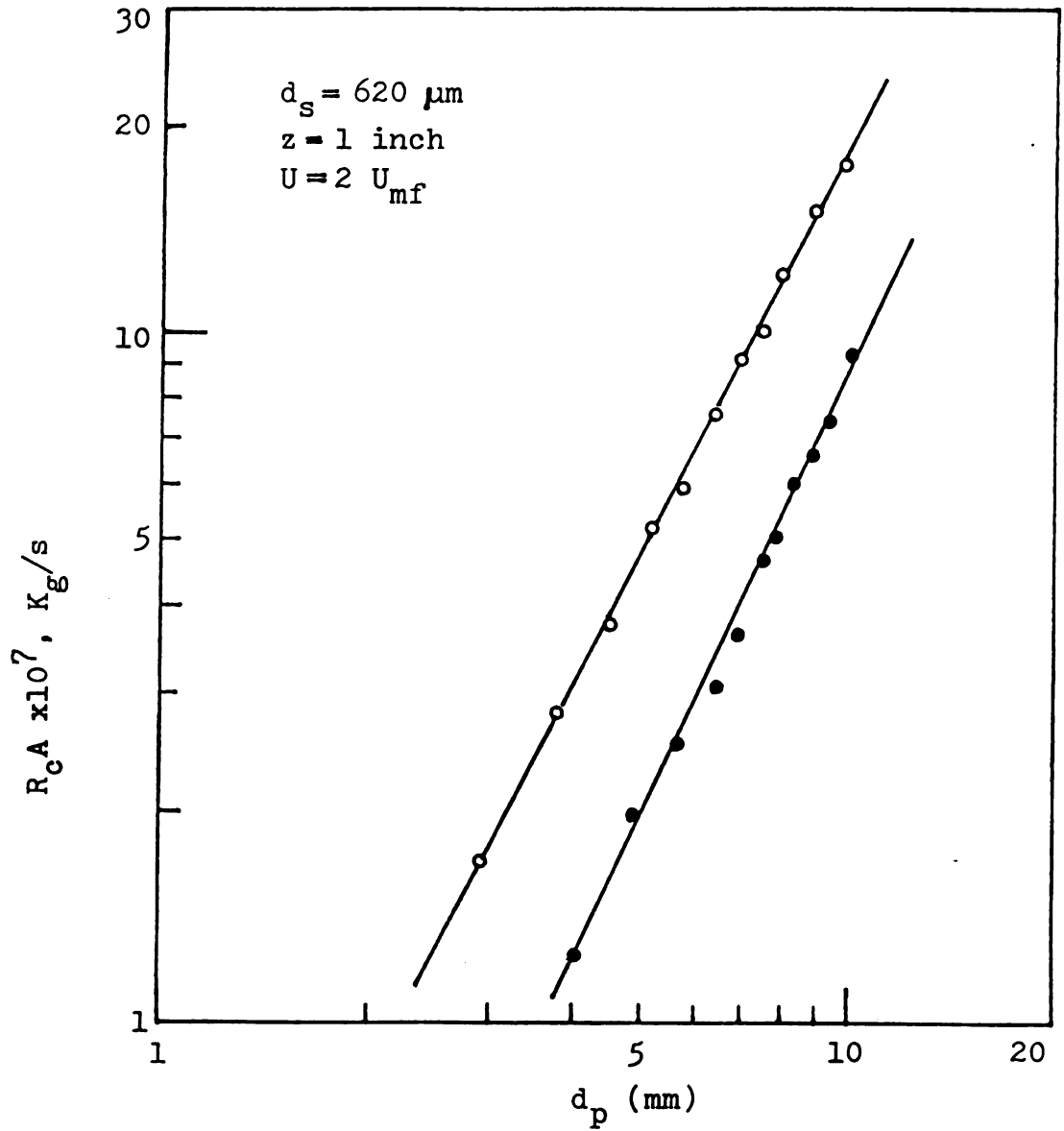


Figure 2.9 Overall combustion rate versus particle diameter ( $T_B = 1163 \text{ K}$ ,  $U_o = 22.6 \text{ m/s}$ ; dilute phase (o), dense phase (●)).

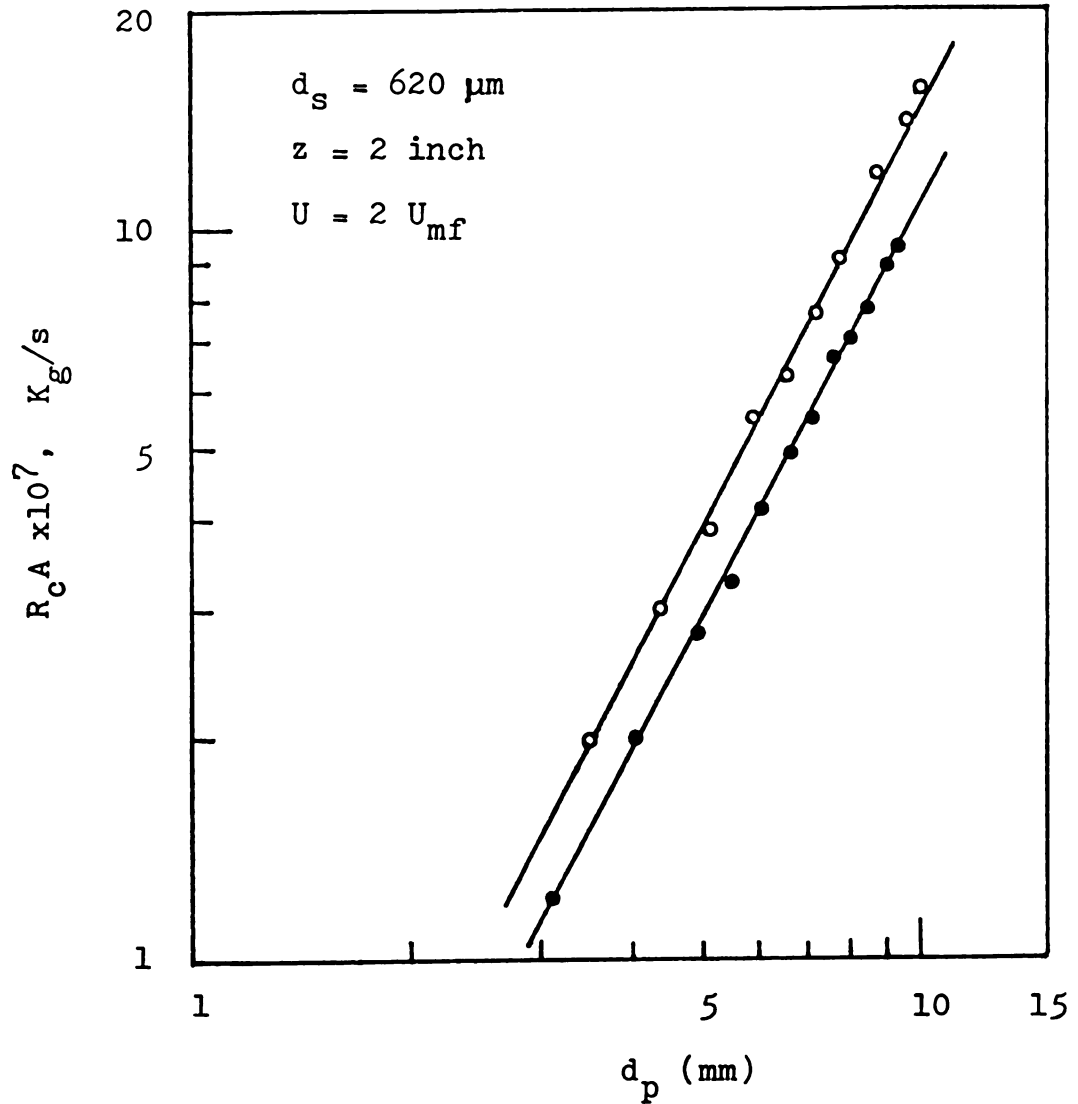


Figure 2.10 Overall combustion rate versus particle diameter ( $T_B = 1163 \text{ K}$ ,  $U_o = 22.6 \text{ m/s}$ ; dilute phase (o), dense phase (●)).

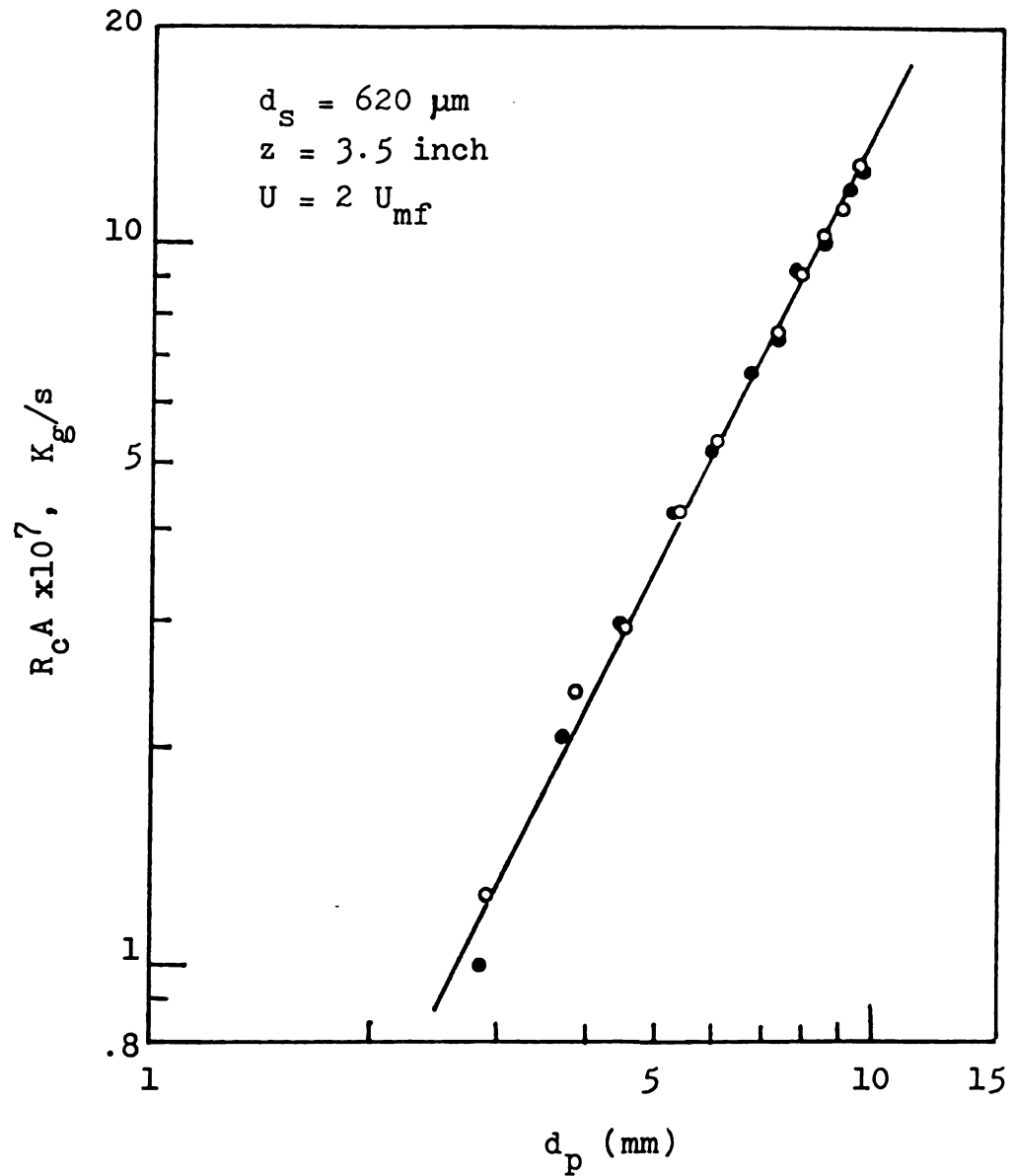


Figure 2.11 Overall combustion rate versus particle diameter ( $T_B = 1163 \text{ K}$ ,  $U_o = 22.6 \text{ m/s}$ ; dilute phase (o), dense phase (●)).

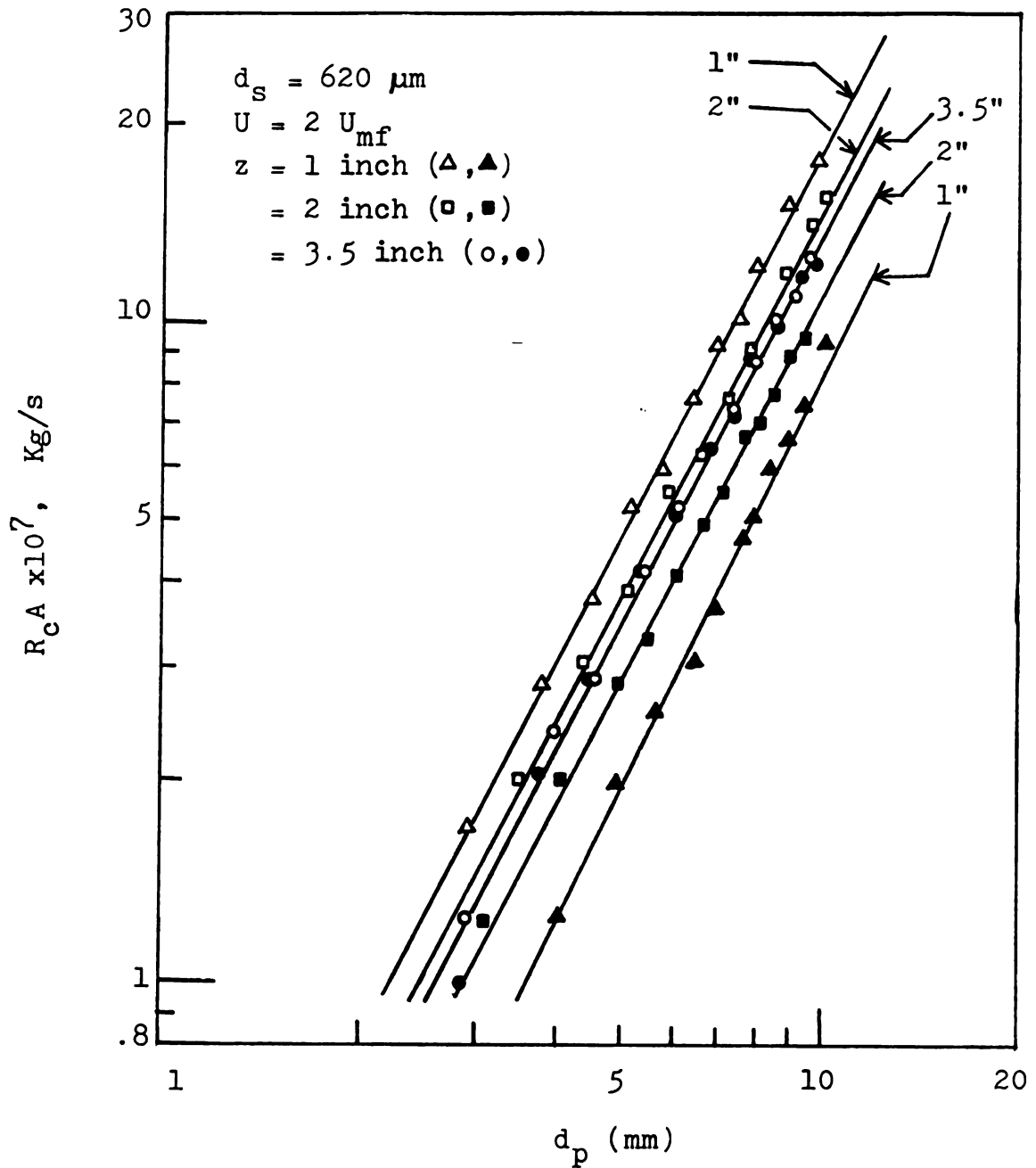


Figure 2.12 Effect of particle position on overall combustion rate ( $T_B = 1163 \text{ K}$ ,  $U_o = 22.6 \text{ m/s}$ ; dilute phase (open symbols), dense phase (closed symbols)).

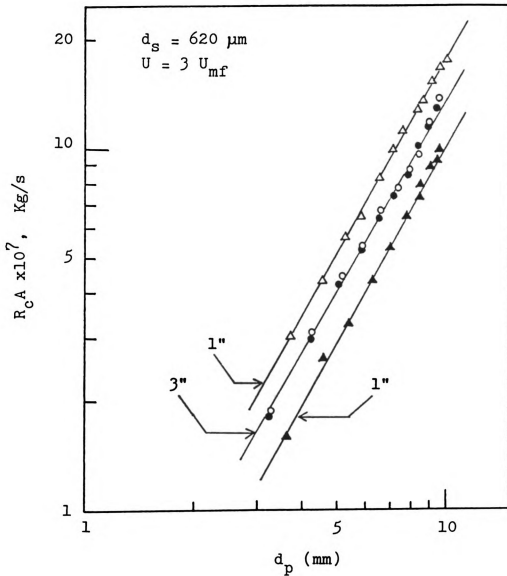


Figure 2.13 Overall combustion rate versus particle diameter ( $T_B = 1163 \text{ K}$ ,  $U_o = 33.8 \text{ m/s}$ ; dilute phase (open symbols), dense phase (closed symbols) ).

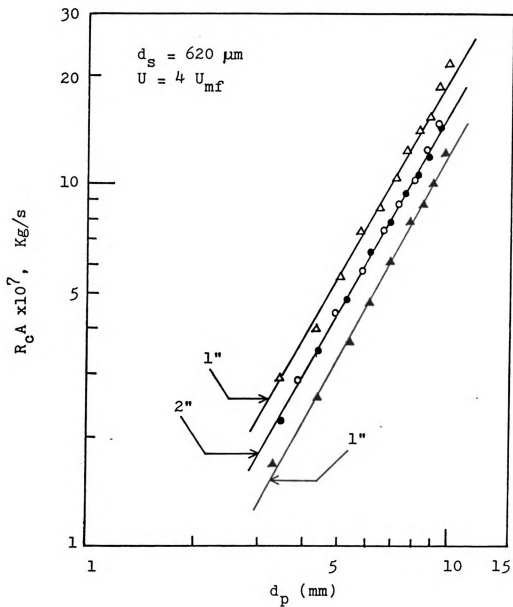


Figure 2.14 Overall combustion rate versus particle diameter ( $T_B = 1163 \text{ K}$ ,  $U_o = 45.2 \text{ m/s}$ ; dilute phase (open symbols), dense phase (closed symbols) ).

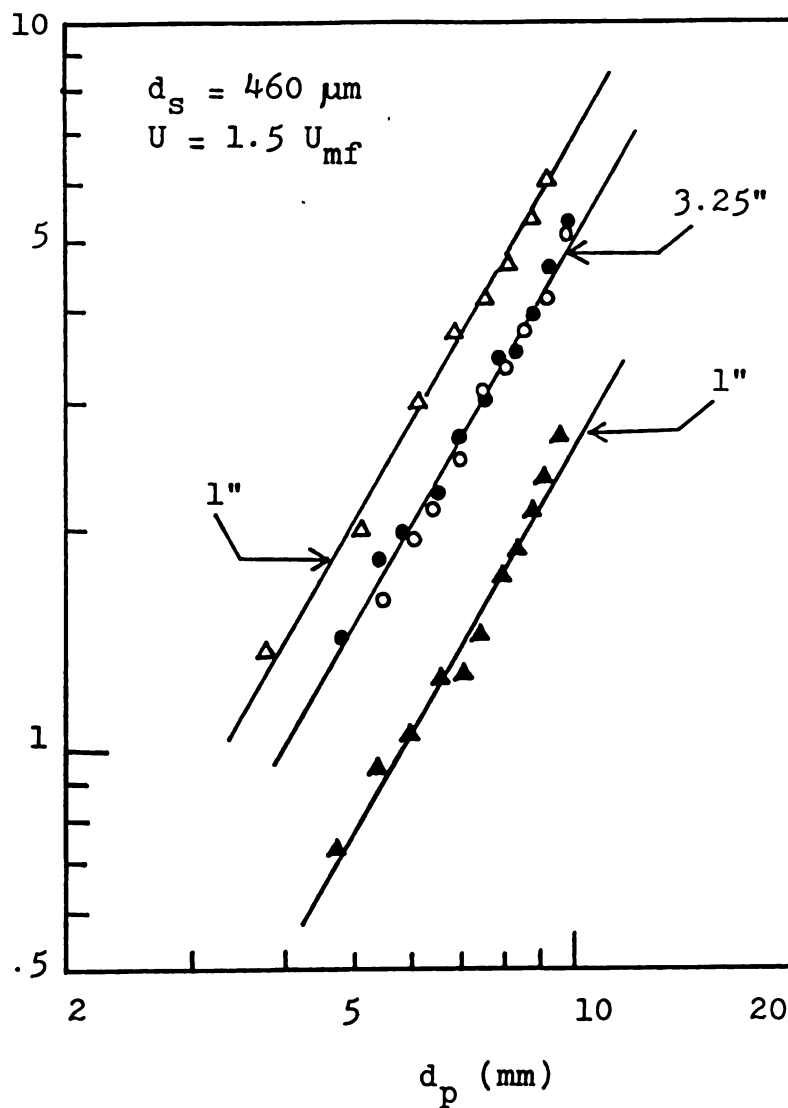


Figure 2.15 Overall combustion rate versus particle diameter ( $T_B = 1163 \text{ K}$ ,  $U_o = 9.4 \text{ m/s}$ ; dilute phase (open symbols), dense phase (closed symbols)).

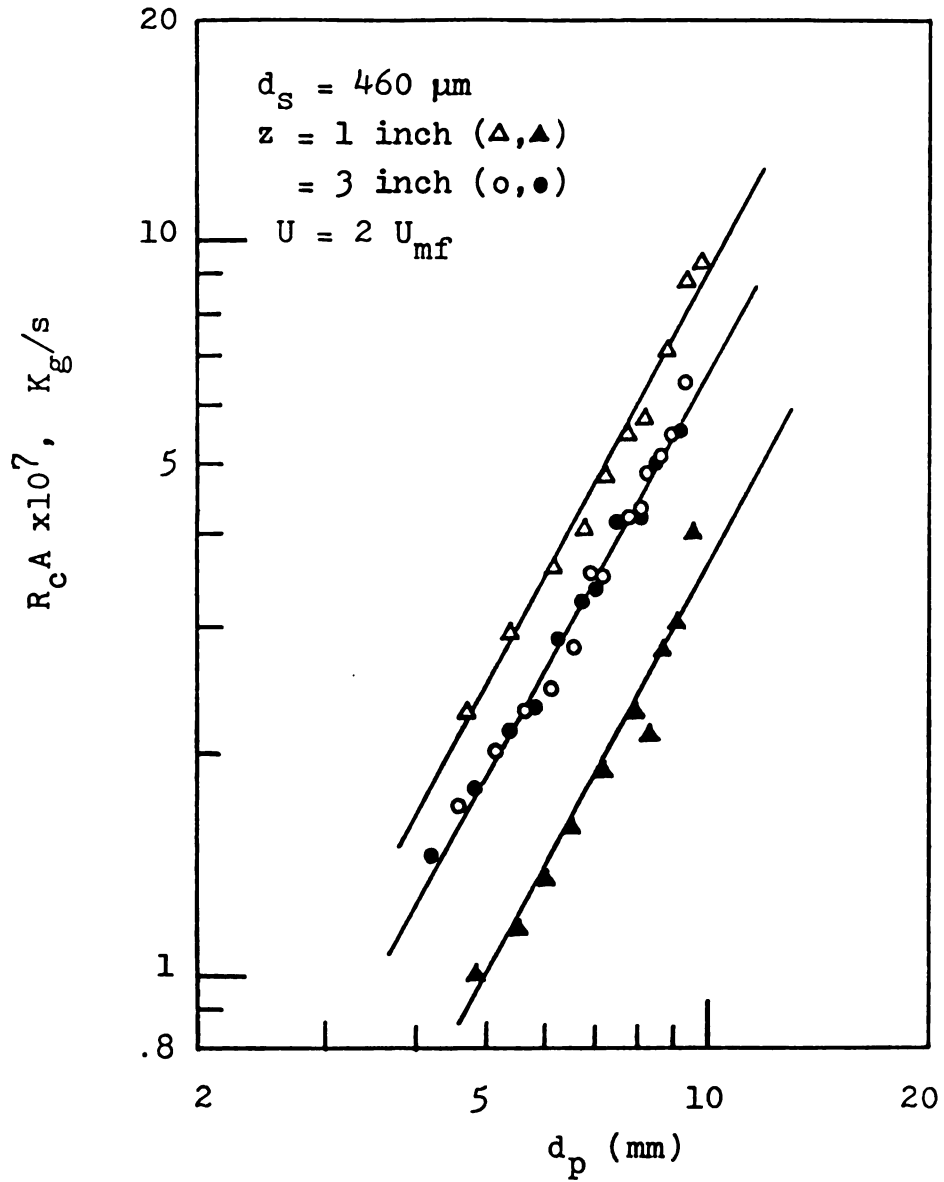


Figure 2.16 Overall combustion rate versus particle diameter ( $T_B = 1163 \text{ K}$ ,  $U_O = 12.5 \text{ m/s}$ ; dilute phase (open symbols), dense phase (closed symbols)).

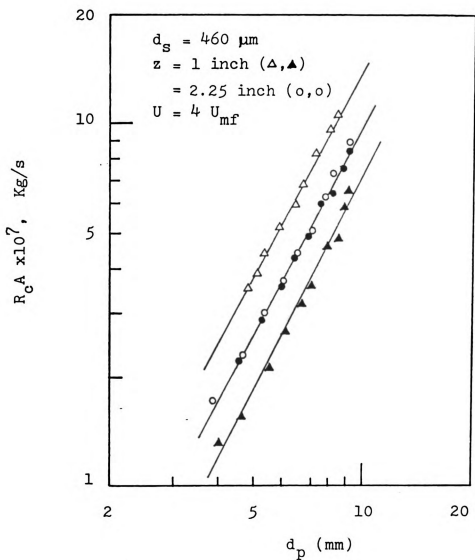


Figure 2.17 Overall combustion rate versus particle diameter ( $T_B = 1163 \text{ K}$ ,  $U_o = 25.0 \text{ m/s}$ ; dilute phase (open symbols), dense phase (closed symbols)).

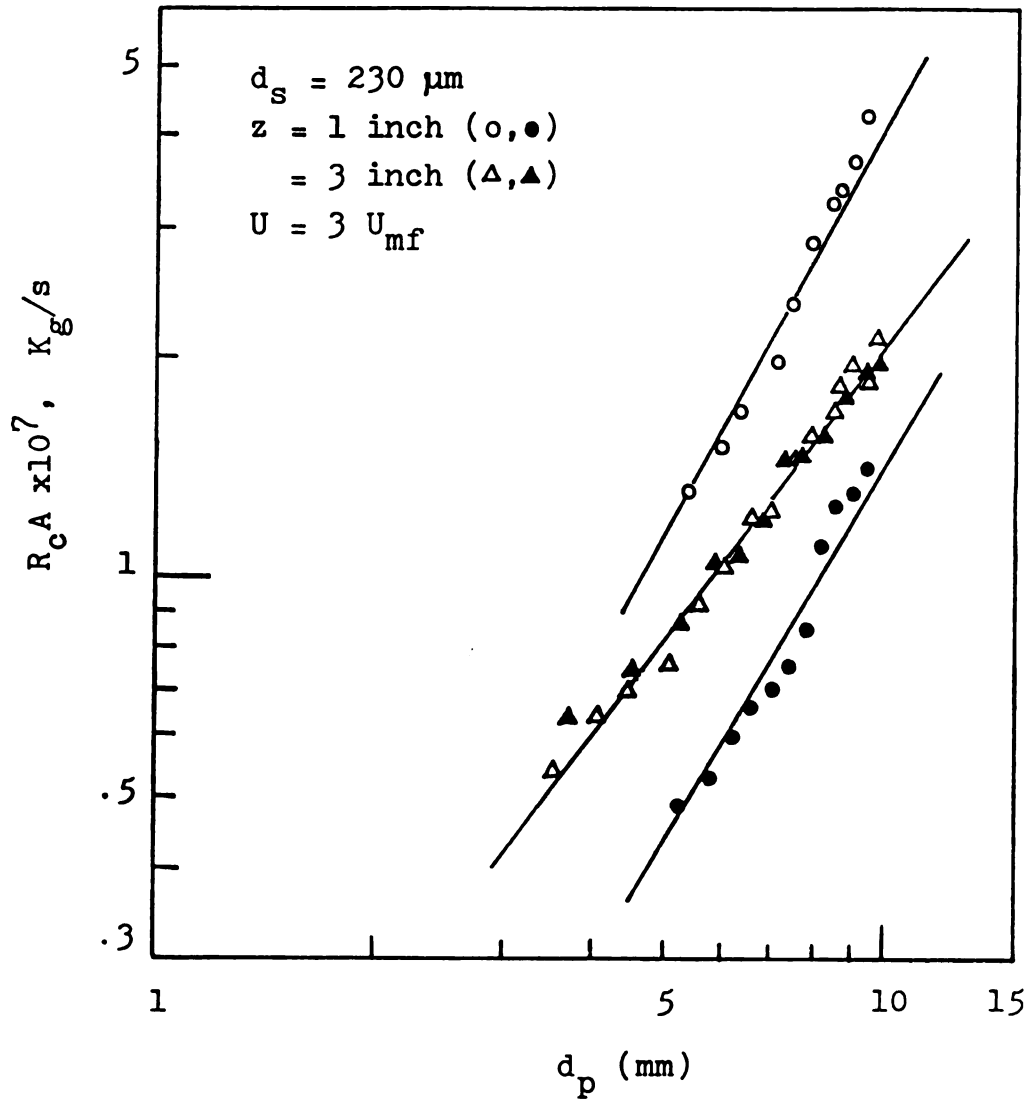


Figure 2.18 Overall combustion rate versus particle diameter ( $T_B = 1163 \text{ K}$ ,  $U_o = 4.7 \text{ m/s}$ ; dilute phase (open symbols), dense phase (closed symbols)).

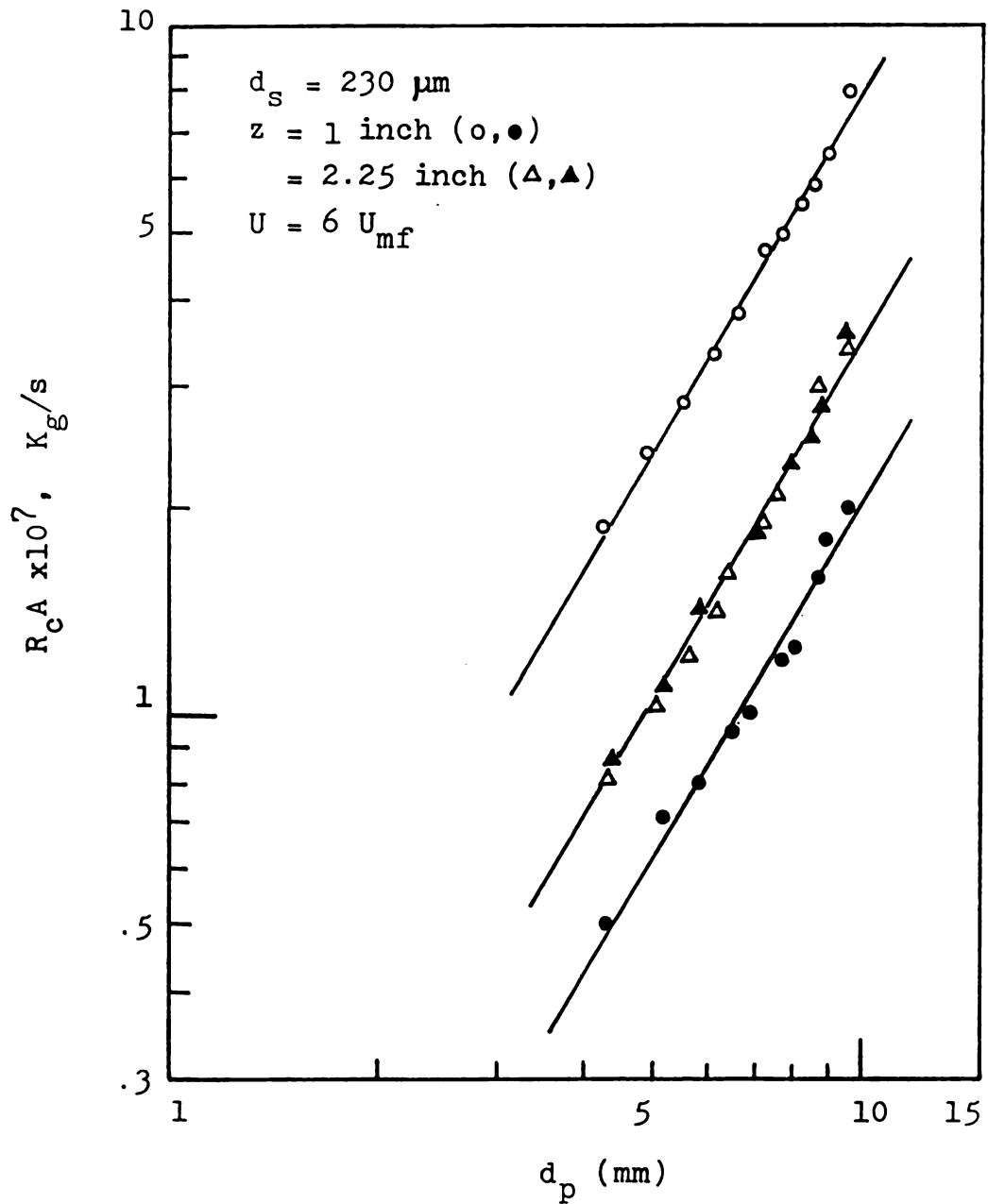


Figure 2.19 Overall combustion rate versus particle diameter ( $T_B = 1163 \text{ K}$ ,  $U_o = 9.4 \text{ m/s}$ ; dilute phase (open symbols), dense phase (closed symbols) ).

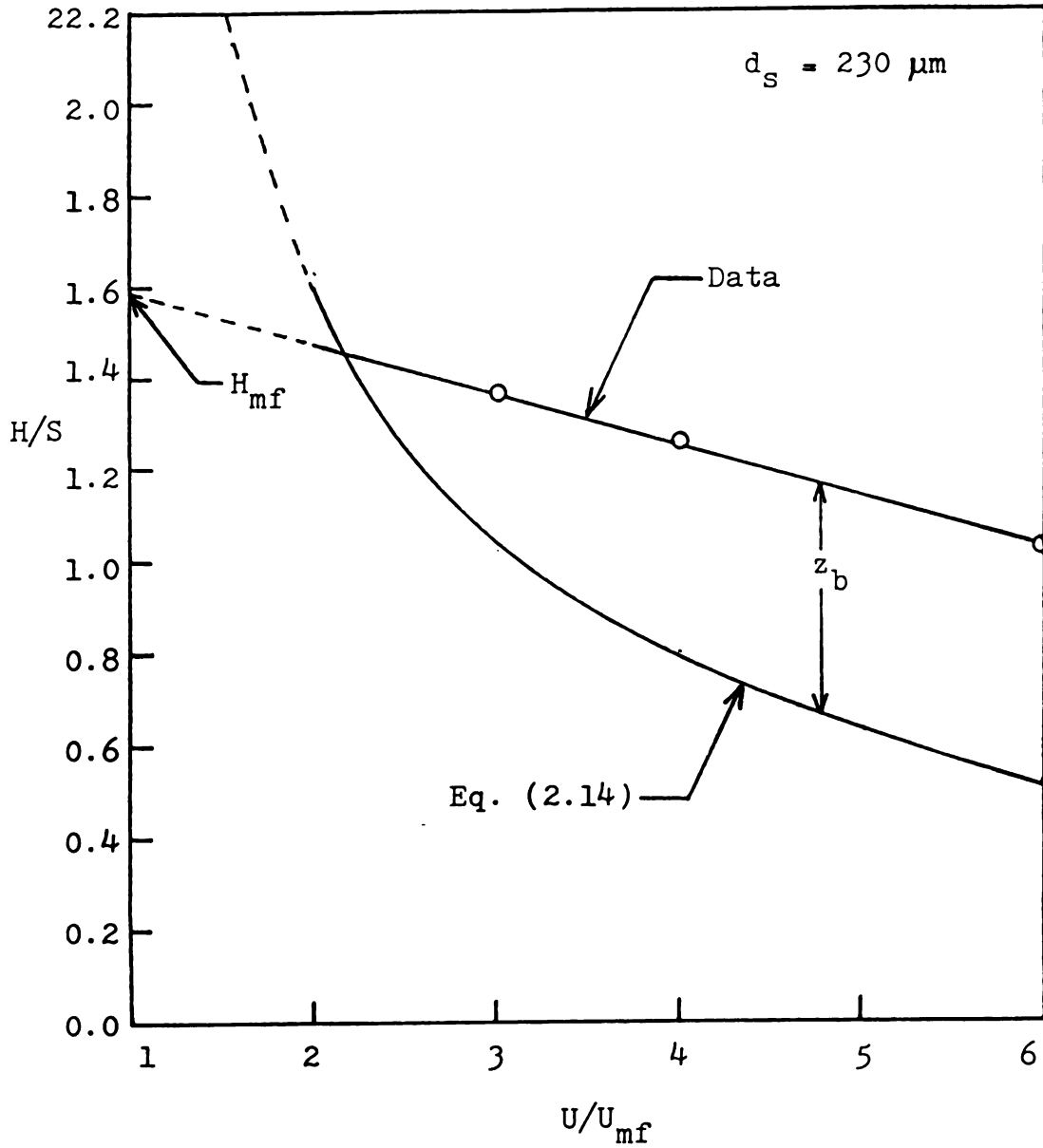


Figure 2.20 Ratio of grid region height to pitch size versus  $U/U_{mf}$ ,  $T_B = 1163 \text{ K}$ .

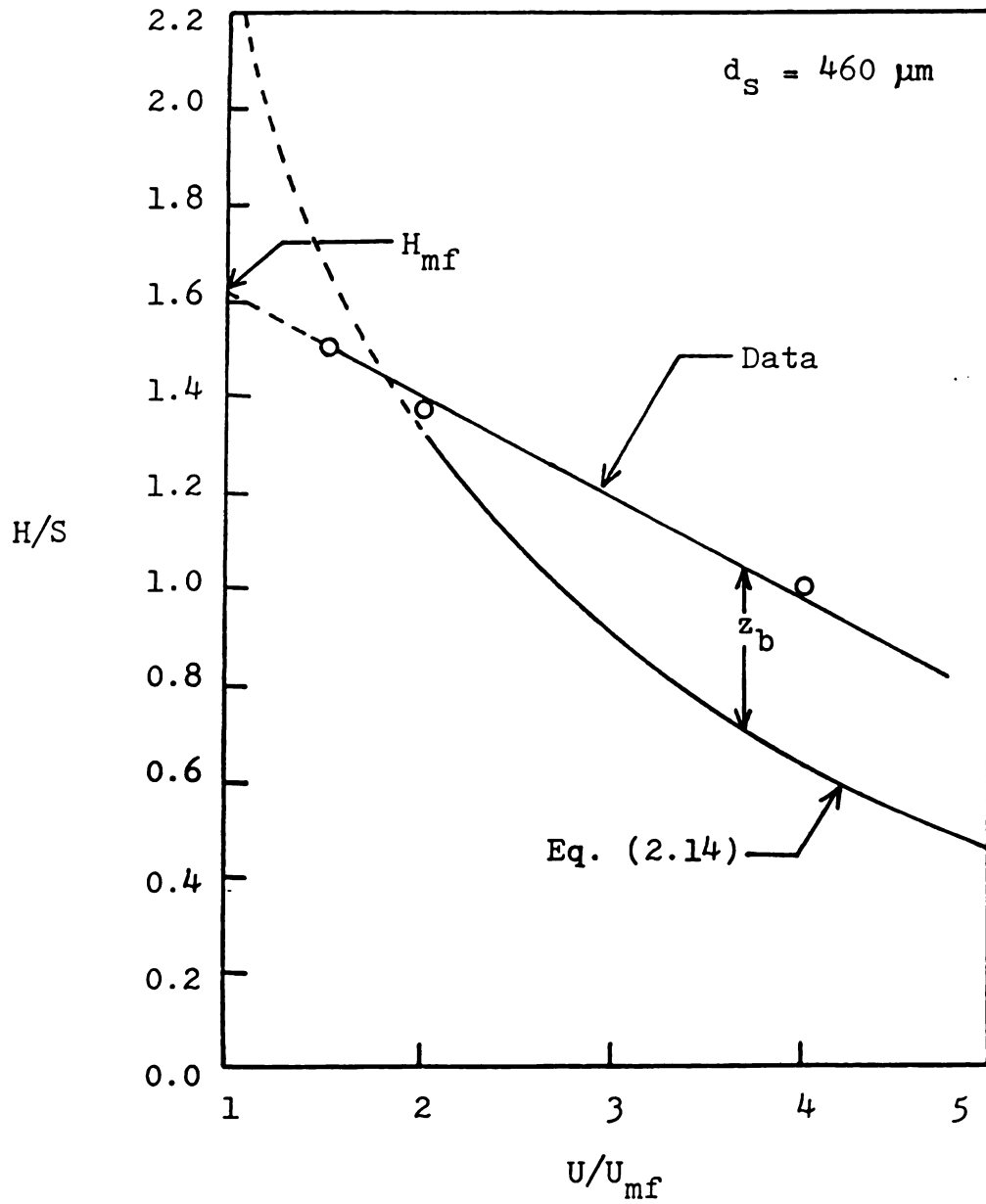


Figure 2.21 Ratio of grid region height to pitch size versus  $U/U_{mf}$ ,  $T_B = 1163 \text{ K}$ .

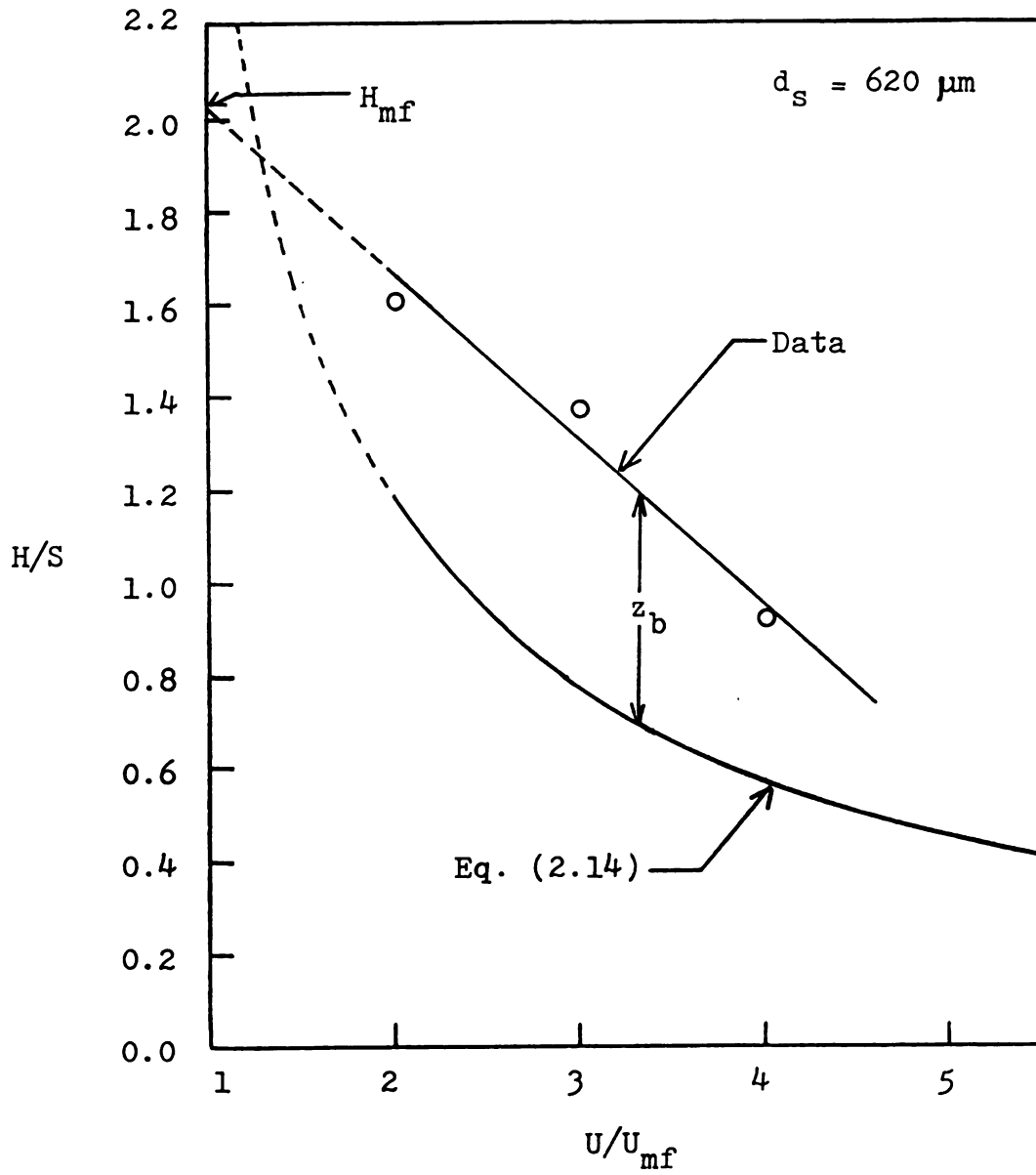


Figure 2.22 Ratio of grid region height to pitch size versus  $U/U_{mf}$ ,  $T_B = 1163 \text{ K}$ .

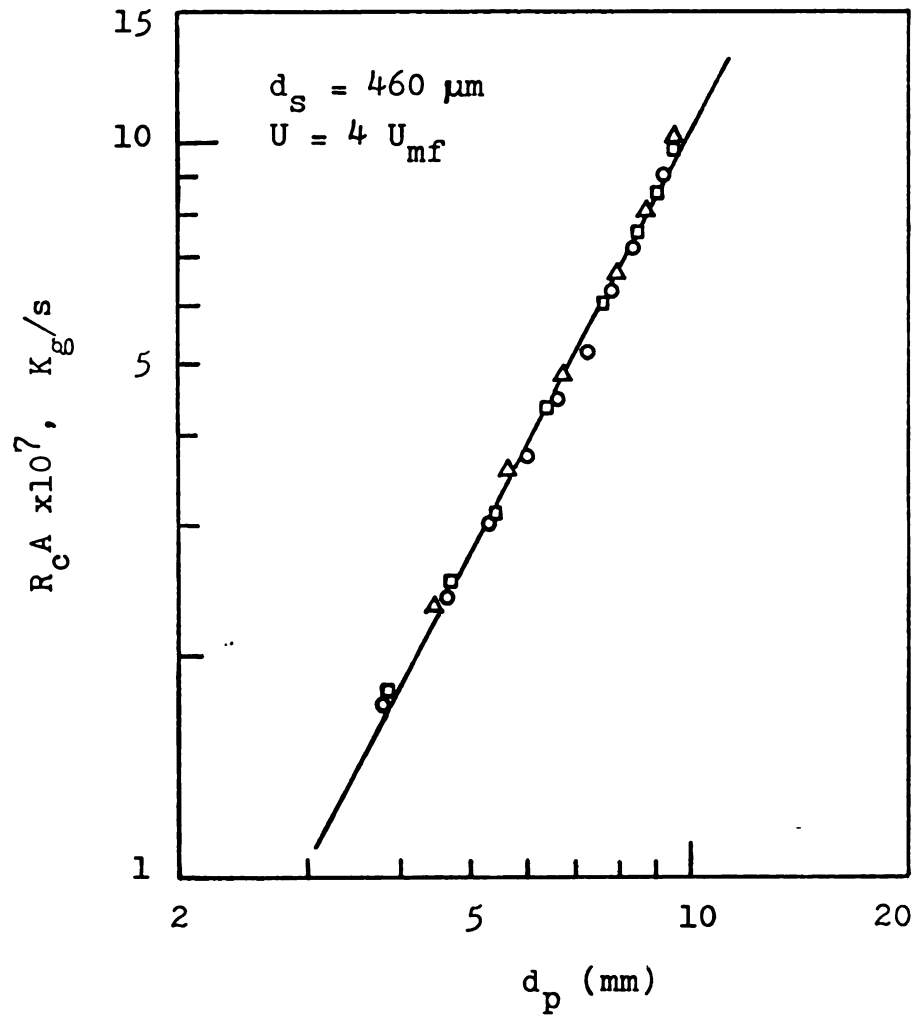


Figure 2.23 Effect of particle position on overall combustion rate in the bubbling region ( $T_B = 1163 \text{ K}$ ,  $U_o = 25.0 \text{ m/s}$ ; 2.25 inch (o), 3 inch (□), 4 inch (Δ)).

### 2-6-3. Mass transfer characteristics of fixed carbon samples

As discussed in Section 2-6-2, the mass transfer resistance in the dilute phase is expected to increase with increasing vertical distance from the distributor due to solids entrainment and gas leakage throughout the jet height. On the other hand, the reverse trend should hold in the dense phase. These trends have been verified experimentally and the typical results are shown in Figures 2.24 - 2.27.

It is further indicated by Figures 2.26 and 2.27 that at the grid region height, as determined in Section 2-6-2, not only the overall combustion rate but the mass transfer resistance of the dilute phase are the same as those of the dense phase. Hence, it can be concluded that the mass transfer resistance as well as the overall combustion rate of fixed carbon samples should be independent of the sample position above the grid region height, due to the uniformity of the bubbling region. Figure 2.28 indeed shows that to be the case, thus substantiating the validity of  $H$ , as defined in Section 2-3, in the modeling study. It should be noted here that for a carbon sample moving freely in the bubbling region, the actual values of both overall combustion rate and mass transfer coefficient are lower than those depicted in Figures 2.23 and 2.28 under the same operating conditions. This is because fixed carbon samples are under the constant influence of bubbles, which increases both rates. Using the first principles and the theories of spouted beds, mass transfer correlations are developed from experimental Sherwood numbers in Chapter 3.

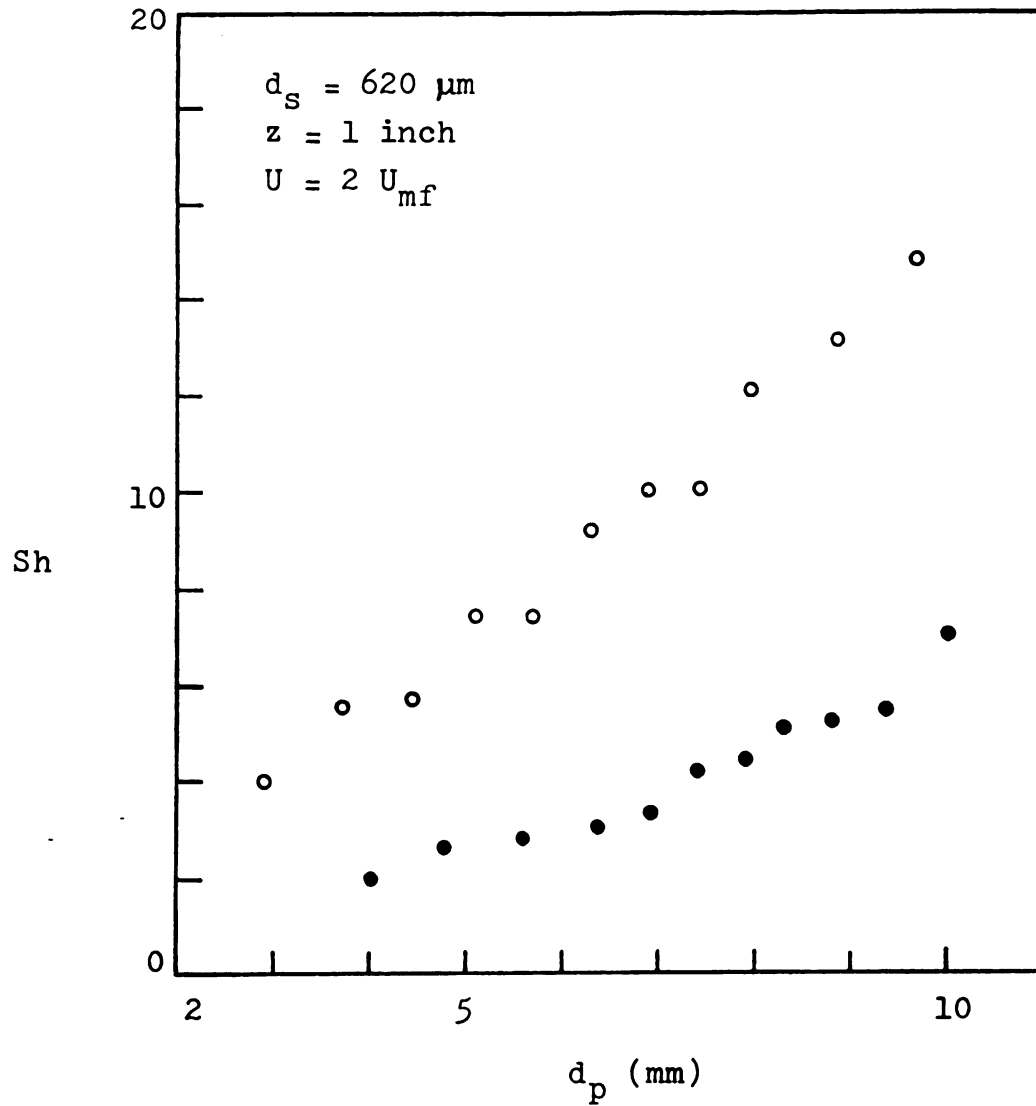


Figure 2.24 Variations in Sherwood number with particle diameter ( $T_B = 1163 \text{ K}$ ,  $U_o = 22.6 \text{ m/s}$ ; dilute phase (o), dense phase (●) ).

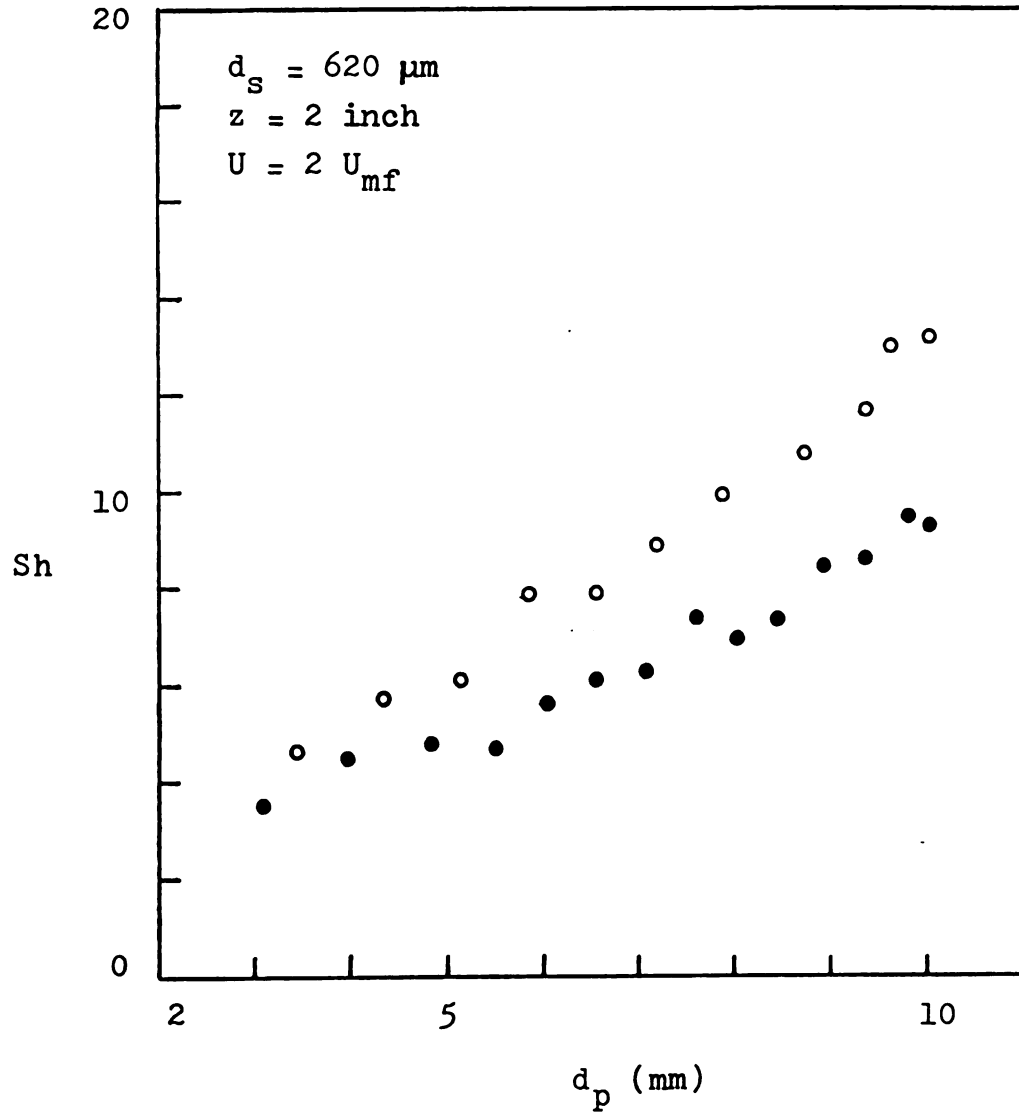


Figure 2.25 Variations in Sherwood number with particle diameter ( $T_B = 1163 \text{ K}$ ,  $U_o = 22.6 \text{ m/s}$ ; dilute phase (o), dense phase (●) ).

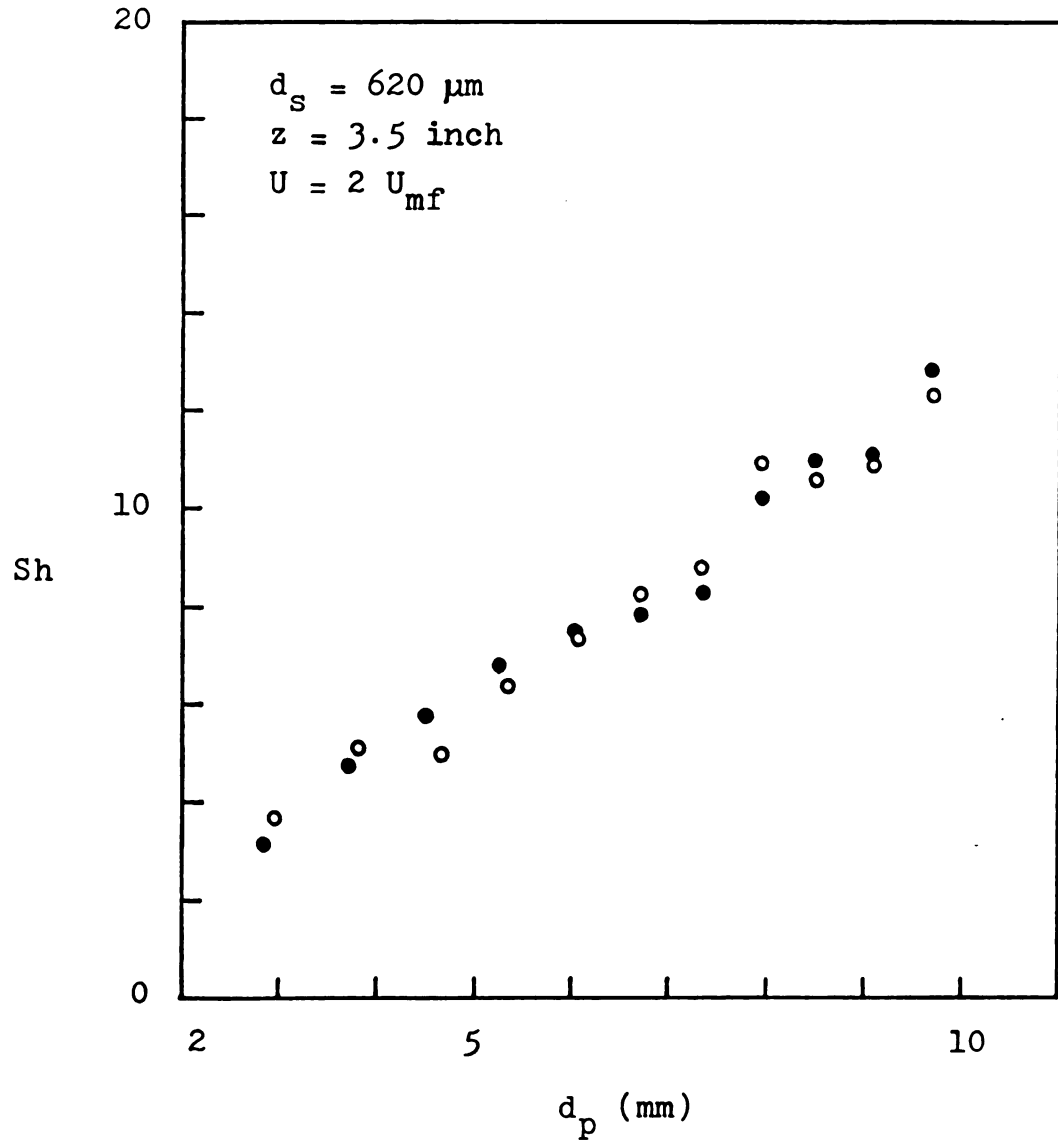


Figure 2.26 Variations in Sherwood number with particle diameter ( $T_B = 1163 \text{ K}$ ,  $U_o = 22.6 \text{ m/s}$ ; dilute phase (o), dense phase (●)).

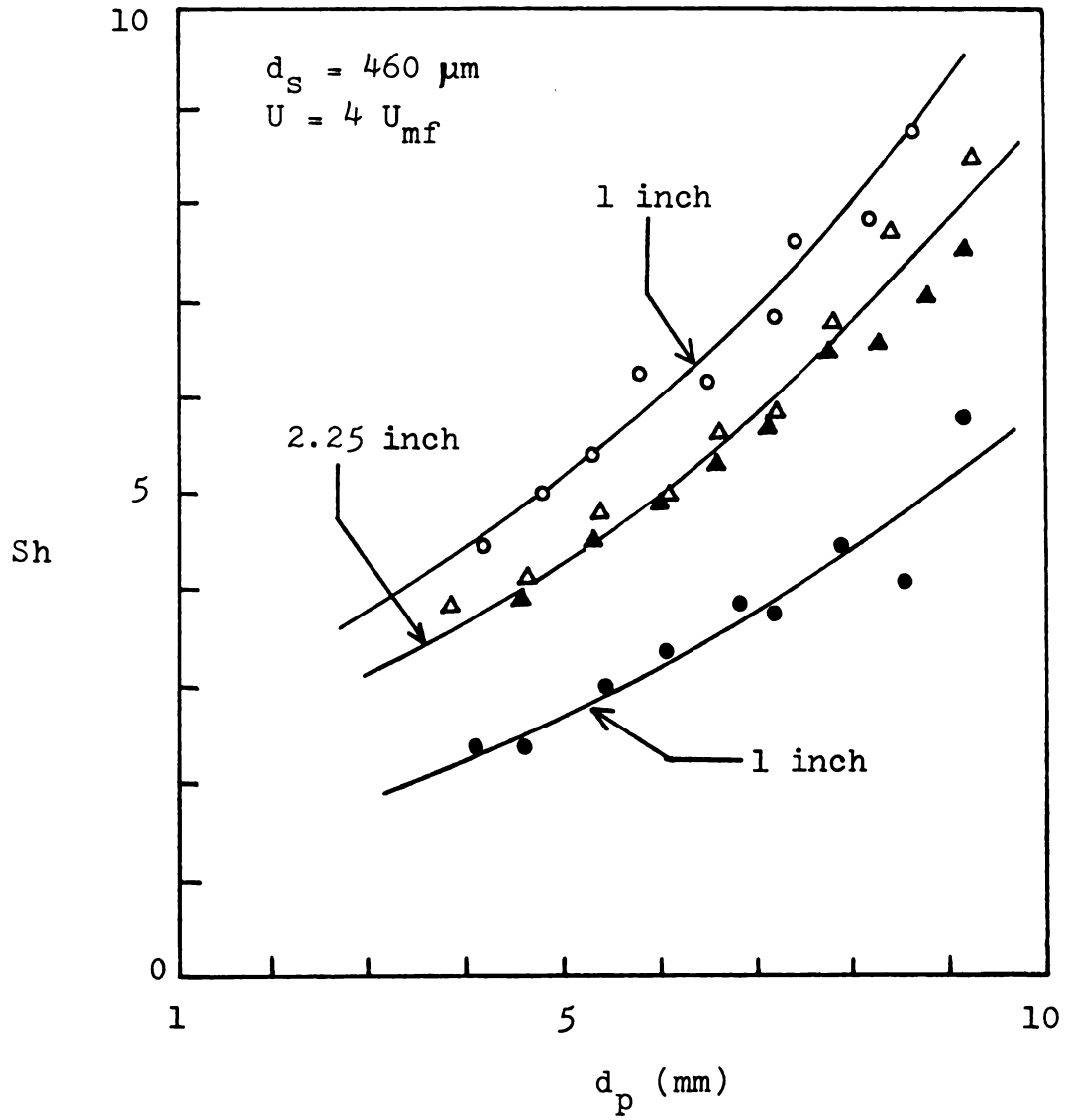


Figure 2.27 Effect of particle position on Sherwood number ( $T_B = 1163 \text{ K}$ ,  $U_o = 25.0 \text{ m/s}$ ; dilute phase (open symbols), dense phase (closed symbols)).

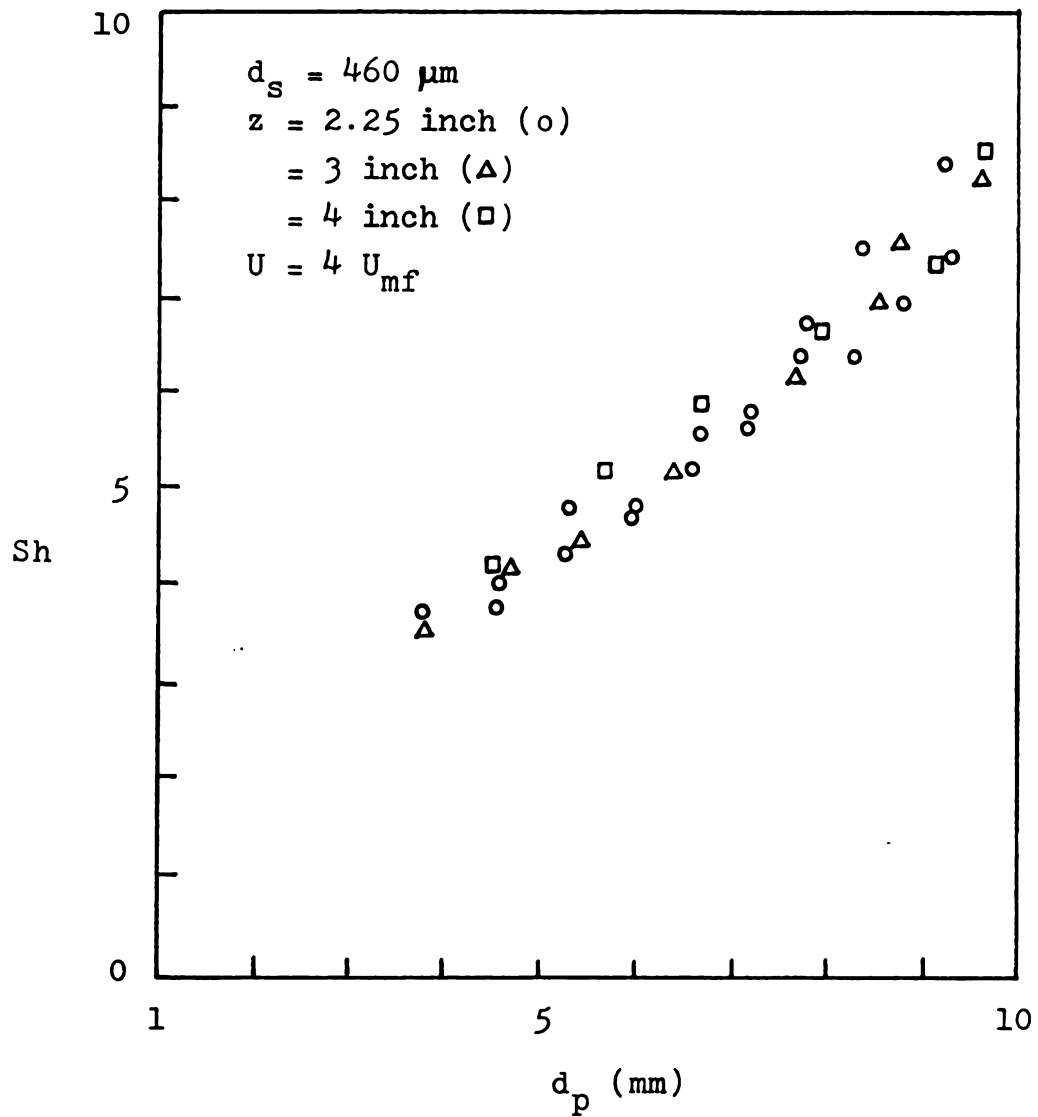


Figure 2.28 Effect of particle position on Sherwood number above grid region height ( $T_B = 1163 \text{ K}$ ,  $U_o = 25.0 \text{ m/s}$ ).

#### 2-6-4. Effects of superficial air velocity on $R_c$ , $A$ and $Sh$

For all inert particle sizes considered in this study, the overall combustion rate has been found to increase with increasing  $U$  both in the dilute and in the dense phase, as shown in Figure 2.29 for  $620 \mu\text{m}$  sand. Figure 2.30 also shows that for the same inert particle size of  $620 \mu\text{m}$ , the increase in  $U$  has no effect on the mass transfer resistance in the dilute phase. Hence, according to Eq.(2.9), the increase in  $R_c$  must be compensated by the corresponding increase in the degree of mass transfer control,  $\phi$ , in order for the Sherwood number to remain the same. In other words, the chemical rate must increase with increasing  $U$ , and this is shown in Figure 2.31 by the significant increase in  $T_p$  in the dilute phase. It is further shown in Figure 2.31 that the increase in  $T_p$  with increasing  $U$  is much less significant in the dense phase. Hence, the increase in the overall combustion rate of the dense phase must be reflected upon the decrease in the mass transfer resistance with increasing  $U$ , and this is shown in Figure 2.32 by the significant increase in the Sherwood number with increasing  $U$ .

For  $230 \mu\text{m}$  sand, the mass transfer resistance is shown in Figure 2.33 to decrease considerably with increasing  $U$  in the dilute phase, while the effect of  $U$  on the mass transfer resistance is small in the dense phase. It should be noted that this trend is generally opposite to what has been observed for  $620 \mu\text{m}$  sand. For  $460 \mu\text{m}$  sand, the mass transfer resistance is shown in Figures 2.34 and 2.35 to decrease

considerably with increasing  $U$  both in the dilute and in the dense phase.

Therefore, in the dilute phase of large inert particles, the overall combustion rate is affected by  $U$  due to the change in the chemical rate. As the inert particle size decreases, the influence of the chemical kinetics diminishes, and the overall combustion rate is affected by  $U$  mainly due to the change in the mass transfer resistance in a bed of small inert particles. In the dense phase, the corresponding trend is opposite to what has been stated for the dilute phase above.

Prins et al. (9) observed that for all inert particle sizes, the mass transfer resistance is independent of  $U$  in the bubbling region in which a burning carbon particle spend most of its time in the particulate phase. This finding is consistent with the two-phase theory of fluidization (19) which states that the gas flow in excess of that required for minimum fluidization passes through the bed in the form of bubbles. As shown in Eq. (2.10), the minimum fluidization velocity strongly depends upon the particle size and, to a less extent, the particle density. As the inert particle size increases, it thus becomes more difficult to fluidize the dense phase, and a larger portion of the gas flow entering the bed must leak into the dense phase. Therefore, it seems that for 620  $\mu\text{m}$  sand, the increase in  $U$  up to  $4 U_{mf}$  has no significant effect on the mass transfer resistance of the dilute phase due to a significant gas leakage, as shown in Figure 2.30. This result further suggests that the amount of gas leakage is considerably more than what is required to fluidize the dense phase,

which is in essence consistent with the conclusion by Yates et al. (18); the dense phase voidage increases beyond its minimum value briefly during the bubble formation.

By the same analogy, it is relatively easy to fluidize the dense phase of small inert particles, and much of the gas flow entering the bed remains in the jet to decrease the mass transfer resistance of the dilute phase, while the dense phase is little affected by  $U$ , as shown in Figure 2.23 for 230  $\mu\text{m}$  sand. For 460  $\mu\text{m}$  sand, the gas leakage is relatively moderate, and the influence of  $U$  is significant in both regions, as shown in figures 2.34 and 2.35. The relative difficulty of fluidizing the dense phase can also be seen in Table 2.5 by noting that the value of  $H_{mf}$  increases with increasing inert particle size.

Furthermore, the minimum fluidization velocity appears to play a rather important role in an implicit manner also in the grid region, since the process of fluidizing the dense phase influences significantly the distribution of the gas flow between the dilute and the dense phase and possibly the solids entrainment rate as well.

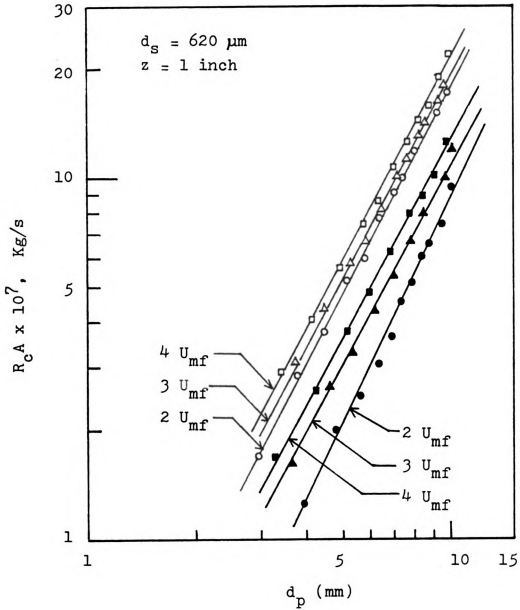


Figure 2.29 Effects of  $U$  on overall combustion rate ( $T_B = 1163 \text{ K}$ , dilute (open symbols), dense phase (closed symbols)).

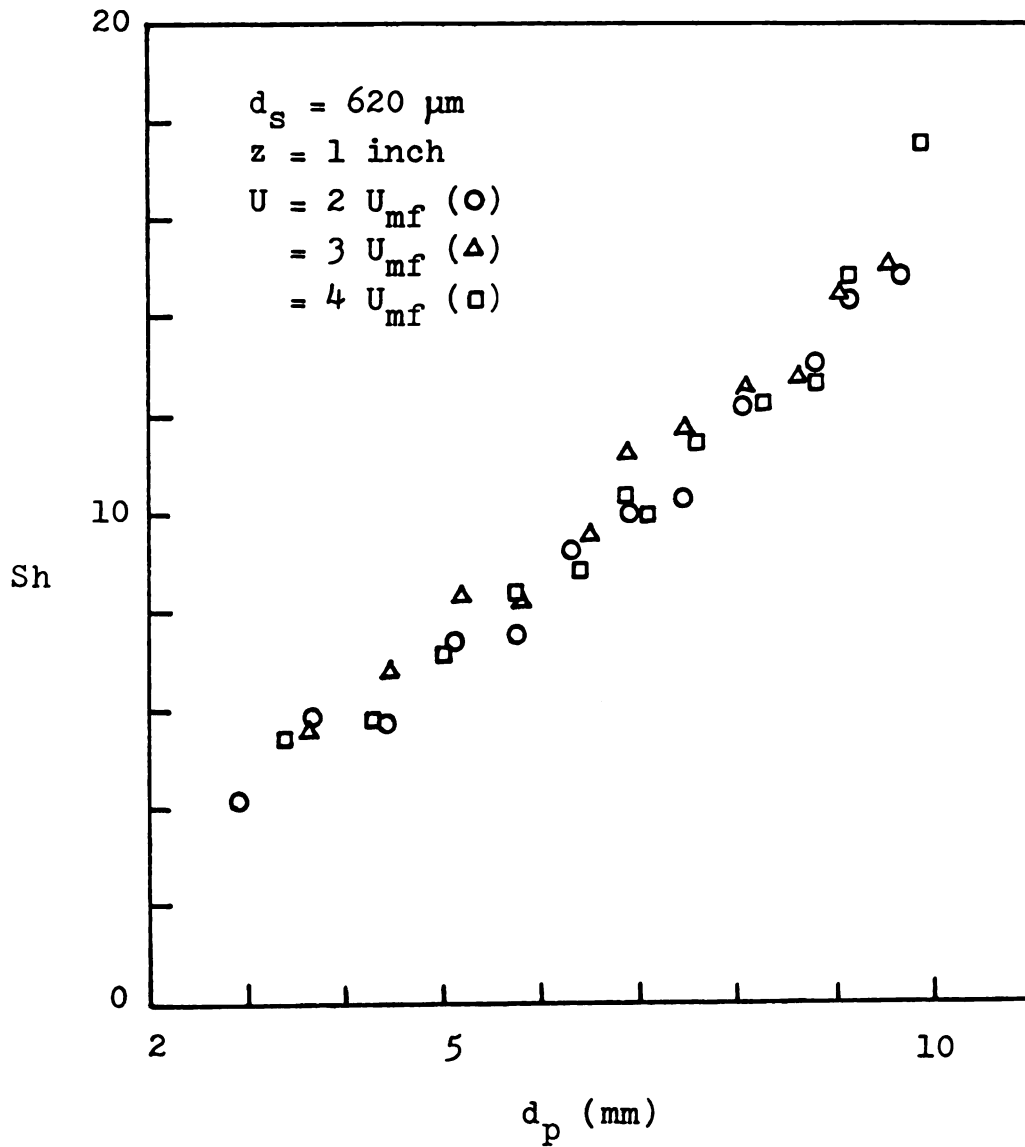


Figure 2.30 Effects of  $U$  on the Sherwood number in the dilute phase ( $T_B = 1163 \text{ K}$ ).

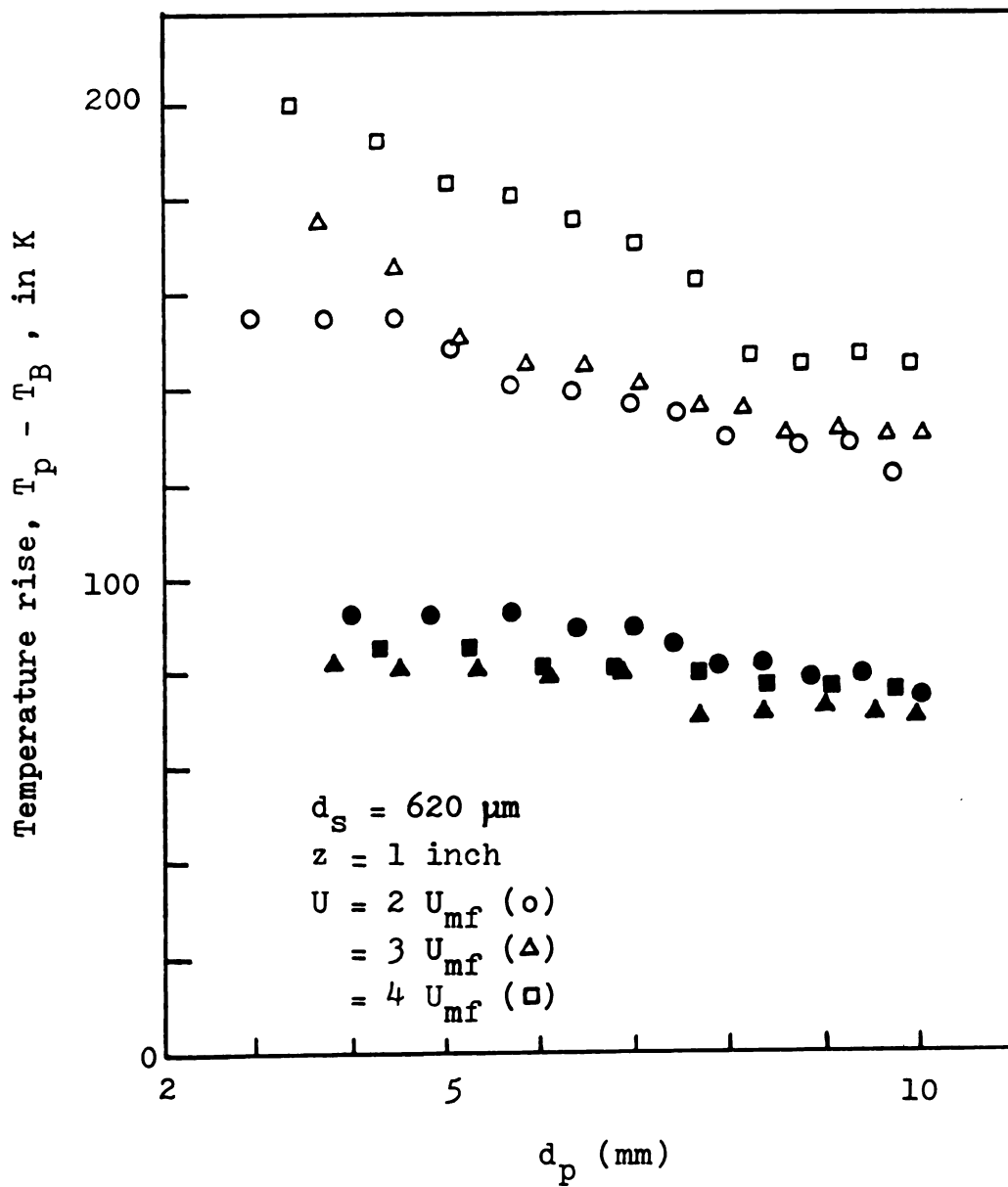


Figure 2.31 Temperature rise above bed temperature ( $T_B = 1163 \text{ K}$ , dilute phase (open symbols), dense phase (closed symbols) ).

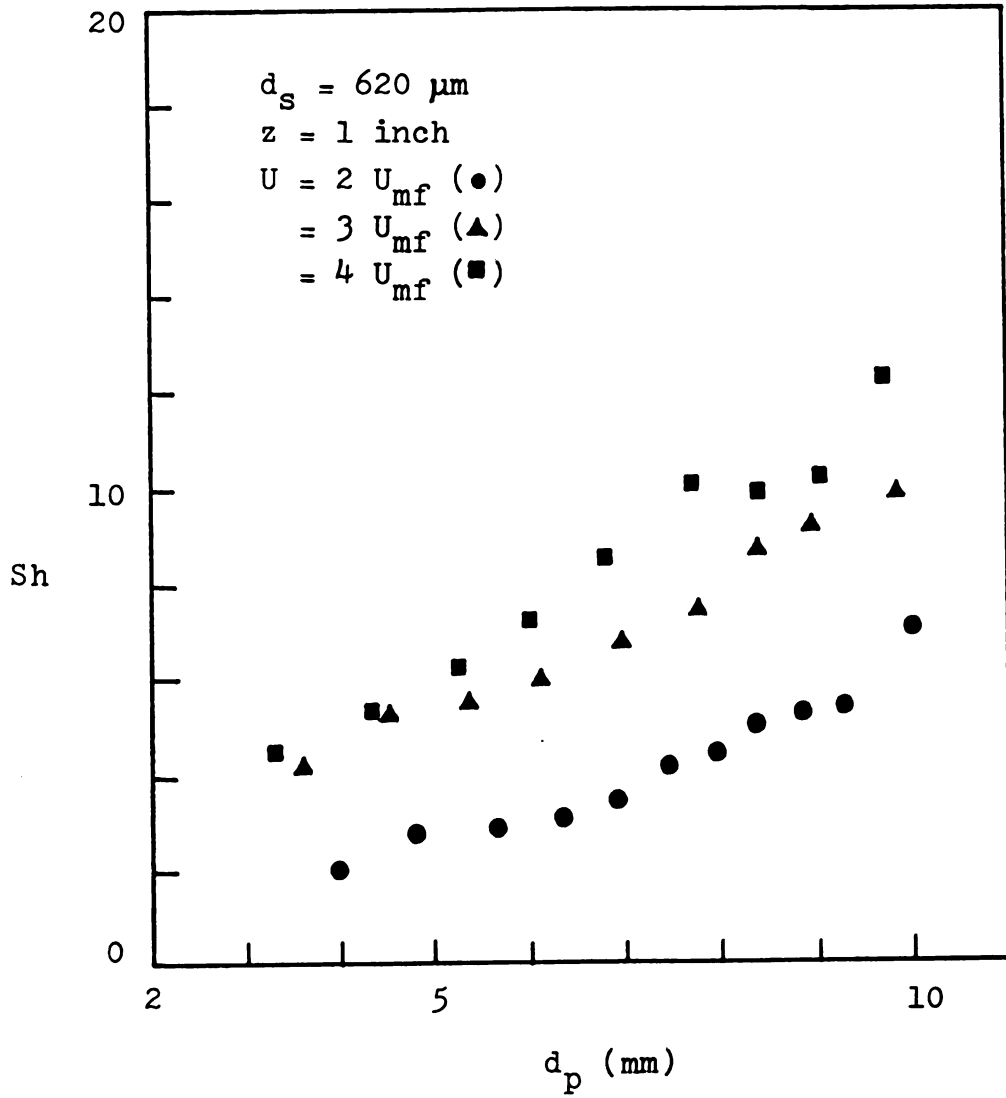
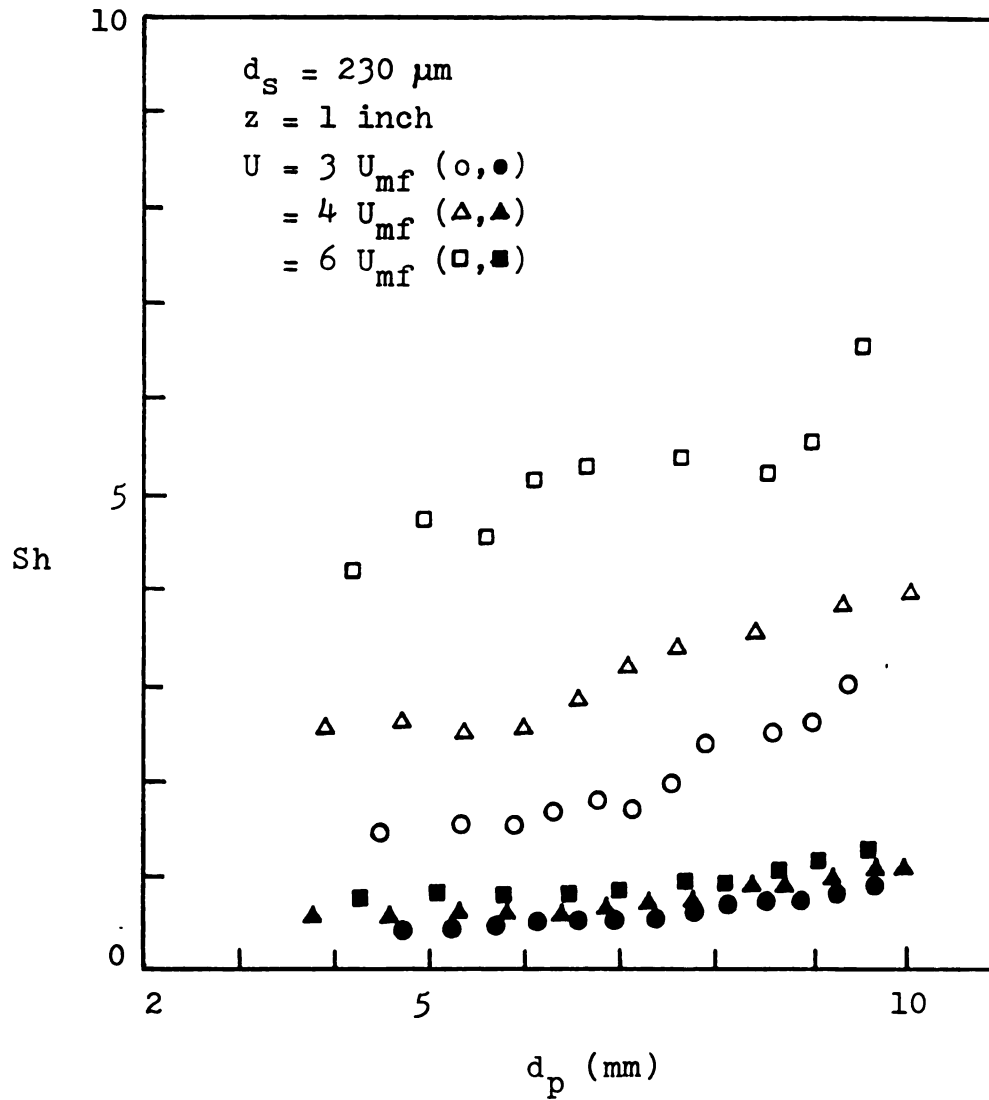


Figure 2.32 Effects of  $U$  on the Sherwood number in the dense phase ( $T_B = 1163 \text{ K}$ ).



**Figure 2.33** Effects of  $U$  on the Sherwood number  
 (  $T_B = 1163 \text{ K}$ , dilute phase (open  
 symbols), dense phase (closed symbols) ).

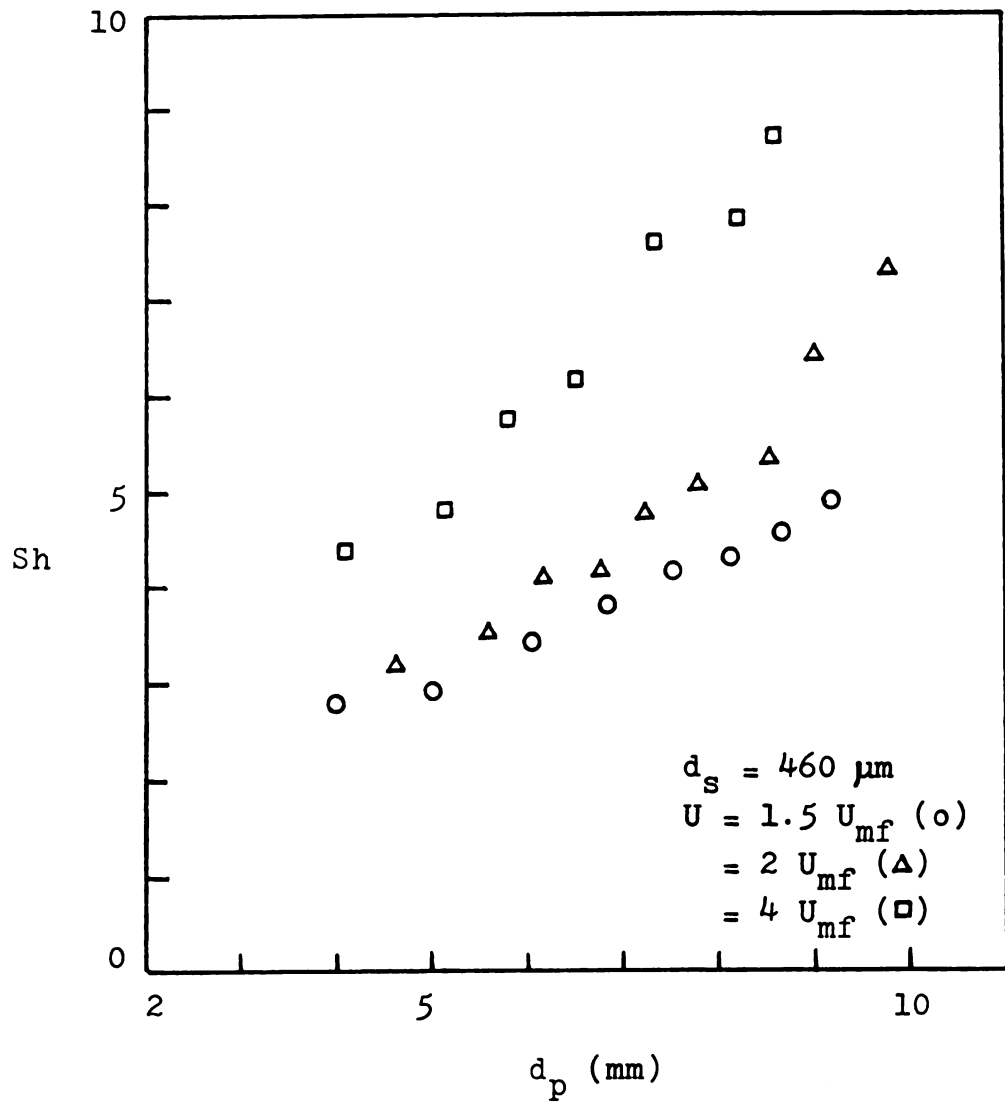


Figure 2.34 Effects of  $U$  on the Sherwood number in the dilute phase ( $T_B = 1163 \text{ K}$ ).

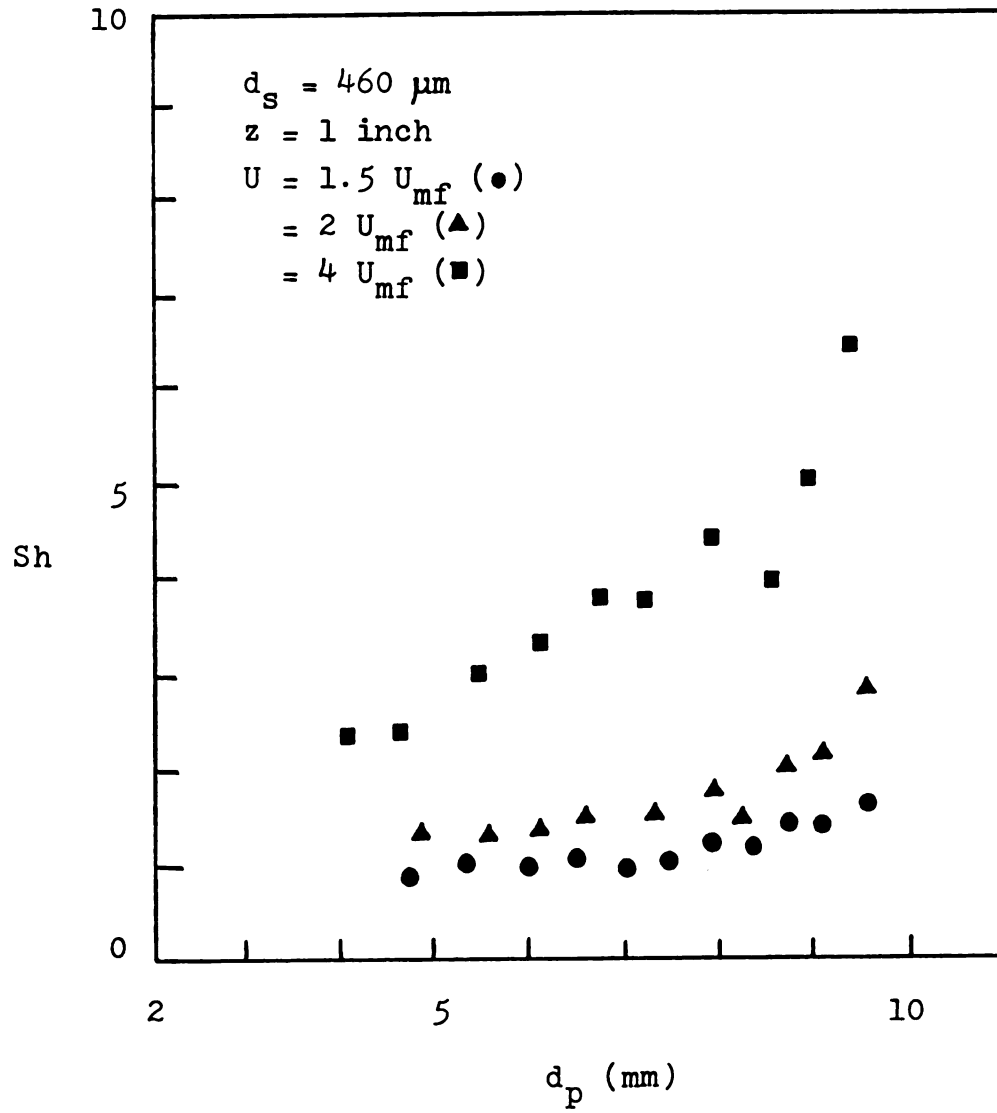


Figure 2.35 Effects of  $U$  on the Sherwood number in the dense phase ( $T_B = 1163 \text{ K}$ ).

#### 2-6-5. Effects of inert particle size on $R_c$ , $A$ and $Sh$

As shown in Table 2.1, the range of minimum fluidization velocities for the three different sized sand particles is rather large; the bed of 230  $\mu\text{m}$  sand was found experimentally to be easily slugging with considerable elutriation even at  $U$  equal to or a little above that for 620  $\mu\text{m}$  sand at minimum fluidization. It was, therefore, possible only to compare two different inert particle sizes at a time for the same superficial air velocity.

In Figure 2.36, the overall combustion rate is shown to decrease in the dilute phase, as the inert particle size increases from 230  $\mu\text{m}$  to 460  $\mu\text{m}$  at  $U = 11 \text{ cm/s}$ . Figure 2.37 shows that the decrease in the overall combustion rate is due to the increase in the mass transfer resistance with increasing inert particle size. This is expected because for larger inert particles, a smaller portion of the gas flow entering the bed remains in the dilute phase due to a higher rate of gas leakage in order to fluidize the dense phase. It will also be difficult to aerate the larger particles with a lower gas flow rate, thus decreasing the dilute phase voidage and increasing the resistance. On the other hand, the superficial gas flow rate increases with increasing inert particle size in the dense phase, and the overall combustion rate is higher for larger inert particles, as shown in Figure 2.36. Figure 2.37 further indicates that this increase in the overall combustion rate is mainly due to the increased chemical rate in the dense phase. The small decrease in the mass transfer resistance is

perhaps due to the difficulty of expanding the dense phase of larger particles.

When the Sherwood numbers are plotted against the carbon particle diameter at  $U = 4 U_{mf}$ , larger inert particles are clearly shown in Figures 2.38 and 2.39 to give higher mass transfer coefficients in both phases. It is worth noting here that similar results were obtained by Prins et al. (9). for the bubbling region in which the transfer coefficients are independent of the superficial gas velocity. On the other hand, the transfer coefficients of the grid region were shown in Section 2-6-4 to depend upon the superficial gas velocity in a rather complicated manner, and the range of  $U$  covered in Figures 2.38 and 2.39 is so large that the effect of inert particle size alone cannot be singled out as clearly as in Figures 2.36-2.37. However, one interesting observation to be made in these figures is that all experimental values of the Sherwood number, except those in the dense phase of 230  $\mu\text{m}$  sand, seem to approach a limiting value of a little less than two, which is the theoretical minimum for a single sphere in an infinite medium of stagnant fluid. Furthermore, small Sherwood numbers exhibited by 230  $\mu\text{m}$  sand seem to be related either to a significant change in the mass transfer mechanism or to the dead zone formation. These points are further examined in detail in the theoretical analyses given in Chapter 3.

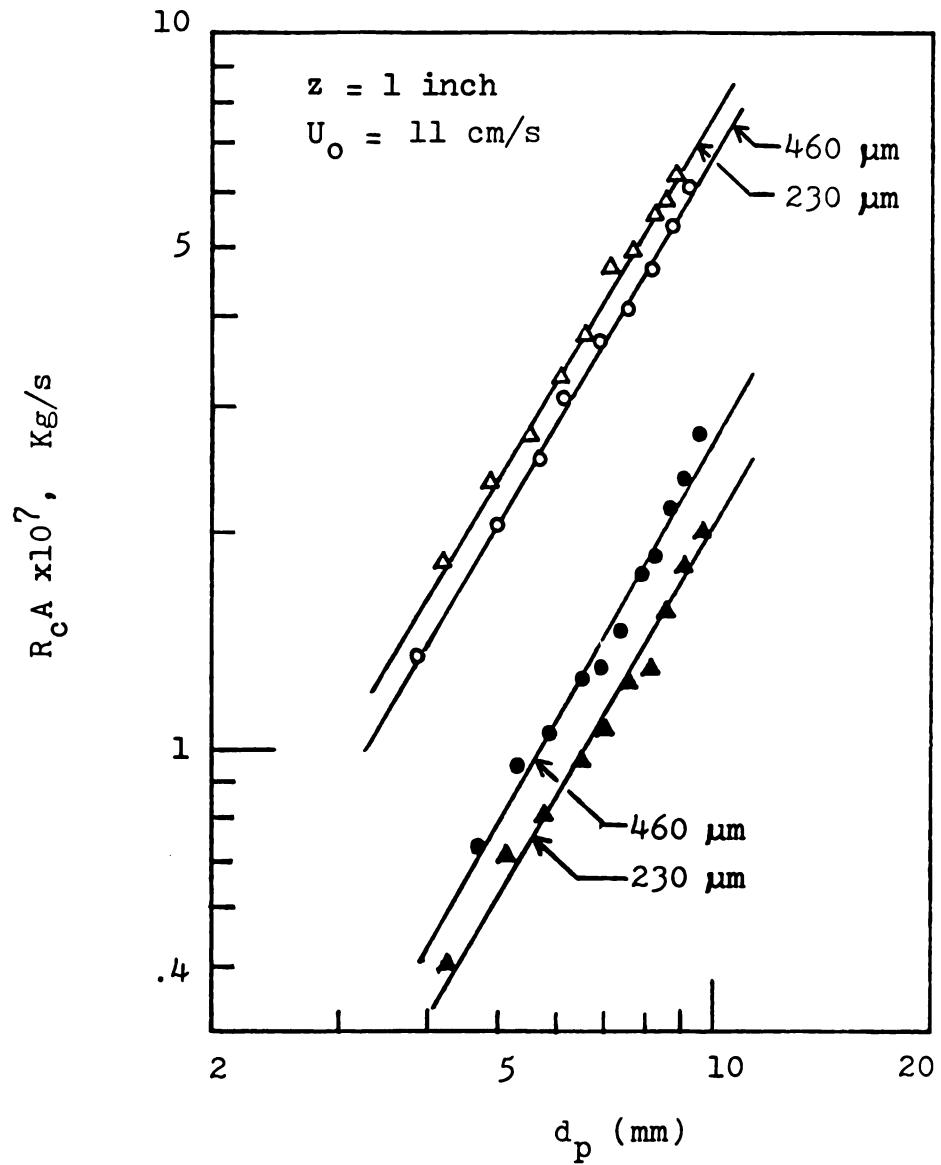


Figure 2.36 Effects of inert particle size on overall combustion rate ( $T_B = 1163$  K, dilute phase (open symbols), dense phase (closed symbols)).

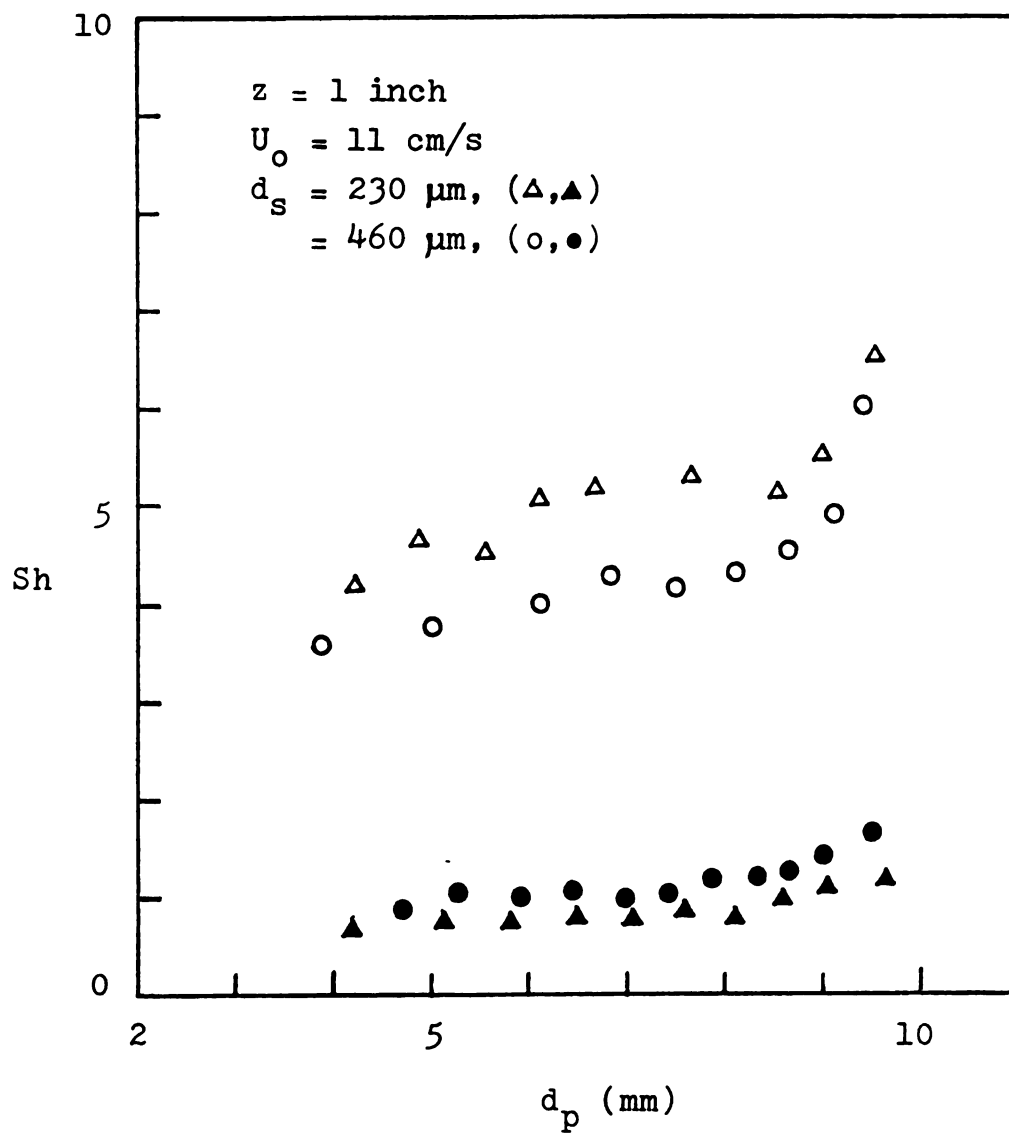


Figure 2.37 Effect of inert particle size on the Sherwood number ( $T_B = 1163 \text{ K}$ , dilute phase (open symbols), dense phase (closed symbols)).

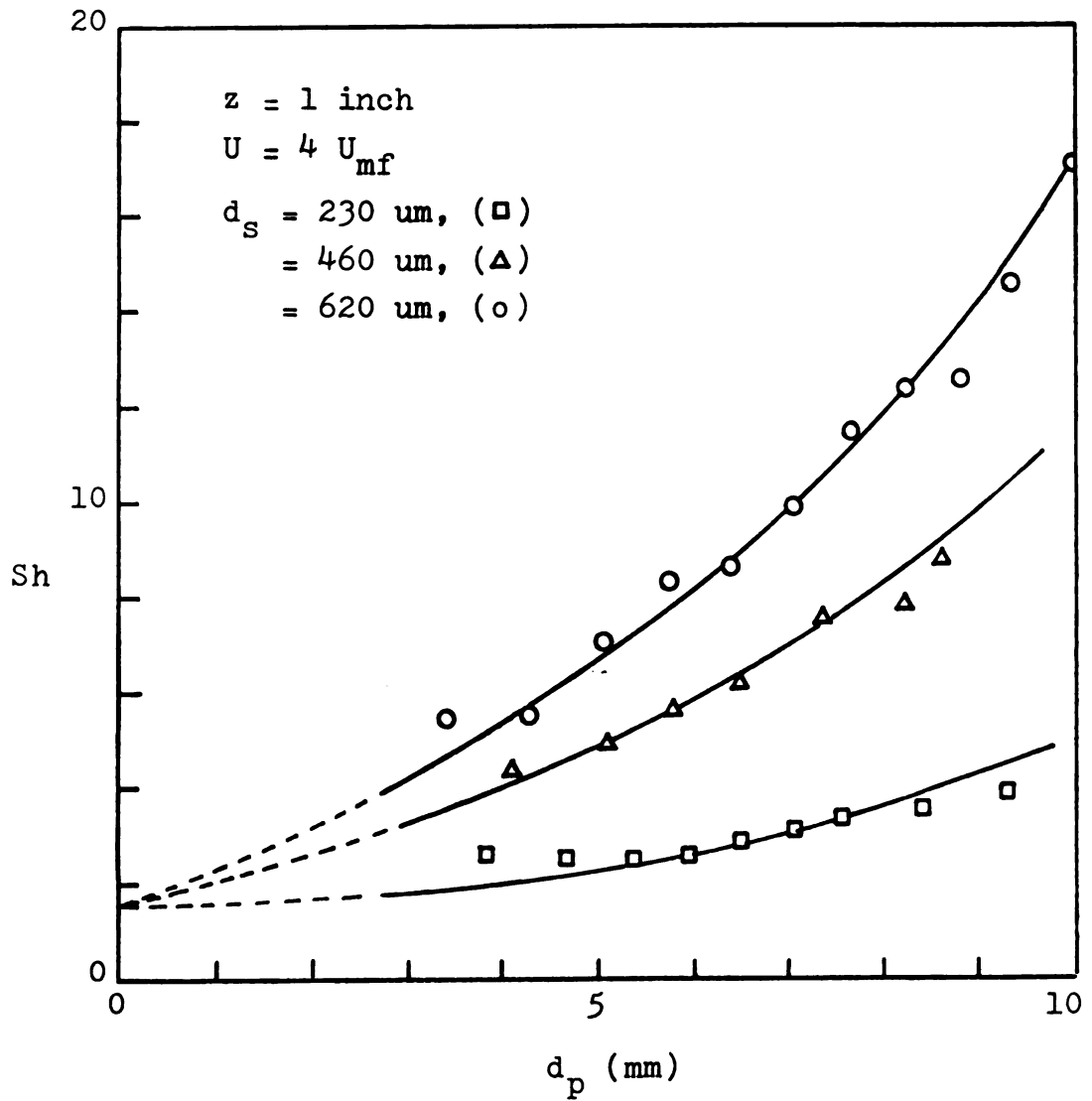


Figure 2.38 Effect of inert particle size on the Sherwood number in the dilute phase ( $T_B = 1163 \text{ K}$ ).

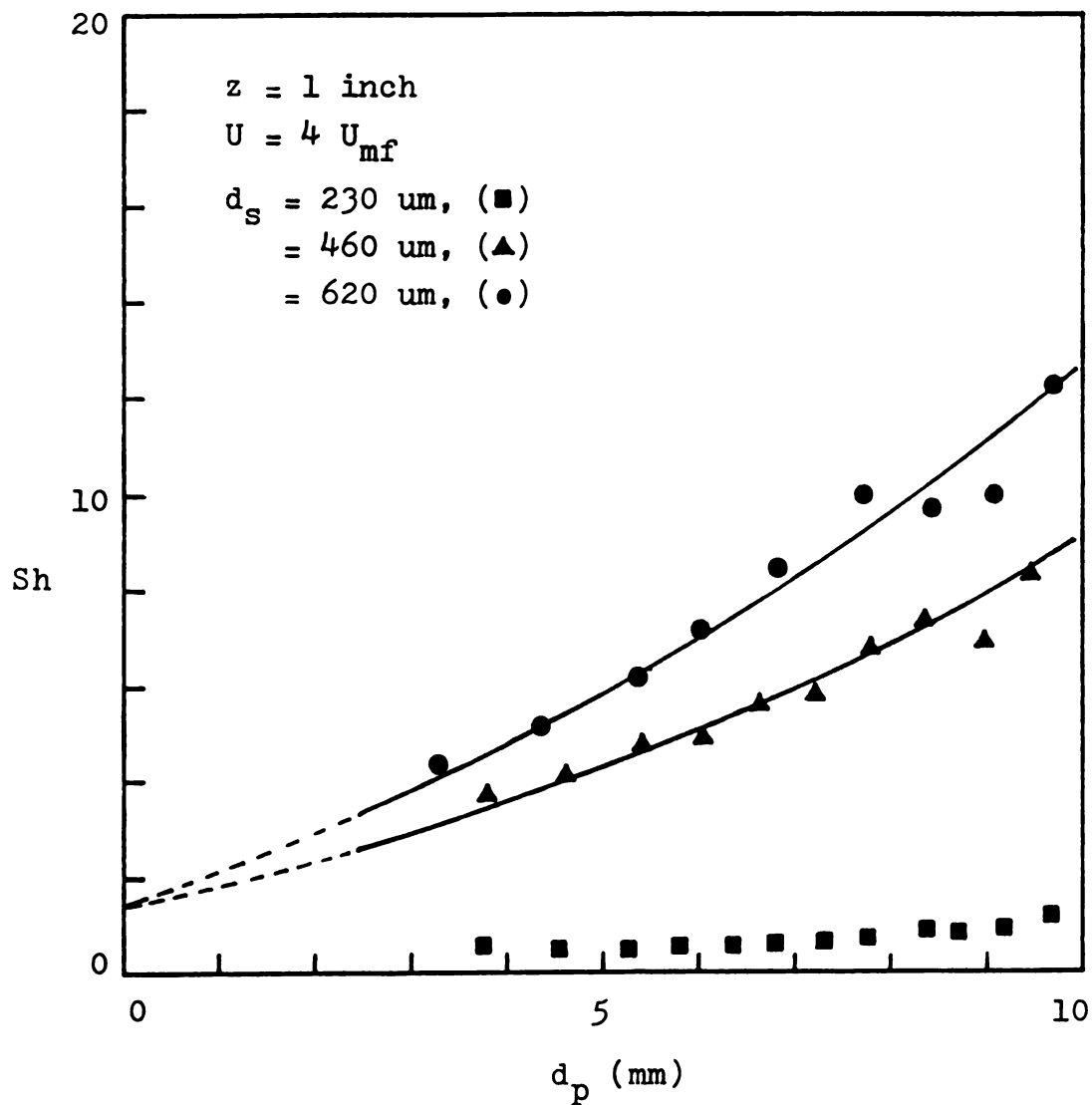


Figure 2.39 Effect of inert particle size on the Sherwood number in the dense phase ( $T_B = 1163 \text{ K}$ ).

#### 2-6-6. Vertical profiles of mass transfer resistance

The experimental results have shown in Section 2-6-3 the general trend that with increasing vertical distance, the mass transfer resistance increases in the dilute phase and decreases in the dense phase. Now, it will be useful to examine what the approximate profile of the resistance look like in each phase.

Figure 2.40 shows that for 620  $\mu\text{m}$  sand, the resistance at 1 inch above in the dilute phase is practically as high as that at 2 inch above, which seems to indicate that the resistance increases sharply within a relatively short distance downstream the orifice and remains constant thereafter. It is not possible to know with our experimental data precisely how short the distance is, but it must be at most one half of the grid region height. As the inert particle size is decreased to 230  $\mu\text{m}$ , the resistance in the latter half of the grid region is shown in Figure 2.41 to increase more significantly than 620  $\mu\text{m}$  sand. For all inert particle sizes, the resistance of the dilute phase must increase abruptly at the orifice due to sudden gas leakage and solids entrainment. Therefore, both mass transfer coefficient and voidage in the dilute phase are expected to decrease with upward concavity along the axial coordinate, and the concavity smooths out with decreasing inert particle size.

The mass transfer resistance of the dense phase appears to decrease more or less gradually over the entire grid region for all inert particle sizes and superficial gas velocities, as shown in Figure 2.42 for 620  $\mu\text{m}$  sand. The voidage of the dense phase can be regarded

as that in a packed bed,  $\epsilon_p$ , at the distributor and increases to  $\epsilon_b$  at the grid region height. Noting that the difference between  $\epsilon_b$  and  $\epsilon_p$  is on the order of 0.1, the profile of  $\epsilon$  is expected to be rather flat in the dense phase along the vertical coordinate. Hence, the gradual decrease in the resistance appears to be caused by the continuous influx of gas from the dilute phase throughout the jet height.

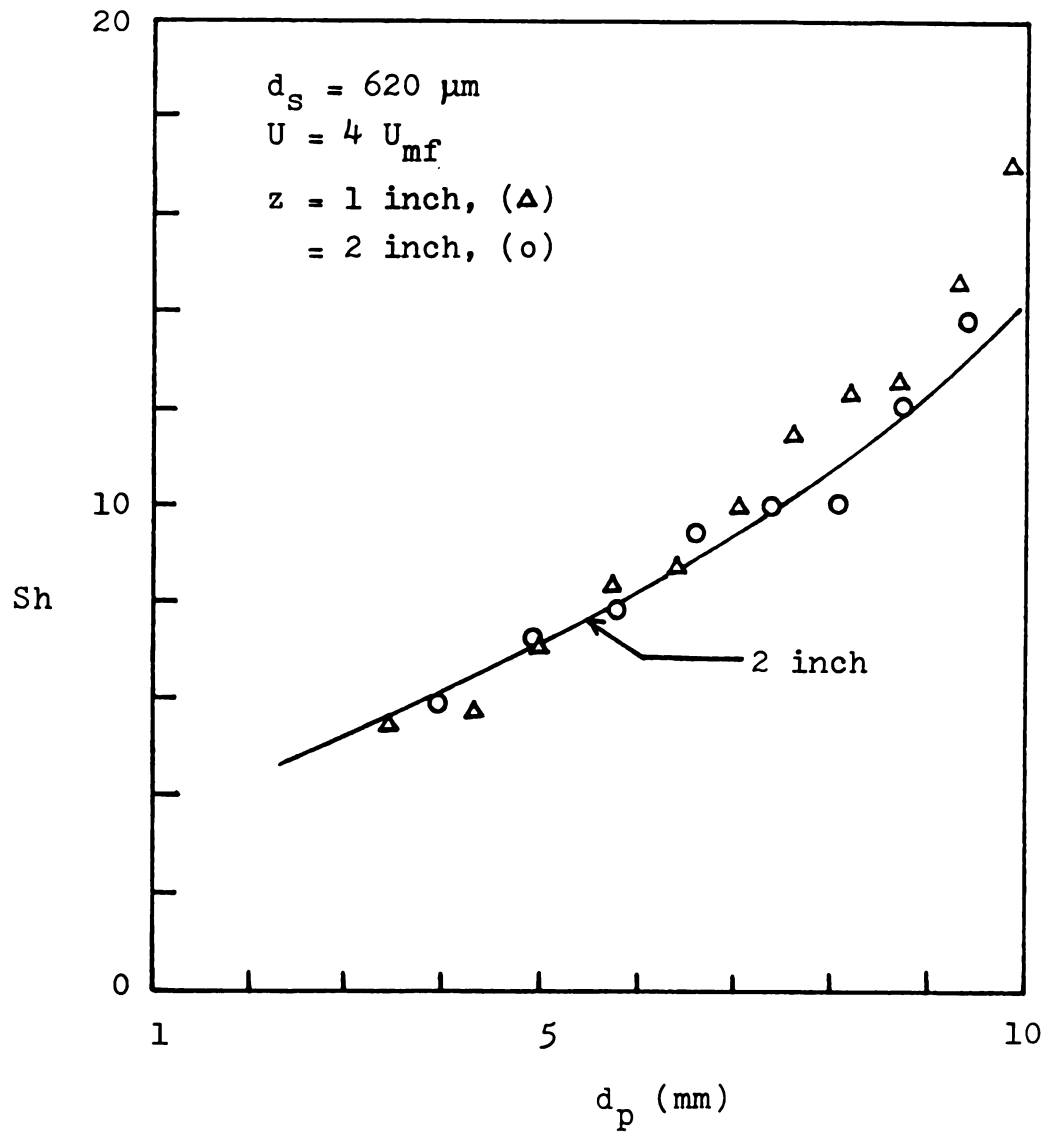


Figure 2.40 Variations in the Sherwood number along the vertical distance in the dilute phase ( $T_B = 1163 \text{ K}$ ).

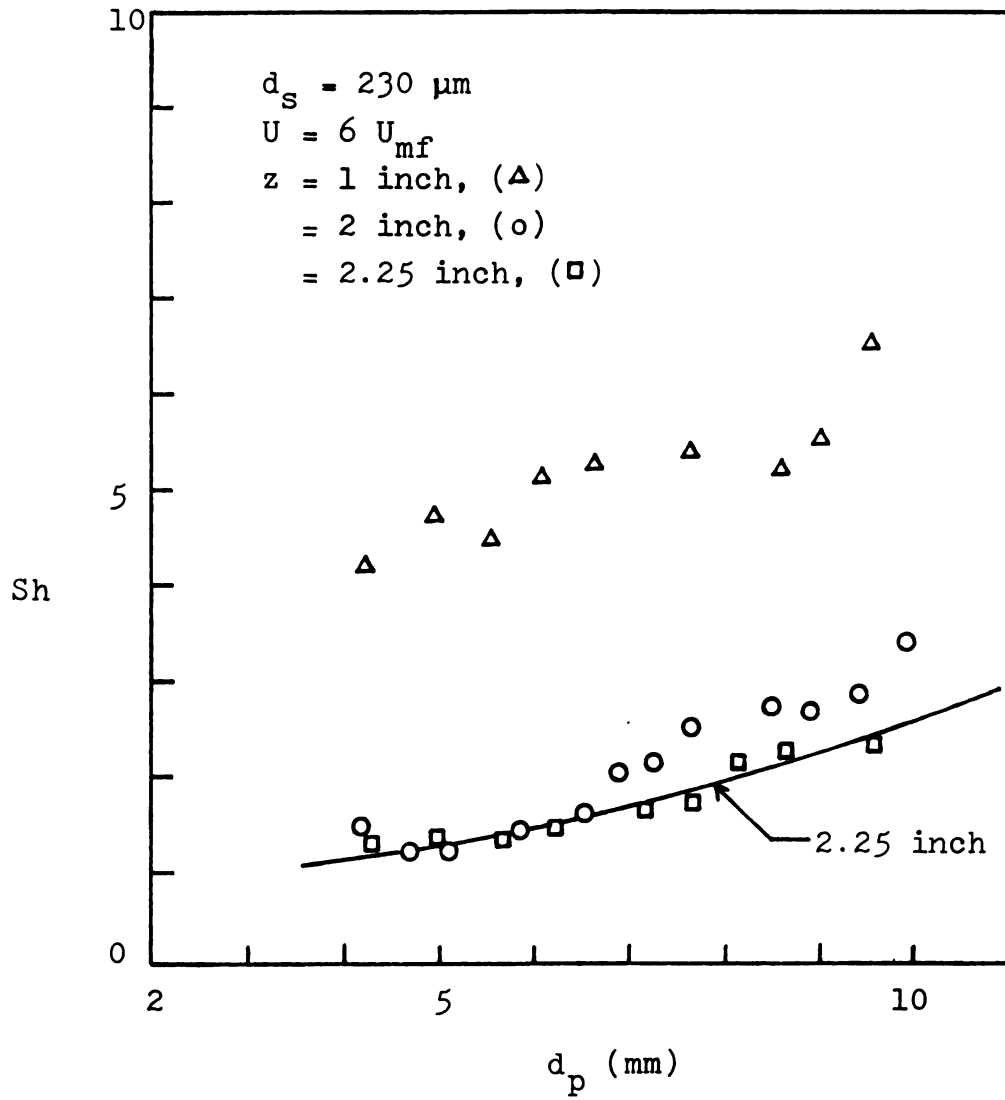


Figure 2.41 Variations in the Sherwood number along the vertical distance in the dilute phase ( $T_B = 1163 \text{ K}$ ).

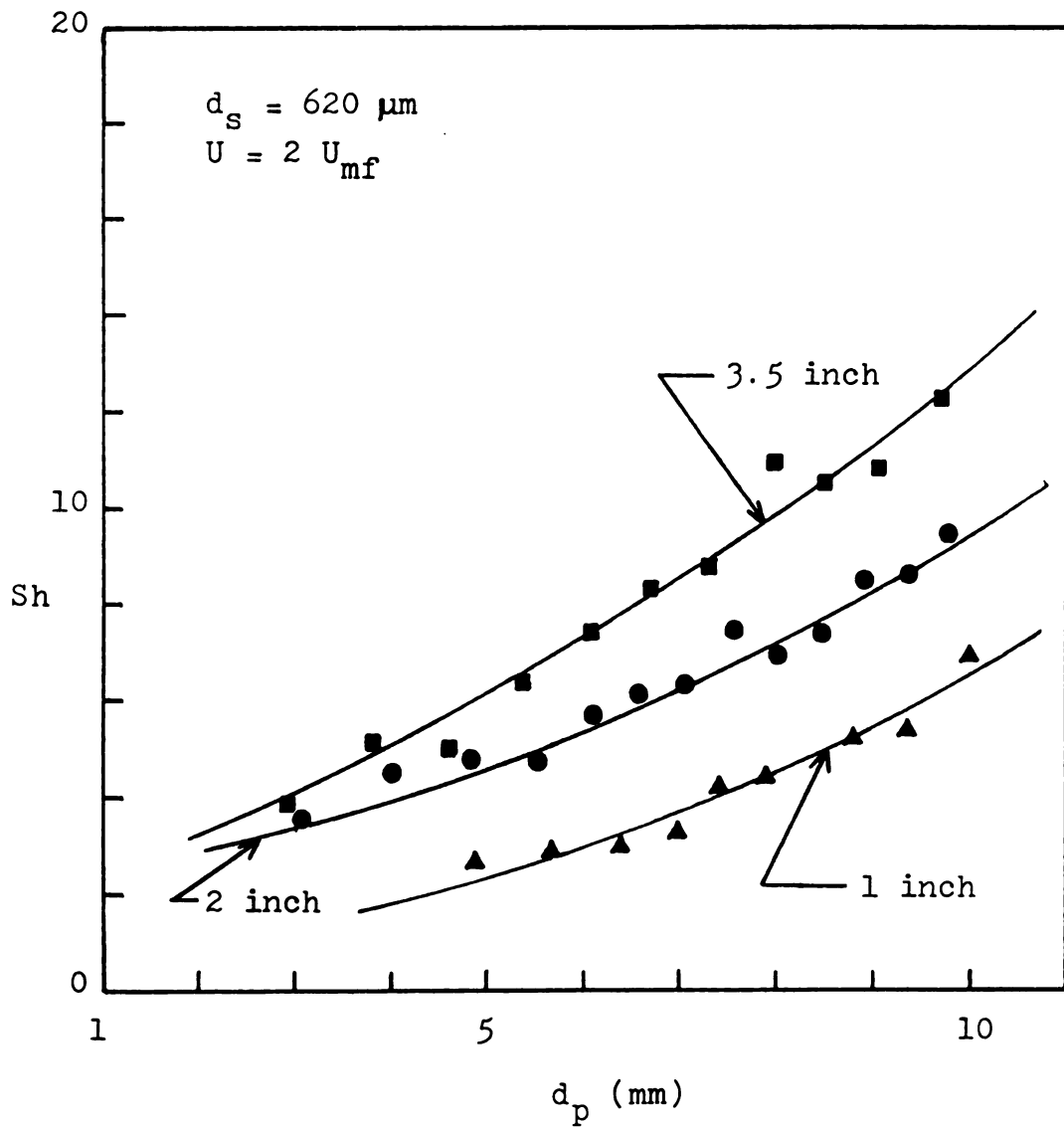


Figure 2.42 Variations in the Sherwood number along the vertical distance in the dense phase ( $T_B = 1163 \text{ K}$ ).

**CHAPTER 3**

**THEORETICAL ANALYSIS OF MASS TRANSFER CHARACTERISTICS**

**IN THE GRID REGION OF A FLUIDIZED BED COMBUSTOR**

### 3-1. Introduction

Although there are many correlations proposed in the literature concerning mass transfer in multiparticle-fluid systems, their applicability in fluidized bed combustion is severely limited due to a dilute situation and a significant difference in size between active and inert particles. Furthermore, unlike in the bubbling region, the experimental results in Chapter 2 have shown that the mass transfer resistance in each phase of the grid region varies in a rather complicated manner, depending on all operating variables considered such as inert particle size, superficial gas velocity and particle position. It appears that no effort has been made to study mass transfer in the grid region of a fluidized bed combustor, and we now attempt in this chapter to examine its theoretical aspects and to derive mass transfer correlations from the experimental data.

### 3-2. Review of Mass Transfer Studies in Multiparticle-Fluid Systems

#### 3-2-1. Background

Oxygen can be transported to a carbon particle burning in a dense bed of inert particles by both molecular diffusion and convection. In the single particle combustion of reactive carbons, the chemical rates are so fast that the concentration gradient for the diffusive and convective transport of oxygen can be assumed to exist only within the gaseous boundary layer surrounding each carbon particle in which CO oxidation takes place. For unreactive carbons such as electrode

graphite, it was shown in Figure 2.7 that the same assumption can be made regarding the concentration gradient of oxygen, if the apparent kinetic data based on the external surface area of the particle are used for the calculation of mass transfer coefficients.

The effective area available for diffusion is reduced due to the presence of inert particles and commonly taken as the local voidage times the total area free of inert particles. On the other hand, the characteristic velocity for convection in the boundary layer is difficult to calculate even in a laminar fluid.

In this Section, we review some of the important works on mass transfer in general multiparticle-fluid systems as well as fluidized beds by focusing our attention particularly on how the local voidage and the convective velocity were handled in each model.

### 3-2-2. Studies on the mechanism of mass transfer in a fluidized bed combustor

As mentioned earlier, despite the importance of the grid region on the overall bed performance, all the studies on mass transfer reported in the literature have been done exclusively in the bubbling region, and the following is a brief summary of such studies.

Avedesian and Davidson (5) first developed a comprehensive mathematical model for the burn-out time of a batch of char particles. They assumed in their model that neither  $\text{CO}_2$  nor  $\text{O}_2$  were present on the particle surface at a bed temperature of 1173 K and that the transport of  $\text{O}_2$  to the burning particle was primarily by molecular diffusion due

to small Reynolds number, based on  $U_{mf}$ , of order of 1. The Sherwood numbers were shown to be fairly constant at 1.42 during burn-off, which suggested that forced and natural convection effects were indeed negligible. They further proposed that the limiting value of 2 for the Sherwood number in the absence of inert particles must be multiplied by the particulate phase voidage.

Ross and Davidson (6) later extended the work by Avedesian and Davidson (5) by noting that the rate of reduction of  $CO_2$  by carbon is negligible at a bed temperature of 1173 K. They also included the effects of the chemical kinetics in the model, and concluded that the higher values of the Sherwood number on the order of 3.5 was indicative of convection.

Tamarin (58) calculated the average tangential stress created by a uniform flow around a sphere using the solution of the Prandtl boundary layer equations and equated the stress to the bed weight divided by the surface area of the sphere to obtain the following expression:

$$Sh = 0.248 (Sc Ar)^{1/3} (d_p/d_s)^{1/2} \quad (3.1)$$

where  $Ar$  is the Archimedes number, defined as  $d_s^3 \rho_f (\rho_s - \rho_f) g / \mu_f^2$ , and  $Sc$  is the Schmidt number, defined as  $\mu_f / \rho_f D_g$ . Eq. (3.1) states that the mass transfer coefficient does not depend on the gas velocity but is determined by the average tangential stress created at the surface of the particle suspended in a gas flow (58). The term,

$(d_p/d_s)^{1/2}$ , was inserted into Eq. (3.1) without any experimental verification simply to account for the difference in size between active and inert particles, and its inherent difficulties in predicting the experimental observations have been discussed by Prins et al. (9).

La Nauze and Jung (7) calculated the Sherwood numbers of petroleum coke particles using their known kinetic data, along with the assumptions of CO burning close to the particle and a constant particle temperature of 1303 K, 130 K higher than the bed temperature. The Sherwood numbers were shown to be well correlated by the Ranz and Marshall equation (33) modified a little to account for the presence of inert particles, viz:

$$\text{Sh} = 2 \epsilon_b + 0.69 (\text{Re}/\epsilon_b)^{1/2} \text{Sc}^{1/3} \quad (3.2)$$

where the Reynolds number is based on the superficial gas velocity,  $U$ .

Although Eq. (3.2) well represented the experimental results by La Nauze and Jung (7), the two-phase theory of fluidization (19) suggests that the characteristic velocity and voidage should be  $U_{mf}$  and  $\epsilon_{mf}$ , respectively, instead of  $U$  and  $\epsilon_b$ , since the particles burn mostly in the particulate phase. This point was later grasped by La Nauze et al. (8) in their unsteady state model. In addition to the oxygen transport from the gas flowing through the particulate phase, they assumed in their model that packets of particles formed around the periphery of a bubble transport fresh oxygen to the burning particles, while they are circulating within the bed. They solved the unsteady state diffusion

equation in the same manner as Higbie's formulation of the penetration theory, and suggested the following expression:

$$\text{Sh} = 2 \epsilon_{mf} + \left[ \frac{4 \epsilon_{mf} d_p (U_{mf}/\epsilon_{mf} + U_b)}{\pi D_g^2} \right]^{1/2}, \quad (3.2)$$

which is now of the form consistent with the two-phase theory.

In deriving Eq. (3.2), La Nauze et al. (8) represented the resistance by inert particles to oxygen transfer by using the effective diffusivity,  $D = \epsilon_{mf} D_g$ , in the diffusion equation. Carvalho and Coelho (59) later argued that instead of  $D$ , the diffusivity of oxygen in air,  $D_g$ , should be used, since it is the area open to diffusion which is only  $\epsilon_{mf}$  times the total area. Agreement between the corrected version of Eq. (3.2) and the experimental Sherwood numbers was shown to be not as good (59). It should be noted that Eq. (2.3) further requires the accurate estimation of the size, frequency and velocity of bubbles which are difficult to measure experimentally.

Using extensive mass transfer data of naphthalene spheres vaporizing in air-fluidized beds of glass beads, alumina and silica sand at 65°C, Prins et al. (9) proposed an empirical correlation, as shown in Eq. (2.12), which explicitly shows the effects of both active and inert particle sizes on the mass transfer coefficient. The validity of correlating experimental data with the modified Reynolds number,  $\text{Re}_{mf} = U_{mf} d_p \rho_f / u_f (1 - \epsilon_{mf})$ , was questioned by Nishimura and

Ishii (60). Where the voidage approaches unity, namely for a single sphere in an infinite medium, this modified Reynolds number becomes infinity and physically meaningless, and such a Reynolds number cannot be derived theoretically (60).

One interesting observation made by Prins et al. (9) was that samples fixed right above the distributor exhibited higher mass transfer coefficients by 20 -50 % than the rest of the bed even for this low temperature vaporization with no considerable heat of reaction. Even though they provided no explanation for these high rates, their results indeed suggest a quite different mechanism for mass transfer in the grid region.

### 3-2-3. Studies on the mechanism of mass transfer in other multiparticle-fluid systems.

When all particles are actively involved in the mass transfer process, the boundary conditions are not the same as in a diluted system, and studies on such diluted systems are rather rare. Here, we begin by reviewing two works which have been tested against the data in diluted systems.

Kunii and Suzuki (61) developed a channeling model in which void spaces in packed beds were assumed to be unevenly distributed so that the selective flowing of fluid or channeling occurred in the loose section in a bed of fine particles. They divided the bed into many blocks of particles which were separated from one another by the void channels, and further assumed that molecular diffusion took place in the direction perpendicular to flow in each channel. They proposed the

following expression for mass transfer under the flow condition of low Péclet number:

$$\text{Sh} = \frac{\psi_s}{6(1-\epsilon)\xi} \text{Pe}_p, \quad \text{for } \text{Pe}_p < 10 \quad (3.3)$$

where  $\psi_s$  is the particle shape factor,  $\xi$  is the ratio of average channeling length to particle diameter, and  $\text{Pe}_p$  is the Péclet number for mass transfer, defined as  $d_p U/D_g$ . The drawback of this approach is the accurate estimation of  $\xi$  which was incidently used as a fitting parameter in correlating experimental data. It is interesting to note that the data by Bar-Ilan and Resnick (62) in a diluted system was fitted well by Eq. (3.3) with  $\xi = 1$ , that is, no channeling of flow, which suggests that in diluted systems, the effect of flow channeling is negligible.

Prins et al. (9) measured additional mass transfer coefficients in the same bed as before but at  $U = 0.8 U_{mf}$ , and found that those packed bed data could also be represented reasonably well by Eq. (2.12), if the superficial gas velocities were used in  $j_D$  and  $Re$ , instead of  $U_{mf}$ . The important conclusion was that the rate of mass transfer in a fluidized bed is the same as in a fixed bed of similar particles, the same porosity and at the same gas velocity.

We now further review two other studies on all particles active systems, because of their distinctive approach to the problem of finding the local voidage and the characteristic velocity of

convection. The study of Nelson and Galloway (63) was initiated from the difficulties of explaining extremely low mass transfer rates in the low Reynolds number range with the theory for a single sphere in an infinite medium. They formulated the problem according to the method of the penetration theory using the concentric spheres free surface cell model of Pfeffer and Happel (64) and a finite radius boundary condition. They further introduced the boundary layer theory in their model to estimate the surface renewal frequency, and this resulted in the terms,  $Re^{1/2}$  and  $Sc^{1/3}$ , appearing in their final expression for the Sherwood number at infinite dilution. It should be noted that the Reynolds number was based on the bulk fluid velocity. The local voidage was calculated simply by letting the voidage of the sphere and its surroundings enclosed by the outer spherical shell match that of the system. The significance of their results was that the dependence of the Sherwood number on  $Re$  was linear at low enough flow rates, and the Sherwood number became zero, instead of two, when there was no flow.

For high Reynolds number situations, Nishimura and Ishii (65) applied the same free surface cell model (64) in their numerical calculation of the velocity profiles and the local voidage around a sphere in a swarm which were subsequently used in their later work (60) in solving the steady state diffusion equation. They further assumed that the Sherwood number has two components, molecular diffusion and convective, and suggested the following correlation from their theoretical results:

$$\text{Sh} = \frac{2}{(1-\epsilon)^{1/3}} + 0.60 \text{Re}^{1/2} \text{Sc}^{1/3} \epsilon^{-1/2} \quad (3.4)$$

where the Reynolds number is based on the relative velocity between a solid and fluid,  $u_R$ . It is interesting to note that Eq. (3.4) reduces to the Ranz and Marshall equation (33) when  $\epsilon = 1$ .

Both of these studies clearly showed some promising features in the direction of improving the model predictions in multiparticle-fluid systems. However, it is unfortunate that they are applicable only to the systems in which all particles are active.

### 3-3. Development of Mass Transfer Correlations in the Grid Region

#### 3-3-1. Formulation of the problem of mass transfer in a dilute system

Regardless of the concentration of active particles in a multiparticle-fluid system, most mass transfer correlations were shown in Section 3-2 to have been developed around the steady state forced convection equation by Ranz and Marshall (33):

$$\text{Sh} = 2 + \alpha \text{Re}^{1/2} \text{Sc}^{1/3}, \quad (3.5)$$

where  $\alpha$  is usually taken as 0.6. Eq. (3.5) is applicable to single spheres in a fluid for the Reynolds number, based on the bulk fluid velocity, usually greater than 5. Any attempt to modify Eq. (3.5) for the application in multiparticle-fluid systems was exclusively to

account for the effects of other particles on the local voidage and the characteristic velocity around one particle of interest.

In all particles active systems, these attempts oftentimes have been found to be unsuccessful especially at low Reynolds numbers, since the infinite radius boundary condition of Eq. (3.5) cannot be met. On the other hand, in diluted systems, this infinite radius boundary condition can be tolerated, since the concentration of active particles is so low that each active particle is virtually surrounded by many inert particles at all times. Figures 2.38 and 2.39 indeed show that the Sherwood numbers approach a value a little less than two as the particle diameter approaches zero except those for 230  $\mu\text{m}$  sand, which suggests that the presence of inert particles is merely to decrease the area available for molecular diffusion.

Furthermore, the bulk fluid velocity in the convective component of Eq. (3.5) should also be replaced by a characteristic velocity in a multiparticle-fluid system, and the most logical choice would be to use the interstitial velocity among inert particles. However, the distribution of local voidage near the active particle has been shown by Basu (66) to be similar to a damped oscillatory function even for uniformly sized particle systems; the voidage is maximum at the active particle surface, and the fluctuating local voidage dies down to the mean voidage of the system away from the active particle. Further complications are expected to arise in the variation of local voidage, if the active and inert particles are different sized and the active particle size actually decreases during the transfer process. A full mathematical treatment of this problem is extremely complicated and far

beyond the scope of this work. Hence, if we are to contend with the interstitial velocity,  $u$ , based on the local mean voidage, the Sherwood number dependence should be different from  $Re^{1/2}$ .

The exponent  $1/3$  of the Schmidt number in Eq. (3.5) has been shown in recent studies (67) to be inadequate for  $Re > 1$ . The value of  $1/3$  was obtained from the case of developing boundary layer which probably exists in the front half of the sphere near the stagnation point, and would not apply to the wake region where its value may increase to  $1/2$  for unsteady state flow. However, in a typical fluidized bed combustor, the Schmidt number is on the order of unity, and the Sherwood number dependence is not as significant as on the Reynolds number.

To sum up, we now propose the following expression for the Sherwood number in the grid region:

$$Sh = 2 \epsilon + a Re^b Sc^{1/3} \quad , \quad (3.6)$$

where  $a$  and  $b$  are constants to be evaluated from the experimental data, and the Reynolds number is defined as  $\rho_f u d / \mu_f$ . In order to evaluate the constants  $a$  and  $b$ , it is necessary to calculate  $\epsilon$  and  $u$  as a function of the axial distance from the distributor in each phase of the grid region.

### 3-3-2. Analogy between the grid region and a spouted bed

A spouted bed is an efficient device of contacting coarse particles with gas, and many of its hydrodynamic features are quite analogous to those of the grid region. Both a spouted bed and the section WXYZ in Figure 2.2 consist of a dilute phase of gas jet and entrained particles and a dense phase of under-fluidized particles surrounding the jet. As shown in Figure 3.1, there is a continuous flow of solids from the dense phase into the jet throughout the jet height, and gas leaks in the opposite direction. The main difference is that the jet breaks up into small bubbles in the grid region for  $U > U_{mf}$ , whereas it always penetrates to the bed surface in a spouted bed. However, when a spouted bed is at the minimum spouting condition, both the particles entrained in the dilute phase and those in the dense phase are by definition just fluidized at the bed surface. As noted in Section 2-6-2, the same degree of fluidization is also attained at the grid region height at minimum fluidization,  $H_{mf}$ , without any bubble formation.

Therefore, the general behavior of gas and solids flows of a spouted bed at minimum spouting can be assumed to be identical to that of the grid region at minimum fluidization, and consequently some of the useful theories of spouted beds can be readily applied to the grid region study.

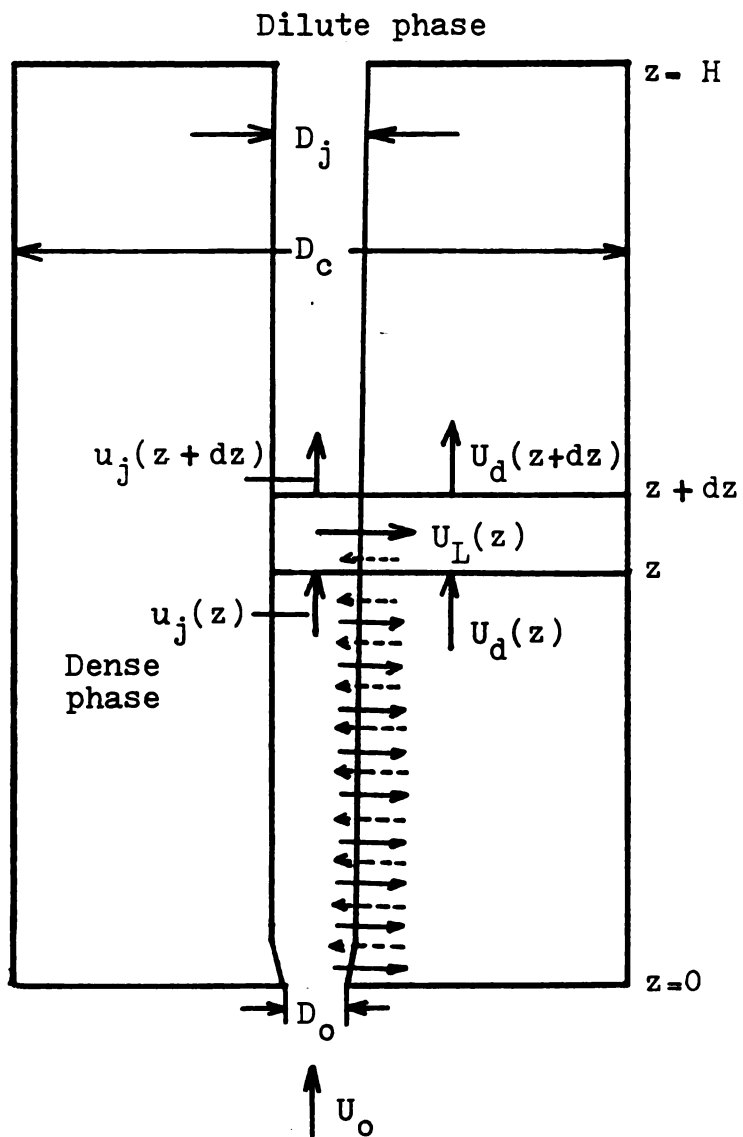


Figure 3.1 Spouted bed model as applied to the grid region (  $\leftarrow$ ---, solids flow;  $\rightarrow$  , gas flow ).

### 3-3-3. Axial voidage distributions in the grid region

Since the dense phase voidage remains relatively constant in the axial direction at or even above minimum fluidization, we now concentrate mainly on the axial voidage distribution in the dilute phase. Currently, there are two different methods of calculating the dilute phase voidage,  $\epsilon_j$ , in a spouted bed: the variational method by Morgan et al. (68) and the numerical method of solving the mass and momentum balance equations, as done by Lefroy and Davidson (56) using an additional empirical equation describing the axial pressure distribution just outside the spout. Due to its simplicity and applicability at the minimum spouting condition, we will directly employ the variational method to calculate  $\epsilon_j$  at minimum spouting and later use a similarity relationship to find the values of  $\epsilon_j$  above minimum fluidization.

Assuming that the jet diameter,  $D_j$ , is constant throughout its height, the momentum equations for gas and solids in the dilute phase are given as (56):

Gas:

$$\rho_f \frac{d}{dz} (\epsilon_j u_j^2) = -\epsilon_j \frac{dP_j}{dz} - \delta (u_j - v_j)^2 \quad (3.7)$$

Solids:

$$\rho_p \frac{d}{dz} \left[ (1 - \epsilon_j) v_j^2 \right] = - (1 - \epsilon_j) \frac{dP_j}{dz} + \delta (u_j - v_j)^2$$

$$- (\rho_p - \rho_f) g (1 - \epsilon_j) \quad (3.8)$$

where  $u_j$  and  $v_j$  are the radially averaged velocity of gas and solids, respectively,  $\epsilon_j$  and  $P_j$  are also the radially averaged voidage and pressure, respectively, and  $\delta$  is a gas-solids interphase drag coefficient.

Combining Eqs. (3.7) and (3.8), the average momentum equation of the mixture becomes

$$\rho_f \frac{d}{dz} (\epsilon_j u_j^2) + \rho_p \frac{d}{dz} \left[ (1 - \epsilon_j) v_j^2 \right] \\ - - \frac{dP_j}{dz} - (\rho_p - \rho_f) g (1 - \epsilon_j) \quad (3.9)$$

Integrating Eq. (3.9) over the jet height at minimum spouting,  $H_{ms}$ , commonly called the maximum spoutable bed depth, we obtain

$$\rho_f \epsilon_j(H_{ms}) u_j^2(H_{ms}) - \rho_f \epsilon_j(0) u_j^2(0) + \rho_p \left[ 1 - \epsilon_j(H_{ms}) \right] v_j^2(H_{ms}) \\ - \rho_p \left[ 1 - \epsilon_j(0) \right] v_j^2(0) - \Delta P_{ms} - (\rho_p - \rho_f) g \int_0^{H_{ms}} (1 - \epsilon_j)_{ms} dz \quad (3.10)$$

where  $\Delta P_{ms}$  is the bed pressure drop at minimum spouting.

At minimum spouting,  $v_j(H_{ms}) = 0$ ,  $\epsilon_j(H_{ms}) = \epsilon_{mf}$  and  $u_j(H_{ms}) = U_{mf} / \epsilon_{mf}$ . Furthermore, at  $z = 0$ ,  $\epsilon_j(0) = 0$  and  $v_j(0) = 0$ . Also noting that  $u_j(0) = (D_o/D_{j,ms})^2 U_{o,mf}$  from continuity, Eq. (3.10) can be rewritten as

$$\rho_f U_{mf}^2 - \rho_f (D_o/D_{j,ms})^4 U_{o,mf}^2 - \Delta P_{ms} - (\rho_p - \rho_f) g \int_0^{H_{ms}} (1 - \epsilon_j)_{ms} dz \quad (3.11)$$

Dividing by the pressure drop across a fluidized bed of the same depth,  $\Delta P_{mf} = (1 - \epsilon_{mf}) g (\rho_p - \rho_f) H_{ms}$ , Eq. (3.11) further reduces to

$$\int_0^1 \frac{[1 - \epsilon_j(\zeta)]_{ms}}{1 - \epsilon_{mf}} d\zeta - I_0 - \frac{\Delta P_{ms}}{\Delta P_{mf}} + \frac{\rho_f \left[ (D_o/D_{j,ms})^4 U_{o,mf}^2 - U_{mf}^2 / \epsilon_{mf} \right]}{(1 - \epsilon_{mf}) (\rho_p - \rho_f) g H_{ms}} \quad (3.12)$$

where  $\zeta$  is the normalized axial coordinate, defined as  $z/H_{ms}$ , and the

boundary conditions are  $\epsilon(0) = 1$  and  $\epsilon(1) = \epsilon_{mf}$ .

The solution to this variational problem is given as (68)

$$\frac{1 - \epsilon_j(\zeta)]_{ms}}{1 - \epsilon_{mf}} = I_2 - \frac{1}{\lambda} \left[ 1 - (\lambda\zeta + I_1)^2 \right]^{1/2} \quad (3.13)$$

where  $\lambda = (1 - I_1^2)^{1/2} - I_1$  (3.14)

$$I_2 = (1 - I_1^2)^{1/2} \left[ (1 - I_1^2)^{1/2} - I_1 \right] \quad (3.15)$$

$$I_0 = I_2 - (1/2\lambda^2) \left[ (1 - I_1^2)^{1/2} (|I_1| - I_1) + \sin^{-1} \left[ (1 - I_1^2)^{1/2} \right] - \sin^{-1} I_1 \right] \quad (3.16)$$

$I_1$ ,  $I_2$  and  $\lambda$  are obtained by solving Eqs. (3.14) - (3.16) simultaneously.

In order to find the value of  $I_0$  for each sand particle size considered this study, the jet diameter at minimum spouting,  $D_{j,ms}$ , is estimated from the correlation by Lefroy and Davidson (56):

$$D_j = 1.06 D_c^{2/3} d_s^{1/3} \quad (3.17)$$

where  $D_c$  is the equivalent diameter of a spouted bed. Equation (3.7) indicates that the jet diameter is independent of the gas flow rate, which is a rather surprising result.

Furthermore, the force balance analysis of Mamuro and Hattori (69), based on the assumption that Darcy's law governs the gas flow in the dense phase, suggests the ratio of  $\Delta P_{ms}/\Delta P_{mf}$  to be 0.75 at minimum spouting regardless of particle size and density. Epstein et al. (70) later showed that the value of the pressure drop ratio was somewhat greater than what was generally observed experimentally and attributed this discrepancy mainly to the deficiency in the Mamuro-Hattori model by neglecting the shear stresses at the jet boundary and bed wall that partially support the particles. However, at least no solid wall is present around the section WXYZ in Figure 2.2, and thus we have exclusively assumed that  $\Delta P_{ms}/\Delta P_{mf} = 0.75$  at minimum spouting.

Table 3.1 further shows that the dimensionless pressure drop term is so dominating in Eq. (3.12) that the values of  $I_0$  remain essentially constant at 0.75 for all sand particle sizes. The significance of this result is that under the operating conditions considered in this study, the axial voidage profile in the dilute phase is the same at minimum spouting regardless of the particle size, when plotted against the dimensionless axial distance,  $z/H_{ms}$ , as shown in Figure 3.2. It should be noted here that due to many hydrodynamic similarities discussed in Section 3-3-2,  $H_{ms}$  can be assumed to be the same as  $H_{mf}$  and Figure 3.2 should also represent the axial voidage profile in the dilute phase of

the grid region at  $U = U_{mf}$ . As predicted in Section 2-6-6, the dilute phase voidage is indeed shown to decrease monotonically with upward concavity.

Table 3.1 Values of the parameters used in the calculation of  $I_0$

$$\rho_p = 2,700 \text{ kg/m}^3, \rho_f = 0.3892 \text{ kg/m}^3, D_o = 6.35 \text{ mm}$$

$d_s$ ( $\mu\text{m}$ )	$U_{o,mf}$ (m/s)	$D_j$ (cm)	$H_{ms}^*$ (cm)	$\Delta P_{ms} / \Delta P_{mf}$	$I_0$
230	1.55	0.98	8.8	0.75	0.7501
460	6.25	1.23	9.0	0.75	0.7508
620	11.28	1.36	11.2	0.75	0.7513

\* Values of  $H_{mf}$  from Table 2.5.

Above minimum spouting or when  $H < H_{ms}$ , the variational method is no longer applicable, since the term  $v_j(H)$  does not vanish. Hence, the dilute phase voidage above minimum fluidization,  $\epsilon_j(z)$ , is calculated using the following similarity relationship (68):

$$\frac{1 - \epsilon_j(z)}{1 - \epsilon_j(H)} = \frac{1 - [\epsilon_j(z)]_{mf}}{1 - \epsilon_{mf}} \quad (3.18)$$

where  $\epsilon_j(H)$  is equal to the mean bed voidage,  $\epsilon_b$ , and the values of

$[\epsilon_j(z)]_{mf}$  are obtained from Figure 3.2.

Upon rearranging, Eq. (3.18) becomes

$$\epsilon_j(z) = 1 - \left[ 1 - \left[ \epsilon_j(z) \right]_{mf} \right] \left( \frac{1 - \epsilon_b}{1 - \epsilon_{mf}} \right) \quad (3.19)$$

where  $\epsilon_b$  is the mean bed voidage.

Since the bed surface is always violently fluctuating in gas fluidized beds, it is extremely difficult to measure the height of an expanded bed accurately, and there is no reliable correlation available for its estimation. Therefore, we used the following equation suggested for a suspension system to calculate  $\epsilon_b$  for different particle size and gas velocity:

$$\frac{U}{u_t} = \epsilon_b^m, \quad (3.20)$$

where  $u_t$  is the terminal velocity of particles, and the exponent  $m$  is estimated from (72):

$$m = \frac{\log (Re_{mf}/Re_t)}{\log \epsilon_{mf}}, \quad (3.21)$$

where  $\epsilon_{mf}$  is assumed to be 0.4 for all  $d_s$ , and the values of  $\epsilon_b$  thus calculated are tabulated in Table 3.2. It is further shown in Figure

3.2 that the dilute phase voidage calculated from Eq. (3.19) increases with increasing  $U$  for all  $z$ , as expected.

Table 3.2 Mean bed voidage calculated from Eq. (3.20) and (3.21)

$d_s$ ( $\mu\text{m}$ )	$u_c$ (m/s)	$m$	$U/U_{mf}$	$\epsilon_b$
230	3.97	5.13	3.0	.434
			4.0	.459
			6.0	.497
460	4.08	4.38	1.5	.438
			2.0	.468
			4.0	.540
620	5.49	4.06	2.0	.474
			2.2	.485
			3.0	.524
			4.0	.562

It was stated earlier in this section that the axial variation of the dense phase voidage,  $\epsilon_d$ , is negligible at minimum fluidization, since,  $\epsilon_p \approx \epsilon_{mf}$ . However, according to the definition of the grid region height, the voidage should increase from  $\epsilon_{mf}$  to  $\epsilon_b$  near  $z = H$ , for  $U > U_{mf}$ . It was further shown by Fakhimi et al. (57) that the dense phase becomes completely fluidized at  $z = h_e$ . For all  $U$ , the difference of  $(\epsilon_b - \epsilon_{mf})$  is relatively small, and the dense phase

voidage can be assumed to remain constant at  $\epsilon_{mf}$  up to the dead zone height,  $z = h_d$ , and increase linearly thereafter to  $\epsilon_b$  at  $z = H$ :

$$\epsilon_d(z) = \begin{cases} \epsilon_{mf} & , & \text{for } 0 \leq z \leq h_d \\ \frac{1}{H - h_e} \cdot \left[ (\epsilon_b - \epsilon_{mf}) z + \epsilon_{mf} H - \epsilon_b h_e \right] & , & \text{for } h_d \leq z \leq H \end{cases} \quad (3.22)$$

where  $h_d$  is the dead zone height and will be discussed in detail in

Section 3-4.

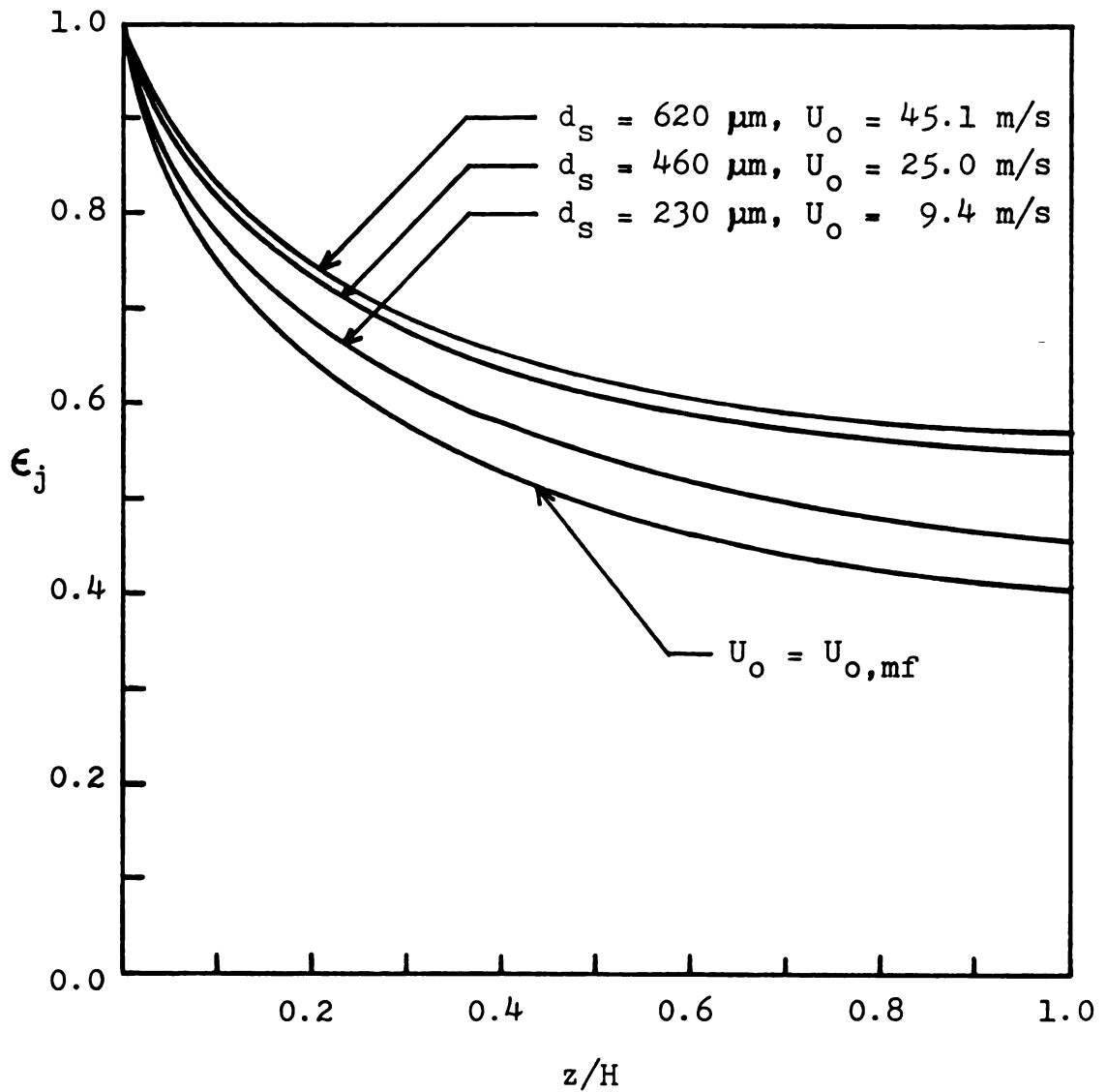


Figure 3.2 Axial voidage distribution in the dilute phase calculated from Eqs. (3.13) and (3.19).

3-3-4. Axial velocity distribution in the grid region

At minimum spouting, the superficial gas velocity in the dense phase of a spouted bed is given as (69)

$$U_d(z) = U_{mf} \left[ 1 - (1 - z/H_{ms})^3 \right], \quad (3.23)$$

which was derived from the following differential force balance equation and boundary conditions:

$$d\sigma_d + dP_d + (\rho_p - \rho_f) g (1 - \epsilon_d) dz = 0 \quad (3.24)$$

$$\begin{aligned} \text{B. C. 1.} \quad & U_d(0) = 0 \\ & 2. \quad U_d(H_{ms}) = U_{mf} \\ & 3. \quad -dP_d / dz \Big|_{H_{ms}} = (\rho_p - \rho_f)(1 - \epsilon_d) g \end{aligned}$$

where  $\sigma_d$  is the average stress borne by the solids. Epstein and Levine (71) showed that Eq. (3.23) still satisfies well even the case of non-Darcy flow in the dense phase. Furthermore, Yokogawa et al. (73) reworked the Mamuro-Hattori analysis by including in Eq. (3.24) the shear stresses acting on both sides of the dense phase, and their complicated final expression for  $U_d$  contained an adjustable parameter that had to be determined from experimental  $U_d(H)$ . Hence, we have

assumed that the axial velocity distribution in the dense phase of the grid region at  $U = U_{mf}$  is well represented by Eq. (3.23) with  $H_{ms}$  being experimental  $H_{mf}$ .

The extension of Eq. (3.23) for  $H < H_{ms}$  was successfully done by Grbarčić (74), and we exclusively use the following expression for the axial velocity distribution in the dense phase above minimum fluidization:

$$U_d(z) = U_d(H) \left[ \frac{1 - (1 - z/H_{mf})^3}{1 - (1 - H/H_{mf})^3} \right], \quad (3.25)$$

where  $U_d(H)$  is equal to the superficial gas velocity of fluidization,  $U$ , from the definition of the grid region height,  $H$ . It should be noted that all  $U_d$ 's are also radially averaged ones, and the corresponding interstitial velocity,  $u_d(z)$ , is simply  $U_d(z)/\epsilon_d(z)$ .

The interstitial axial velocity in the dilute phase,  $u_j(z)$ , is calculated from differential mass balance equations (56) between  $z = z$  and  $z = z + dz$ , as shown in Figure 3.1:

Dilute phase:

$$-\frac{\pi}{4} D_j^2 \frac{d(\epsilon_j u_j)}{dz} = U_L \pi D_j \quad (3.26)$$

Dense phase:

$$\frac{\pi}{4} (D_c^2 - D_j^2) dU_d = U_L \pi D_j dz \quad (3.27)$$

where  $U_L(z)$  is the superficial velocity of gas leakage into the dense phase, and solids entrainment as well as gas leakage is assumed to occur only in the radial direction at the jet boundary, as shown in Figure 3.1.

Combining Eqs. (3.26) and (3.27) and integrating from  $z = 0$  to  $z = z$ , we obtain

$$\epsilon_j(z) u_j(z) - \epsilon_j(0) u_j(0) = \left[ 1 - \left( \frac{D_c}{D_j} \right)^2 \right] \left[ U_d(z) - U_d(0) \right] \quad (3.28)$$

Substituting Eq. (3.25) into Eq. (3.28) and noting that at  $z=0$ ,  $\epsilon_j = U_d = 0$  and  $u_j(0) = (D_o/D_j)^2 U_o$ , Eq. (3.28) further reduces to

$$u_j(z) = \frac{1}{\epsilon_j(z)} \left[ U_o \left( \frac{D_o}{D_j} \right)^2 + U \left( 1 - \left( \frac{D_c}{D_j} \right)^2 \right) \left[ \frac{1 - (1 - z/H_{mf})^3}{1 - (1 - H/H_{mf})^3} \right] \right] \quad (3.29)$$

which is valid for all  $U \geq U_{mf}$ . At the grid region height,  $z = H$ , Eq. (3.29) becomes

$$\epsilon_j(H) u_j(H) = U_o \left( \frac{D_o}{D_j} \right)^2 + U \left[ 1 - \left( \frac{D_c}{D_j} \right)^2 \right] \quad (3.30)$$

Furthermore, from continuity, we have

$$U_o D_o^2 = U D_c^2 \quad (3.31)$$

Hence, Eq. (3.30) reduces to  $\epsilon_j(H) u_j(H) = U = U_d(H)$ , as it should.

The axial gas velocities calculated from Eq. (3.29) are shown in Fig. 3.3 to decrease monotonically with upward concavity as the axial distance increases.

It is further to be noted that the equivalent diameter of a spouted bed calculated from Eq. (3.31) is 5.86 cm, which is about 5 % greater than the actual pitch size of 5.56 cm. This discrepancy arises from the fact that the gas flow through the interstitial space among the imaginary columns in contact with one another is unaccounted for, when the diameter of each column is assumed to be the pitch size itself.

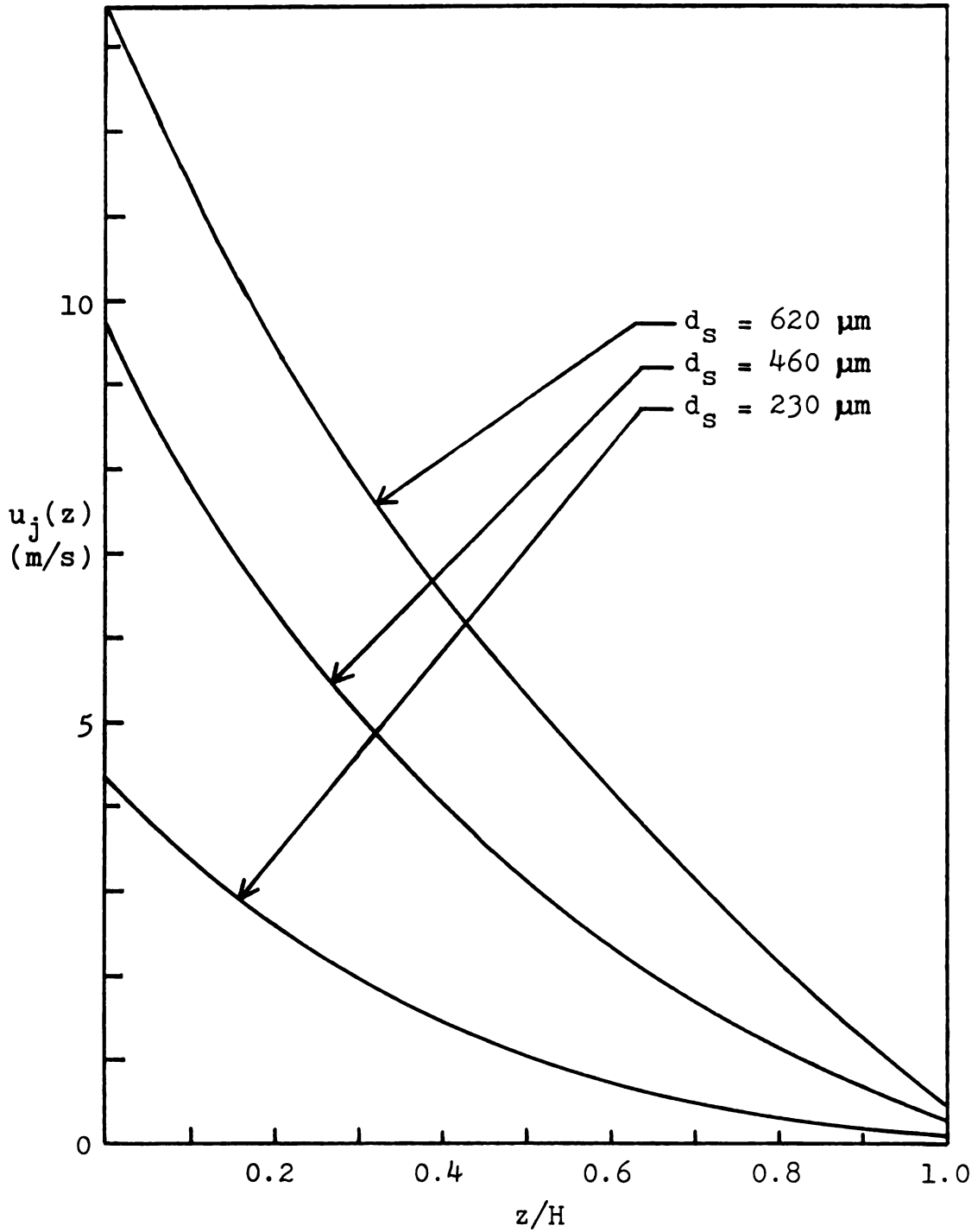


Figure 3.3 Axial velocity distribution in the dilute phase at  $U = 4 U_{mf}$ .

### 3-3-5. Development of mass transfer correlations

The general procedures of estimating the constants a and b in Eq. (3.6) from the experimental data can be summarized as follows:

#### Dilute phase:

- (1) Calculate  $I_0$  in Eq. (3.12) at minimum fluidization.
- (2) Solve for  $[\epsilon_j(z)]_{mf}$  from Eqs. (3.13) - (3.16).
- (3) Find  $\epsilon_j(z)$  for  $U > U_{mf}$  from Eq. (3.19).
- (4) Find  $u_j(z)$  for  $U \geq U_{mf}$  from Eq. (3.29).
- (5) Calculate  $\epsilon_j(z)$  and  $u_j(z)$  at each z, and  
 plot  $\log \left[ (\text{Sh}_{\text{exp}} - 2 \epsilon_j) / \text{Sc}^{1/3} \right]$  against  $\log \text{Re}_j$ .
- (6) Estimate the slope and y-intercept.

#### Dense phase:

- (1) For  $U > U_{mf}$ , find  $\epsilon_d(z)$  from Eq. (3.22).  
 For  $U = U_{mf}$ ,  $\epsilon_d(z) = \epsilon_{mf}$  for all z.
- (2) For  $U > U_{mf}$ , find  $u_d(z) = U_d(z) / \epsilon_d(z)$  from Eq. (3.25).  
 For  $U = U_{mf}$ , find  $u_d(z) = U_d(z) / \epsilon_d(z)$  from Eq. (3.23).
- (3) Calculate  $\epsilon_d(z)$  and  $u_d(z)$  at each z, and  
 plot  $\log \left[ (\text{Sh}_{\text{exp}} - 2 \epsilon_d) / \text{Sc}^{1/3} \right]$  against  $\log \text{Re}_d$ .
- (4) Estimate the slope and y-intercept.

As shown in Figures 3.4 and 3.5, the lower zone of the dilute phase from  $z = 0$  to  $z = h_e$  exhibited mass transfer characteristics quite different from the upper zone from  $z = h_e$  to  $z = H$ . This is certainly expected, because the mode of gas flow changes from a jet to bubbles at  $z = h_e$ , as discussed in Section 2-6-2. The proposed correlations for mass transfer in the dilute phase are

Lower zone ( $0 \leq z < h_e$ ) :

$$Sh_j(z) = 2\epsilon_j(z) + 0.006 Re_j^{1.35}(z) Sc^{1/3} \quad (3.32)$$

$$\text{for } 70 < Re_j < 500 \text{ and } 3 < Re_{s,j} < 30$$

Upper zone ( $h_e \leq z \leq H$ ) :

$$Sh_j(z) = 2\epsilon_j(z) + 0.115 Re_j^{1.15}(z) Sc^{1/3} \quad (3.33)$$

$$\text{for } 10 < Re_j \leq 70 \text{ and } 0.3 < Re_{s,j} < 5$$

where  $Re_j(z) = \rho_f u_j(z) d_p / \mu_f$  and  $Re_{s,j}(z) = \rho_f u_j(z) d_s / \mu_f$ .

Unlike in the dilute phase, no abrupt change was observed in the axial variation of mass transfer characteristics in the dense phase. However, as shown in Figure 3.6, the data are correlated quite differently, depending on the Reynolds number based on the inert particle size,  $Re_s$ . The proposed correlations for mass transfer in the dense phase are

$$Sh_d(z) = 2\epsilon_d(z) + 0.047 Re_d^{1.4}(z) Sc^{1/3} \quad (3.34)$$

$$\text{for } 10 < Re_d < 70 \text{ and } 1 < Re_{s,d} < 4.5$$

$$Sh_d(z) = 2\epsilon_d(z) + 0.001 Re_d^{2.65}(z) Sc^{1/3} \quad (3.35)$$

$$\text{for } 7 < Re_d < 20 \text{ and } 0.45 < Re_{s,d} < 1$$

where  $Re_d(z) = \rho_f u_d(z) d_p / \mu_f$  and  $Re_{s,d}(z) = \rho_f u_d(z) d_s / \mu_f$

Noting that the ranges of both Reynolds numbers for Eqs. (3.33) and (3.34) are almost identical, the data for the upper zone of the dilute phase and for the dense phase are plotted together in Figure 3.7 and shown to be well represented by a single correlation:

$$Sh = 2\epsilon(z) + 0.094 Re^{1.22}(z) Sc^{1/3} \quad (3.36)$$

for  $10 < Re < 70$  and  $0.3 < Re_s < 5$

where both  $\epsilon$  and  $u$  are calculated differently in each phase, as outlined earlier in this section. This result appears to be surprising but is indeed consistent with our definition of the grid region height, because all hydrodynamic parameters eventually become identical at  $z = H$  so that mass transfer data in both phases should be correlated by the same type of expression, as shown in Figure 3.7.

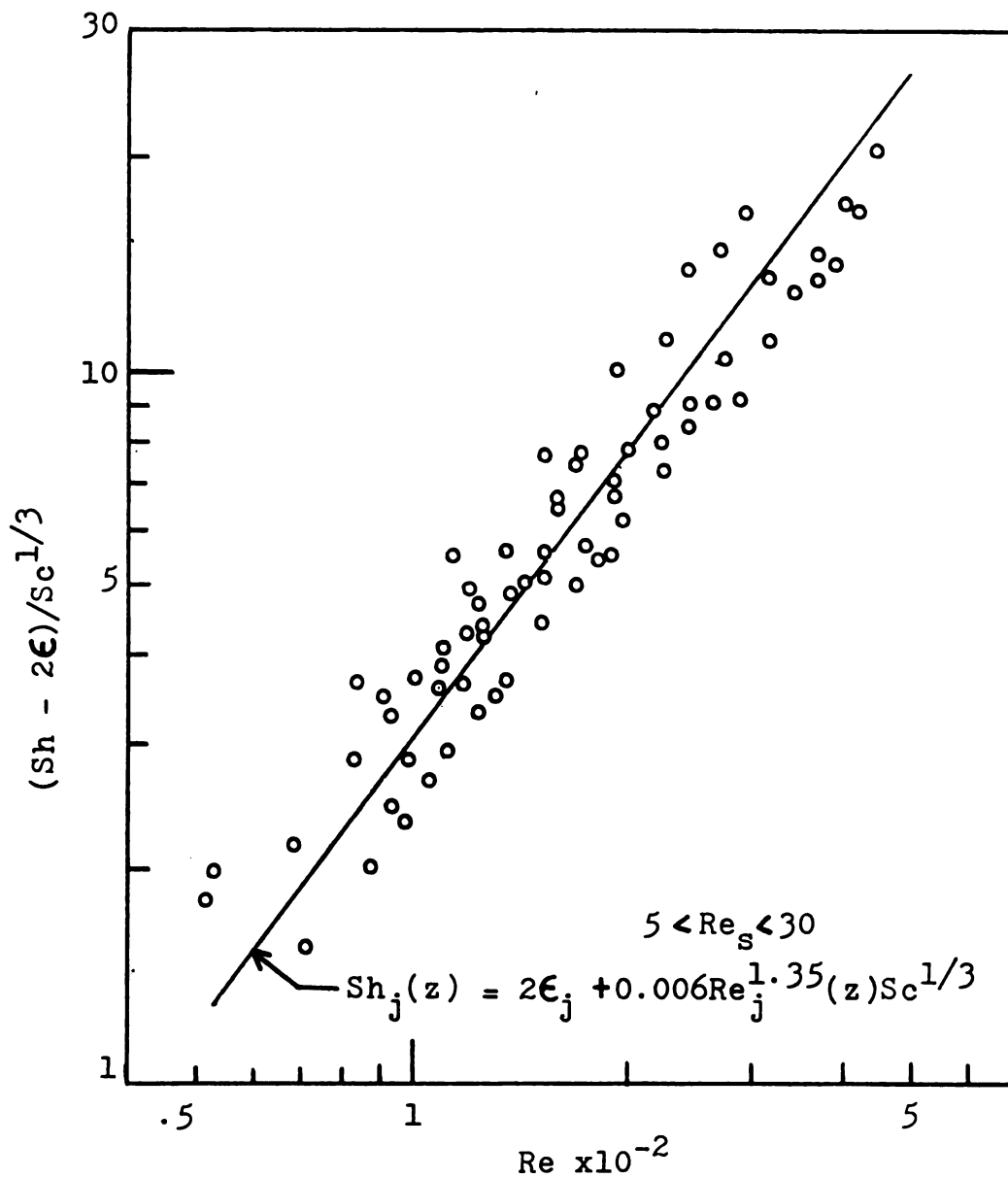


Figure 3.4 Plot of  $\ln[(Sh - 2\epsilon)/Sc^{1/3}]$  versus  $\ln Re$  in the dilute phase for  $0 \leq z < h_e$ .

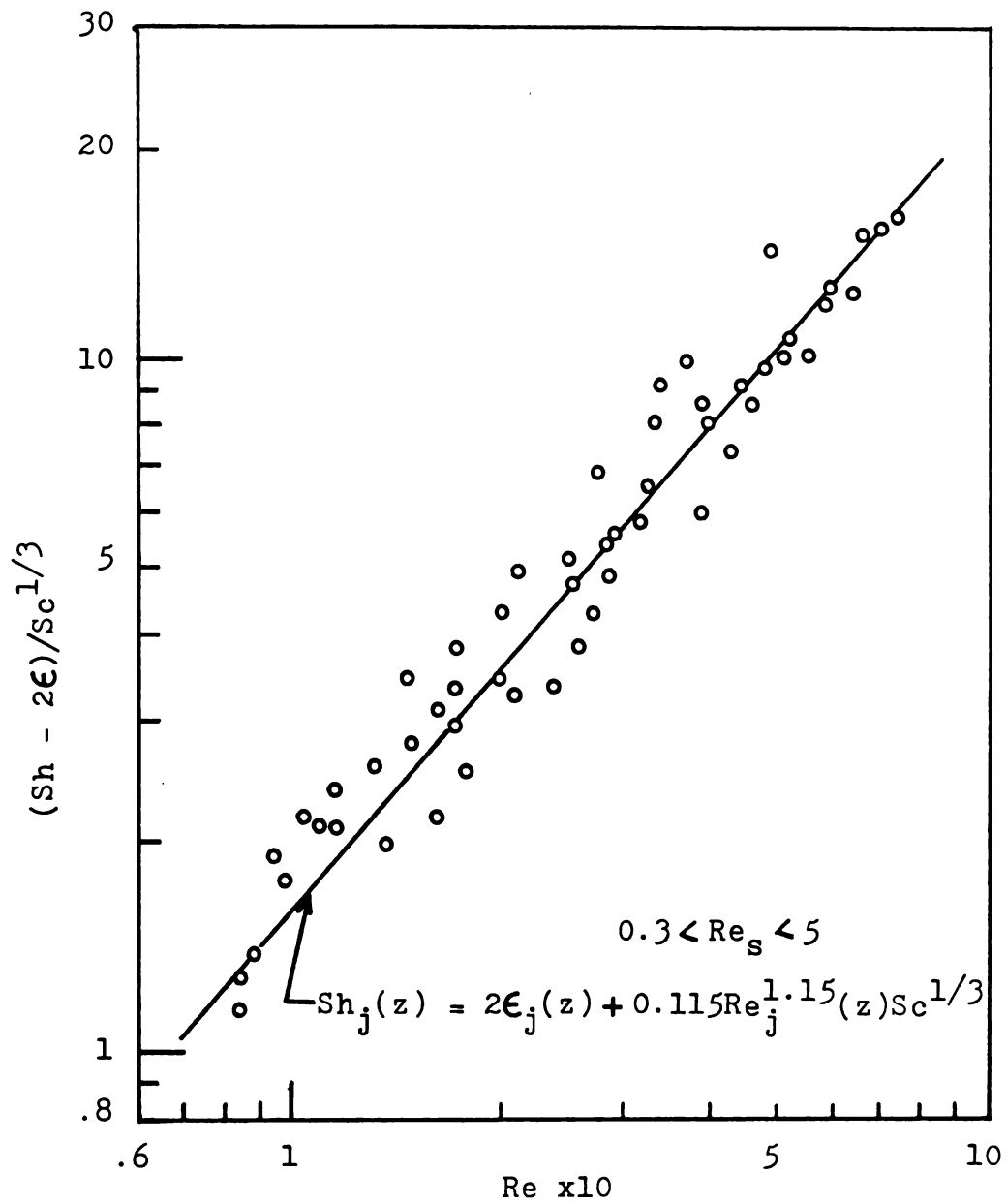


Figure 3.5 Plot of  $\ln[(Sh - 2\epsilon)/Sc^{1/3}]$  versus  $\ln Re$  in the dilute phase for  $h_e \leq z \leq H$ .

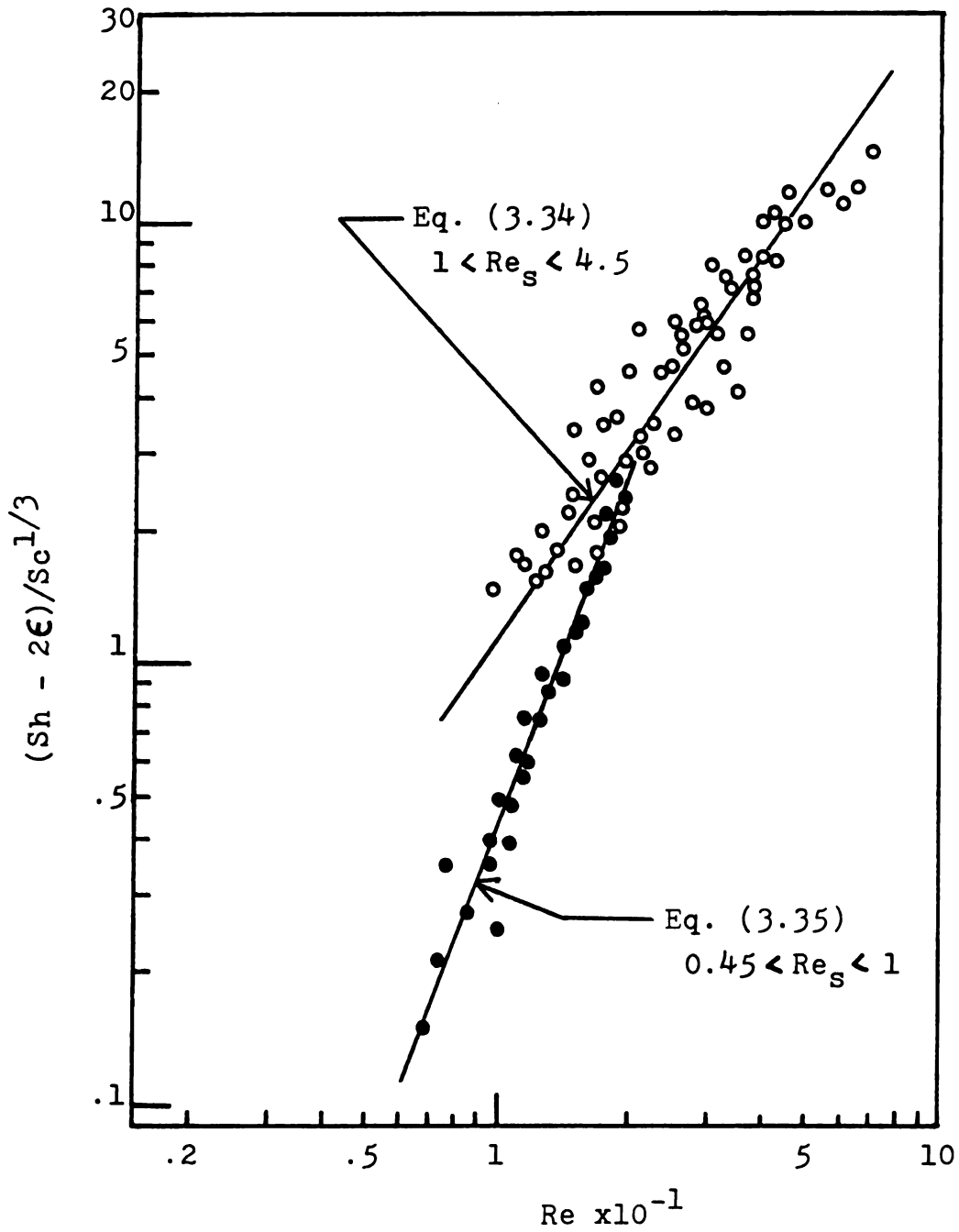


Figure 3.6 Plot of  $\ln[(Sh - 2\epsilon)/Sc^{1/3}]$  versus  $\ln Re$  in the dense phase for  $0 < z \leq H$ .

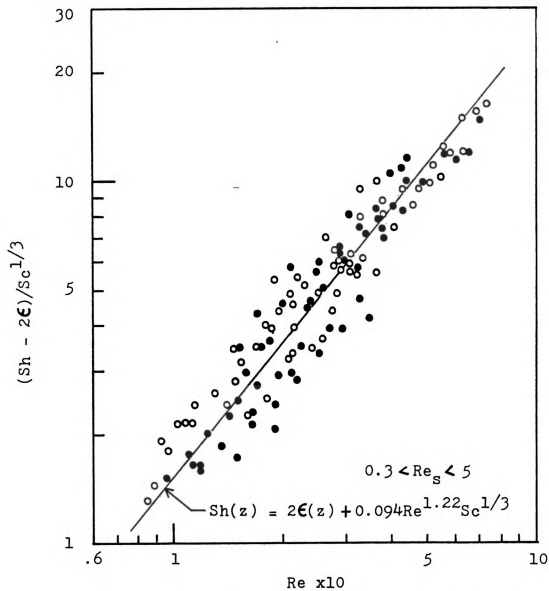


Figure 3.7 Plot of  $\ln[(Sh - 2\epsilon)/Sc^{1/3}]$  versus  $\ln Re$  ( dilute phase (open symbol ), dense phase (closed symbol) ).

### 3-4. Discussion

It should be noted that in our study, carbon particles were fixed at various positions in order to characterize the effects of bed hydrodynamics on the combustion and mass transfer rates as a function of particle position in both phases of the grid region. In actual practice, however, active particles are also entrained into the jet along with inert particles, accelerated and carried to the top of the jet where some particles are swept into the wake of each rising bubble, while the remaining particles are returning to the dense phase. Therefore, the interstitial gas velocity,  $u(z)$ , in Eqs. (3.32)-(3.36) should be replaced by the relative velocity between gas and solids,  $u_R = u(z) - v(z)$ , which is essentially the same as  $u(z)$  in packed and fluidized beds (60). Hence, Eqs. (3.34)-(3.36) can be directly applied to actual situations.

On the other hand, the particle velocity in the dilute phase,  $v_j(z)$ , is expected to be more pronounced perhaps due to high rates of momentum transfer in the jet, and can be calculated numerically from the mass and momentum balance equations (56). However, the calculations showed that for bed materials similar to the ones typically encountered in a fluidized bed combustor, the ratio of  $v_j(z) / u_j(z)$  is still at most 10 % for all  $z$  (68), which is certainly well within the range of experimental errors, as shown by the degree of data scattering in Figures 3.4 and 3.5. This relatively small velocity ratio is mainly due to the fact that unlike other two-phase jet flows, a significant

amount of gas flow entering the bed with high momentum quickly leaks throughout the jet boundary to fluidize the dense phase, instead of transferring momentum to the particles entrained in the jet. It is, therefore, suggested that Eqs. (3.32) and (3.33) be used in actual situations under the operating conditions considered in this study.

Bar-Ilan and Resnick (62) measured the rate of vaporization of naphthalene particles in a packed bed of inert particles of similar size and shape, and their data with 460  $\mu\text{m}$  granules are shown in Figure 3.8 to be reasonably well fitted by Eq. (3.34). It should be noted that the size reduction of active particles during the transfer process was assumed to be negligible in their study, whereas the active particle size is explicitly shown in each correlation proposed in this study so that this important problem of particle size variation can still be accommodated for a broader range of applications. They also found that the mass transfer characteristics changed drastically at Reynolds numbers ( $Re_s$ ) around unity, which is basically consistent with our results, as shown in Figure 3.6. Furthermore, the transition from a laminar to a turbulent flow regime in a packed bed is known to occur at Reynolds numbers ( $Re_s$ ) around 5 (63). Therefore, it appears that Eqs. (3.34) and (3.35) are generally applicable to diluted systems in laminar flow for  $Re_s > 0.3$ .

For  $Re_s < 0.3$ , the experimental Sherwood numbers are extremely small, as shown in Figure 2.39 for 230 $\mu\text{m}$  sand, and it is no longer possible to represent the data in the form of Eq. (3.6). Hence, the mechanism of mass transfer is mainly molecular diffusion at these low

Reynolds numbers, and the Sherwood numbers can be assumed to be effectively  $2\epsilon$ .

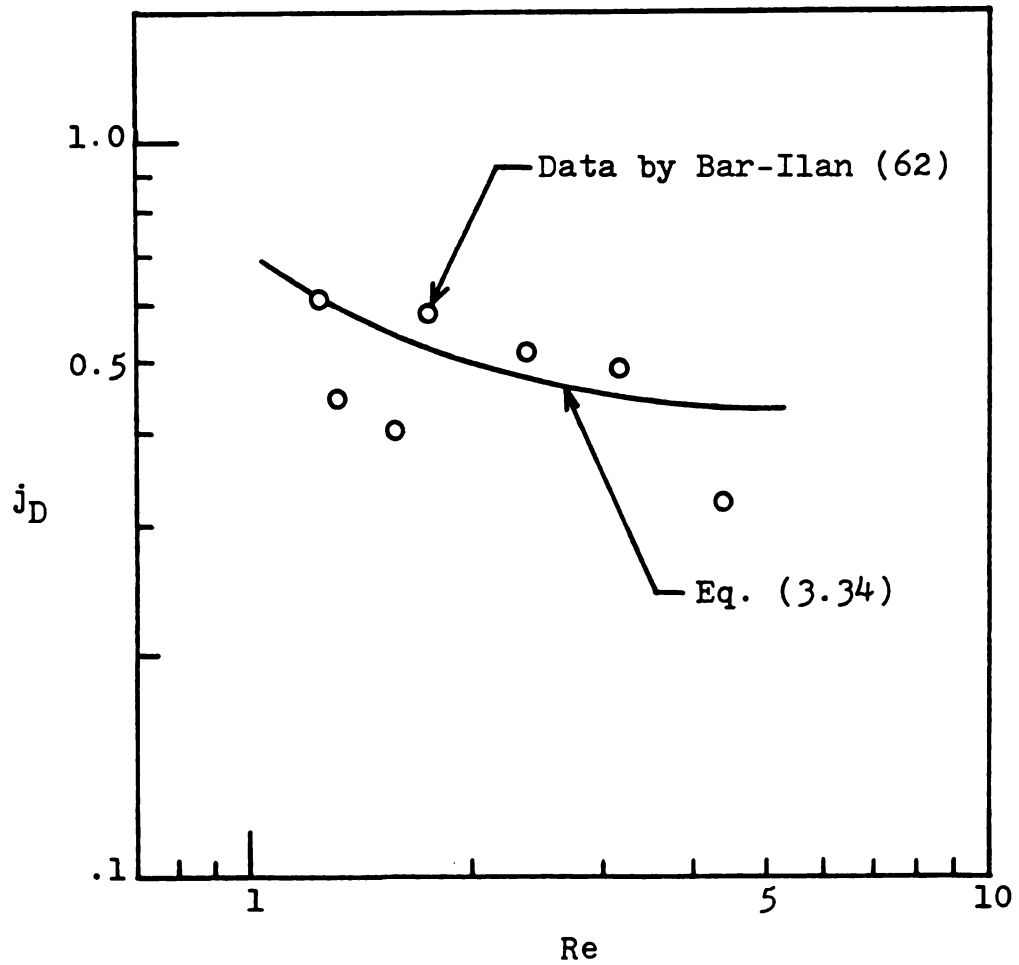


Fig. 3.8 Mass transfer factor versus Reynolds number in a diluted system.

### 3-4. Estimation of the Dead Zone Height

The dead zone is commonly defined as a portion of the dense phase in which the particles are stationary, as in a fixed bed. In the absence of any appreciable convective effects, the particles are certainly immobile and still maintain their overall tranquility with increasing gas flow, until the superficial gas velocity reaches a critical value of  $U_{mf}$ . It was shown experimentally that the dense phase becomes completely fluidized at  $z = h_e$  (52), whereas Figure 3.9 shows that the superficial gas velocities at  $z = h_e$  far exceed their values at minimum fluidization for all sand particle sizes considered. This discrepancy may appear to be somewhat unexpected but nevertheless is consistent with the experimental observations of Yates et al. (18) that the local dense phase voidage increases above its minimum fluidization value during the bubble formation. It should be noted here that the dense phase voidage was already assumed to increase linearly from  $\epsilon_{mf}$  at  $z = h_d$  to  $\epsilon_b$  at  $z = H$  in the analysis given in Section 3-3-3. Consequently, the dense phase is expected to become unstable due to this excessive local expansion, and it is these instabilities that disturb the tranquility of stationary particles. Therefore, the dead zone height,  $h_d$ , is likely to be at or a little above where  $U_d(z) = U_{mf}$ .

Horio et al. (75) directly measured the dead zone shape by the wax quenching method in a three-dimensional bed and proposed the following correlations for the dead zone height:

$$d_m/D_o = 4.4 \times 10^{-3} U_o^{1.5} + 1.75 \quad (3.37)$$

$$h_d = 0.5 (S - d_m) \tan \theta_r \quad (3.38)$$

where  $d_m$  is called the particle moving zone diameter, and  $\theta_r$  is the angle of repose which is commonly taken as  $37^\circ$  for the sand particle sizes considered in this study.

As expected, it can be seen from Table 3.3 that the values of  $h_d$  calculated from Eqs. (3.37) and (3.38) are generally higher than those based on the assumption of  $U_d(h_d) = U_{mf}$  and still considerably lower than those  $h_e$ . It is also to be noted that the calculated values of  $h_d$  are shown to be rather insensitive to  $U_o$  which is the only variable affecting the dead zone formation for a given distributor pitch size. The critical gas velocity required for the elimination of the dead zone can be calculated simply by letting  $d_m = S$  in Eq. (3.37) and solving for  $U_o$ . Its value for our case is estimated to be about 136 m/s which is more than 12  $U_{mf}$  even for 620  $\mu\text{m}$  sand. At these high gas flow rates, the elutriation rate of bed materials is so high that the elimination of the dead zone is possible only by reducing the pitch size.

Table 3.3 Estimated values of the dead zone height

$d_s$ ( $\mu\text{m}$ )	$U_o$ (m/s)	$h_d$ (cm) from $U_d(h_d) = U_{mf}$	$h_d$ (cm)	$h_e$ (cm)
			calculated from Eqs. (3.37) and (3.38)	
230	4.7	1.24	1.67	5.9
	6.2	.82	1.66	4.4
	9.4	.50	1.65	2.9
460	9.4	2.77	1.65	10.1
	12.5	1.85	1.63	7.3
	25.0	.78	1.54	3.5
620	22.6	2.32	1.56	6.3
	33.8	1.37	1.47	4.3
	45.1	.85	1.36	2.2

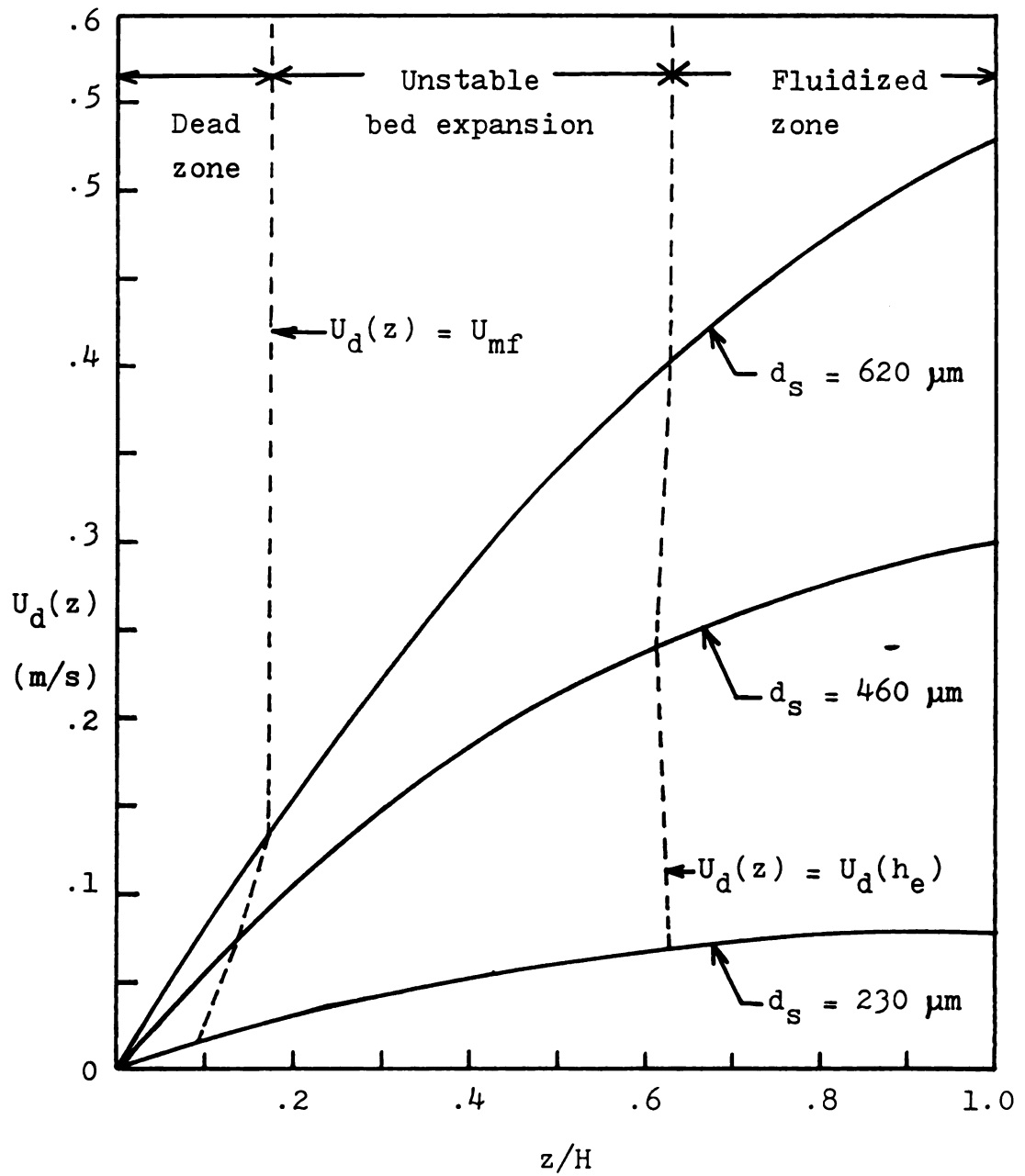


Figure 3.9 Axial velocity distribution in the dense phase at  $U = 4 U_{mf}$ .

**CHAPTER 4**

**SUMMARY OF CONCLUSIONS AND SUGGESTIONS**

**FOR FUTURE RESEARCH**

#### 4-1. Summary of Conclusions

The grid region can account for a major component of gas and solids contacting, compensating for poor contacting in the bubbling and slugging zones. Consequently, understanding the hydrodynamics and transfer processes in the grid region is crucial to successful modeling of fluidized bed reactors (76). In this study, we were particularly concerned with combustion and mass transfer characteristics in the grid region of a fluidized bed combustor. Specifically, we aimed at:

1. experimentally measuring the grid region height from a reaction point of view, which is useful for the modeling purpose,
2. characterizing the combustion and mass transfer phenomena in the dilute and dense phases of the grid region,
3. and developing mass transfer correlations for the dilute and dense phases of the grid region.

The experimental methods involved measuring combustion rates of sample carbon particles fixed at various locations near a multi-orifice gas distributor. The operating variables considered in this study were inert particle size, superficial gas velocity and particle position. Noting that there are many hydrodynamic similarities between a spouted bed at minimum spouting and the grid region at minimum fluidization, the experimental results were further analyzed in light of theories for

spouted beds and two-phase flows. The following is a summary of conclusions on the experimental and theoretical results.

4-1-1. Conclusions on single particle experiments

1. For unreactive carbons such as electrode graphite, the chemical kinetics plays an important role in fluidized bed combustion, and combustion cannot be assumed to be in a shrinking sphere mode at high fractional burn-off due to a significant internal burning.
2. Due to solids entrainment and gas leakage, the external mass transfer resistance of the dilute phase increases with increasing distance from the distributor, thus lowering the overall combustion rate, while the reverse trend is observed in the dense phase.
3. The grid region height was defined as where the bubbles deviate from their vertical path due to bed momentum, and its values determined experimentally are all consistent with its own definition in the sense that the mass transfer as well as the combustion characteristics are the same regardless of the sample position above the grid region height.
4. The grid region height decreases with increasing gas flow rate for all sand particle sizes considered in this study,

and available correlations for jet penetration length cannot be used in the reactor modeling study.

5. Under the operating conditions considered in this study, the grid region occupies up to 40 % of the entire bed volume and cannot be neglected in the overall reactor modeling study.
6. In the dilute phase of large inert particles, the overall combustion rate increases with increasing gas flow rate mainly due to the increase in the chemical rate. As the inert particle size decreases, the influence of the chemical kinetics diminishes, and the overall combustion rate is affected by the gas flow rate mainly due to the change in mass transfer resistance in a bed of small inert particles. In the dense phase, the corresponding trends are reversed.
7. At a constant gas velocity, the effect of increasing inert particle size is to decrease the overall combustion rate in the dilute phase due to the increase in the mass transfer resistance, while the trend is again reversed in the dense phase.
8. From Conclusions #6 and #7, it can be concluded that gas leakage into the dense phase increases with increasing inert particle size perhaps due to the difficulties associated with fluidizing larger particles.

9. Both the mass transfer coefficient and voidage of the dilute phase decrease with upward concavity with increasing distance from the distributor, and the concavity smooths out with decreasing inert particle size. In the dense phase, both quantities increase gradually with increasing distance from the distributor.

4-1-2. Conclusions on the theoretical analysis

1. The general behavior of gas and solids flows in the grid region at minimum fluidization can be assumed to be identical to that of a spouted bed at minimum spouting.
2. The dilute phase can be further divided into the upper and lower zone around  $z = h_e$ , with each zone exhibiting mass transfer characteristics quite different from each other, and this is found to be consistent with the hydrodynamic picture of the dilute phase outlined in the definition of the grid region height.
3. The experimental Sherwood numbers are represented by one of the following generalized correlations:

$$Sh = 2\epsilon + 0.006 Re^{1.35} Sc^{1/3} \quad (4.1)$$

for  $70 < Re_p < 500$  and  $5 < Re_s < 30$

$$Sh = 2\epsilon + 0.094 Re^{1.22} Sc^{1/3} \quad (4.2)$$

for  $10 < Re_p < 70$  and  $0.3 < Re_s < 5$

$$Sh = 2\epsilon \quad (4.3)$$

for  $Re_p < 10$  and  $Re_s < 0.3$

where  $Re_p = \rho_f u d_p / \mu_f$  and  $Re_s = \rho_f u d_s / \mu_f$ . It should be noted that both  $\epsilon$  and  $u$  are calculated differently in each phase, as outlined in Section 3-3-5.

The significance of this study is that the experimental technique of determining the grid region height can be readily employed in other fluidized bed applications for its estimation. Furthermore, the proposed mass transfer correlations can accommodate the size variation of active particles during the transfer processes and are shown to be also applicable to other diluted systems.

#### 4-2. Suggestions for Future Research

This study was initiated from the need of developing a combustion model in the grid region which can later be combined with bubbling bed models for better prediction of the overall bed performance. As shown in Figure 4.1, both experimental and theoretical works presented in this study are concerned with only a small portion of the overall scope of research needed for the combustion modeling of the grid region. Here, we describe briefly some of the research areas of immediate concern.

1. More combustion experiments need be done in the grid region involving reactive carbons of known chemical reactivity to determine the relative importance of the chemical kinetics and mass transfer on the overall combustion rate.
2. The grid region height is perhaps the most important of all modeling parameters. Dedicated efforts need be put into experimentally measuring the grid region height under a wider range of operating conditions for possible development of a correlation.
3. Accurate prediction of particle temperature requires further research toward developing a model of simultaneous heat and mass transfer and CO oxidation in the boundary layer.

4. Hydrodynamic experiments using the fiber optic probe will give a detailed picture of the complicated gas and solids flows in the grid region. The jet boundary, solids entrainment rate and residence time distribution of solids in the dilute and dense phases can be estimated by further statistical treatment of the data, and a comprehensive hydrodynamic modeling study should follow for the generalization of data.
  
5. In the grid region, the size reduction of carbon particles due to fragmentation and attrition caused by the impact with inert bed particles is likely to be significant due to vigorous gas and solids mixing in the jet and high temperature gradient. A pattern of the attrition activity as a function of burn-off % can be obtained by careful experimentation of monitoring the weight loss of carbon particles, already burnt to different degrees of burn-off, during a short stay in a shallow bed fluidized by  $N_2$ . The type and external surface area of carbon particles, inert particle size and gas velocity seem to be the important variables in the modeling study.

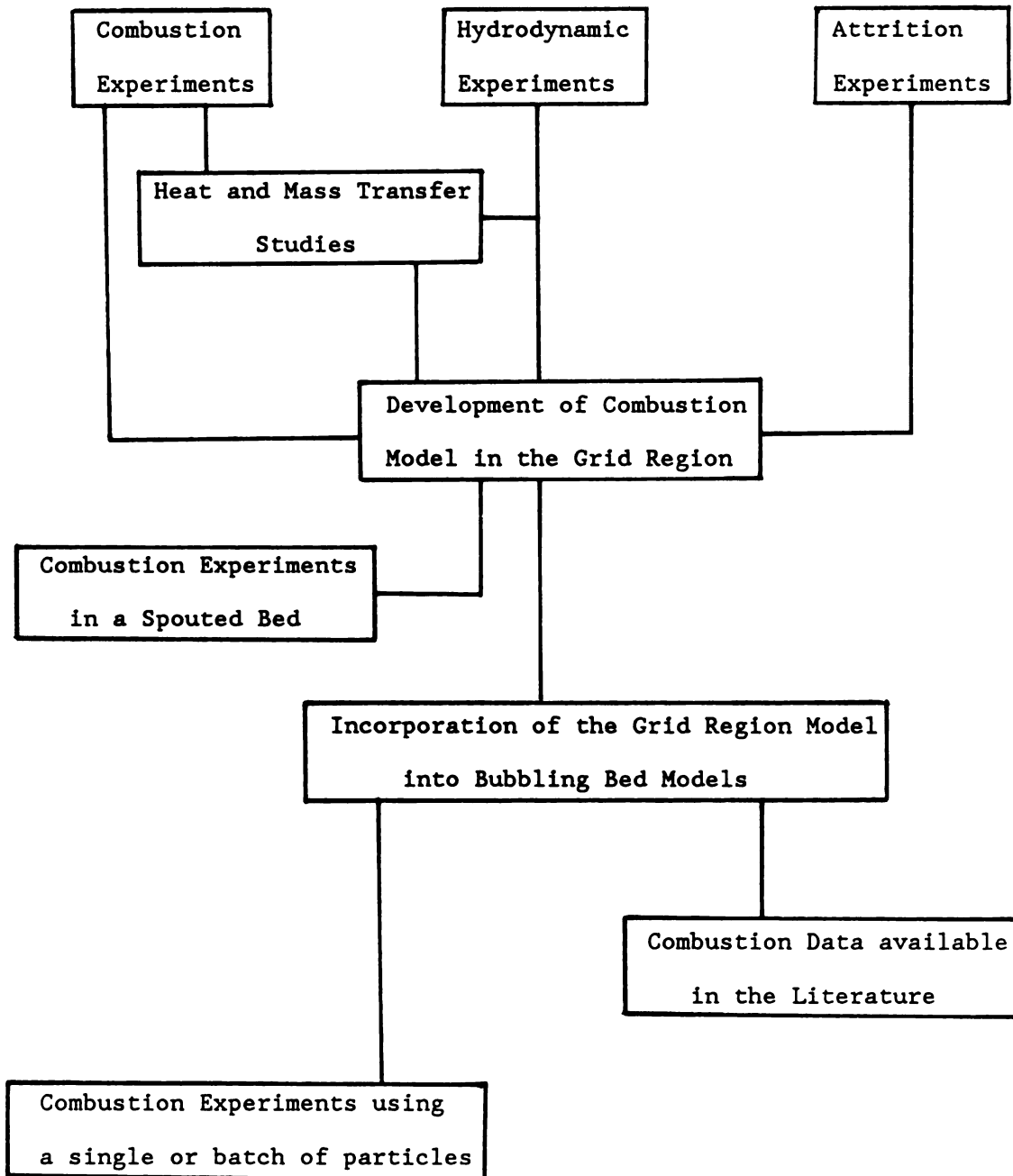


Figure 4.1 Research plan for the overall combustion modeling.

## **APPENDIX**

A-1. Design of Gas Distributors

If the pressure drop across a gas distributor is too low, not all orifices are in continuous operation, and the result is poor fluidization. The pitch size and orifice diameter have already been set by the experimental conditions, and we now determine the thickness of the multi-orifice distributor which will give the pressure drop high enough for uniform gas distribution.

The pressure drop across the bed for  $U \geq U_{mf}$  is

$$\Delta P_B = (\rho_s - \rho_f)(1 - \epsilon_{mf})H_{mf} g \quad (A.1)$$

$$= (2700 - 0.3892)(1 - 0.4)(0.20)(9.8)$$

$$= 3175.2 \text{ N/m}^2$$

where  $H_{mf}$  is set at 20 cm, the static bed height, for all  $d_s$ 's considered.

Quereshi and Creasy (77) proposed the following expression for the pressure drop ratio for stable operation:

$$\Delta P_D / \Delta P_B \geq 0.01 + 0.2 \left[ 1 - \exp(-0.5 D_B / H_{mf}) \right] \quad (A.2)$$

$$\text{Hence, } \Delta P_D \geq 0.0717 \Delta P_B = 240 \text{ N/m}^2$$

Furthermore, Geldart and Baeyens (78) derived the following expression for  $\Delta P_D$ :

$$\Delta P_D = \frac{6G^2}{\pi^2 C_D^2 \rho_f} \left( \frac{S}{D_o} \right)^4 \quad (\text{A.3})$$

where  $G$  is the mass flux of gas and  $C_D$  is the discharge coefficient at the orifice. Hence,  $\Delta P_D$  is minimum at the lowest mass flux, and

$$G_{\min} = 7.3 \times 10^{-3} \text{ kg/m}^2 \text{ s at } U = 3 U_{mf} \text{ for } 230 \text{ } \mu\text{m sand.}$$

Upon rearranging Eq. (A.3),

$$C_D = \left[ \frac{6G_{\min}^2}{\pi^2 \rho_f (\Delta P_D)_{\min}} \right]^{1/2} \left( \frac{S}{D_o} \right)^2 \quad (\text{A.4})$$

$$= \left[ \frac{6 (7.2 \times 10^{-3})^2}{\pi^2 (0.3892) (240)} \right]^{1/2} \left( \frac{0.0556}{0.00635} \right)^2$$

$$= 0.0445$$

Quereshi and Creasy (77) further suggested

$$C_D = 0.82 (L_D / D_o)^{0.13} \quad (\text{A.5})$$

for  $L_D / D_o > 0.09$ , where  $L_D$  is the thickness of the gas distributor.

Solving Eq. (A.5) for  $L_D$ , we have

$$L_D = 9.27 \times 10^{-3} \text{ m}$$

## A-2. Sample Calculations

### A-2-1. Particle terminal velocity

The upper limit to gas flow rate through a fluidized bed is approximated by the terminal velocity of particles (79):

$$u_t = \left[ \frac{4 g d_s (\rho_s - \rho_f)}{3 \rho_f C_d} \right]^{1/2} \quad (\text{A.6})$$

where the drag coefficient,  $C_d$ , for spherical particles is given as:

$$C_d = \frac{10}{\text{Re}_s^{1/2}} \quad \text{for } 0.4 < \text{Re}_s < 500 \quad (\text{A.7})$$

Combining Eqs. (A.6) and (A.7), we obtain

$$u_t = \left[ \frac{4}{225} \frac{(\rho_s - \rho_f)^2 g^2}{\rho_f \mu_f} \right]^{1/3} d_s \quad (\text{A.8})$$

for  $0.4 < Re_s < 500$

For 620  $\mu\text{m}$  sand,

$$u_t = \left[ \frac{4}{225} \frac{(2700 - 0.3892)^2 (9.8)^2}{(0.3892)(0.000046)} \right]^{1/3} (0.00062)$$

$$= 5.49 \text{ m/s}$$

And  $Re_s = \frac{\rho_f u_t d_s}{\mu_f} = 28.8$       Hence,  $0.4 < Re_s < 500$

#### A-2-2. Calculation of $\epsilon$ and $u$

The experimental conditions of Run number 26 are given in Table 2.2 as  $d_s = 0.00062 \text{ m}$ ,  $U = 0.53 \text{ m/s}$ ,  $U_o = 45.1 \text{ m/s}$  and  $z = 2.54 \text{ cm}$ .

Furthermore, from Table 2.5,  $H_{mf} = 0.112 \text{ m}$  and  $H = 0.051 \text{ m}$ .

First calculate  $\epsilon$  and  $u$  in the dilute phase. The jet diameter for 620  $\mu\text{m}$  sand is

$$D_j = 1.06 D_c^{2/3} d_s^{1/3} \quad (3.17)$$

$$= 1.06 (0.0586)^{2/3} (0.00062)^{1/3}$$

$$= 0.0136 \text{ m}$$

At minimum fluidization,

$$I_o = \frac{\Delta P_{ms}}{\Delta P_{mf}} + \frac{\rho_f \left[ (D_o/D_j)^4 U_{o,mf}^2 - U_{mf}^2 / \epsilon_{mf} \right]}{(1 - \epsilon_{mf}) (\rho_s - \rho_f) g H_{mf}} \quad (3.12)$$

$$= 0.75 + \frac{(0.3892) \left[ (0.00635/0.0136)^4 (45.1/4)^2 - 0.53^2 / 0.4 \right]}{(1 - 0.4) (2700 - 0.3892) (9.8) (0.112)}$$

$$= 0.7513 \approx 0.75$$

From Figure 3.2, at  $z = 2.54$  cm or  $\zeta = 2.54/11.2 = 0.23$ ,  $\epsilon_{j,mf} = 0.63$

Hence, the dilute phase voidage at  $U = 4 U_{mf}$  becomes

$$\epsilon_j(2.54 \text{ cm}) = 1 - \left[ 1 - [\epsilon_j(2.54 \text{ cm})]_{mf} \right] \left( \frac{1 - \epsilon_b}{1 - \epsilon_{mf}} \right) \quad (3.19)$$

$$= 1 - (1 - 0.63) \left( \frac{1 - 0.562}{1 - 0.4} \right) = 0.73$$

From Eq. (3.29), the interstitial gas velocity then becomes

$$u_j(2.54 \text{ cm}) = \frac{1}{0.73} \left[ (45.1) \left( \frac{0.00635}{0.0136} \right)^2 + (0.53) \left[ 1 - \left( \frac{0.0586}{0.0136} \right)^2 \right] \left( \frac{1 - (1 - 2.54/11.2)^3}{1 - (1 - 5.1/11.2)^3} \right) \right]$$

$$= 5.28 \text{ m/s}$$

Furthermore,

$$Re_{s,j}(2.54 \text{ cm}) = \frac{(0.3892)(5.28)(0.00062)}{(0.000046)} = 27.7$$

Since the dead zone height is lower than 2.54 cm, the sample is in the unstable expansion zone, and the dense phase voidage becomes, from Eq. (3.22),

$$\begin{aligned} \epsilon_d(2.54 \text{ cm}) &= \frac{1}{5.1 - 0.85} \left[ (0.562 - 0.4)(2.54) + (0.4)(5.1) \right. \\ &\quad \left. - (0.562)(0.85) \right] \\ &= 0.464 \end{aligned}$$

Furthermore, from Eq. (3.25),

$$\begin{aligned} U_d(2.54 \text{ cm}) &= (0.53) \left[ \frac{1 - (1 - 2.54/11.2)^3}{1 - (1 - 5.1/11.2)^3} \right] \\ &= 0.34 \text{ m/s} \end{aligned}$$

Hence, the interstitial gas velocity in the dense phase becomes

$$u_d(2.54 \text{ cm}) = 0.34 / 0.464 = 0.733 \text{ m/s}$$

And  $Re_{s,d}(2.54 \text{ cm}) = 3.85$

A-2-3. Calculation of  $R_c$ ,  $\phi$  and Sh

The quantities measured experimentally for fixed samples are the initial and final diameters of a carbon sphere,  $d_{p,i}$  and  $d_{p,f}$  respectively, and the particle temperature during one combustion interval of  $t$  seconds. The combustion rate per unit external surface area is given as:

$$R_c = \Delta W / t \pi d_p^2 \quad (2.6)$$

$$= \rho_p (d_{p,i}^3 - d_{p,f}^3) / 6 t d_p^2$$

where  $d_p = (d_{p,i} + d_{p,f}) / 2$ , and  $\rho_p = 600 d_p^{0.4}$ .

For example, in Run # 21,  $d_{p,i} = 9.864 \times 10^{-3}$  m,  $d_{p,f} = 9.275 \times 10^{-3}$  m,  $T_p = 1258$  K, and  $t = 90$  seconds.

Hence,

$$R_c = 600 (9.57 \times 10^{-3})^{0.4} \left[ [(9.864 \times 10^{-3})^3 - (9.275 \times 10^{-3})^3] \right]$$

$$/ (6)(90)(9.57 \times 10^{-3})^2$$

$$= 4.85 \times 10^{-3} \text{ kgC} / \text{m}^2 \text{ s.}$$

Furthermore,

$$k_c = A \exp(-E_a / R T_p) \quad (2.7)$$

$$= 87000 \exp(-36000 / (1.987)(1258))$$

$$= 4.84 \times 10^{-2} \text{ kgC} / \text{m}^2 \text{ s atm}$$

For  $n = 1$ , Eq. (2.5) can be rewritten as:

$$\phi = 1 - R_c / k_c C_o$$

$$= 1 - (4.85 \times 10^{-3}) / (4.84 \times 10^{-2})(0.21)$$

$$= 0.523$$

In order to calculate the Sherwood number from Eq. (2.9), the oxygen concentration of incoming air must be in  $\text{kg} / \text{m}^3$ , instead of in atm. Assuming an ideal gas,

$$C_o = \frac{P_{O_2} (MW)_{O_2}}{RT}$$

$$= \frac{(0.21)(32)}{(82.057)(1163)} = 0.0704 \text{ kg} / \text{m}^3$$

Furthermore, the variation of  $D_g$  with temperature is calculated using the following equation by Fujita (80):

$$\begin{aligned}
 D_g(T) &= D_g(273 \text{ K}) (T / 273)^{1.823} \\
 &= [1.81 \times 10^{-5} \text{ m}^2 / \text{s}] (1163 / 273) \\
 &= 2.542 \times 10^{-4} \text{ m}^2 / \text{s}
 \end{aligned}$$

Hence,

$$\begin{aligned}
 \text{Sh} &= \frac{k_m d_p}{D_g} = \frac{R_c d_p}{\beta \phi D_g C_o} \\
 &= \frac{(0.00485)(0.00957)}{(0.375)(0.523)(0.0005242)(0.0704)} \\
 &= 13.16
 \end{aligned}$$

A-3. Experimental Data

Table A.1 Experimental results (Run # 1)

	$d_p \times 10^2$ (m)	$T_p$ (K)	$R_c \times 10^4$ (kg/m <sup>2</sup> s)	$\phi$	Sh
dilute phase	.915	1218	23.0	.64	4.91
	.868	1216	22.6	.64	4.57
	.810	1216	22.7	.63	4.31
	.749	1218	23.5	.63	4.15
	.681	1221	25.9	.61	3.80
	.607	1221	26.4	.60	3.45
	.500	1223	27.0	.59	2.90
	dense phase	.948	1208	9.6	.83
.901		1213	9.2	.84	1.46
.867		1213	9.1	.85	1.38
.833		1223	8.6	.87	1.21
.788		1217	8.9	.86	1.22
.742		1218	8.4	.87	1.06
.696		1218	8.3	.87	.99
.648		1218	9.5	.85	1.07
.591		1215	9.7	.84	1.01
.529		1206	10.9	.80	1.07
.473		1206	10.5	.81	.91

Table A.2 Experimental results (Run # 2)

	$d_p \times 10^2$ (m)	$T_p$ (K)	$R_c \times 10^4$ (kg/m <sup>2</sup> s)	$\phi$	Sh
dilute phase	.971	1209	22.3	.61	5.32
	.916	1209	23.0	.59	5.27
	.860	1211	21.3	.63	4.29
	.807	1211	20.4	.65	3.75
	.750	1211	20.6	.65	3.55
	.663	1214	22.1	.63	2.43
	.568	1214	22.1	.63	2.93
	.500	1215	22.2	.64	2.60
	.425	1215	23.9	.61	2.47
	dense phase	.985	1206	16.6	.70
.926		1204	16.0	.70	3.15
.867		1206	15.0	.73	2.67
.829		1204	15.1	.72	2.60
.788		1207	16.4	.70	2.72
.721		1207	16.7	.70	2.56
.653		1207	15.5	.72	2.09
.656		1207	17.1	.69	2.23
.555		1207	17.2	.69	2.06
.499		1212	19.4	.67	2.13

Table A.3 Experimental results (Run # 3)

	$d_p \times 10^2$ (m)	$T_p$ (K)	$R_c \times 10^4$ (kg/m <sup>2</sup> s)	$\phi$	Sh
dilute phase	.957	1203	21.4	.59	5.12
	.905	1206	21.3	.61	4.69
	.851	1206	21.2	.61	4.38
	.797	1209	21.0	.63	3.95
	.741	1209	20.8	.63	3.61
	.684	1209	20.9	.63	3.35
	.624	1215	21.5	.65	3.08
	.560	1211	21.9	.62	2.93
	.492	1213	22.1	.63	2.57
	.419	1213	22.8	.62	2.30
dense phase	.952	1205	19.9	.63	4.46
	.880	1206	18.7	.66	3.71
	.831	1211	19.4	.67	3.60
	.756	1209	18.7	.67	3.14
	.682	1209	17.6	.69	2.58
	.603	1211	18.5	.68	2.43
	.519	1211	19.3	.67	2.23
	.457	1211	19.9	.66	2.05

Table A.4 Experimental results (Run # 4)

	$d_p \times 10^2$ (m)	$T_p$ (K)	$R_c \times 10^4$ (kg/m <sup>2</sup> s)	$\phi$	Sh
dilute phase	.938	1213	17.2	.71	3.35
	.854	1212	16.7	.72	2.96
	.788	1212	17.5	.70	2.92
	.741	1220	18.2	.72	2.78
	.693	1217	16.6	.73	2.33
	.646	1215	17.2	.72	2.30
	.595	1215	17.7	.71	2.20
	.542	1220	17.7	.73	1.96
	.484	1218	19.4	.69	2.01
	dense phase	.962	1207	18.5	.66
.917		1205	17.8	.67	3.61
.874		1206	16.7	.69	3.11
.832		1205	16.3	.70	2.89
.788		1206	17.9	.67	3.11
.740		1210	18.2	.68	2.92
.692		1207	17.0	.69	2.51
.645		1205	16.5	.69	2.28
.594		1206	18.7	.66	2.50
.538		1208	18.7	.67	2.23
.477	1208	20.0	.64	2.19	

Table A.5 Experimental results (Run # 5)

	$d_p \times 10^2$ (m)	$T_p$ (K)	$R_c \times 10^4$ (kg/m <sup>2</sup> s)	$\phi$	Sh
dilute phase	.977	1238	31.0	.61	7.32
	.900	1248	31.4	.65	6.40
	.850	1243	28.2	.67	5.30
	.776	1241	28.8	.65	5.08
	.725	1243	29.0	.66	4.72
	.673	1243	27.9	.67	4.14
	.617	1248	30.1	.67	4.12
	.560	1248	28.6	.68	3.48
	dense phase	.947	1198	14.3	.71
.904		1198	11.8	.76	2.09
.864		1198	12.0	.76	2.03
.827		1198	9.8	.80	1.51
.790		1198	11.6	.76	1.78
.649		1201	12.1	.76	1.53
.603		1202	11.9	.77	1.39
.556		1203	12.0	.77	1.28
.483		1204	13.9	.74	1.34

Table A.6 Experimental results (Run # 6)

	$d_p \times 10^2$ (m)	$T_p$ (K)	$R_c \times 10^4$ (kg/m <sup>2</sup> s)	$\phi$	Sh	
dilute phase	.917	1217	24.3	.61	5.39	
	.879	1211	22.1	.62	4.64	
	.842	1211	21.7	.63	4.32	
	.804	1214	21.9	.64	4.09	
	.745	1215	22.4	.63	3.93	
	.662	1217	22.9	.63	3.56	
	.598	1211	21.5	.63	3.02	
	.553	1214	23.8	.61	3.23	
	.503	1217	25.3	.60	3.17	
	.447	1218	26.9	.58	3.09	
	dense phase	.896	1217	21.6	.65	4.40
		.860	1213	21.9	.63	4.41
.822		1216	22.6	.63	4.36	
.784		1214	21.6	.65	3.77	
.724		1213	22.9	.62	4.00	
.660		1213	23.4	.61	3.78	
.592		1213	23.5	.60	3.43	
.520		1217	25.2	.60	3.25	
.466		1218	25.9	.59	3.04	
.407		1220	27.2	.58	2.83	

Table A.7 Experimental results (Run # 7)

	$d_p \times 10^2$ (m)	$T_p$ (K)	$R_c \times 10^4$ (kg/m <sup>2</sup> s)	$\phi$	Sh
dilute phase	.859	1285	45.5	.67	8.67
	.817	1293	45.2	.70	7.84
	.735	1298	48.3	.69	7.58
	.649	1290	44.4	.69	6.16
	.584	1303	47.6	.72	5.76
	.513	1303	45.8	.73	4.80
	.403	1305	50.8	.70	4.37
	dense phase	.933	1214	26.3	.56
.892		1214	23.4	.61	5.06
.855		1212	20.6	.65	4.03
.786		1212	23.3	.61	4.46
.715		1212	22.0	.62	3.75
.674		1211	23.1	.60	3.82
.608		1213	22.9	.62	3.36
.540		1215	23.1	.62	2.97
.458		1221	23.0	.65	2.40
.405		1221	25.0	.62	2.42

Table A.8 Experimental results (Run # 8)

	$d_p \times 10^2$ (m)	$T_p$ (K)	$R_c \times 10^4$ (kg/m <sup>2</sup> s)	$\phi$	Sh
dilute phase	.889	1228	33.5	.54	6.90
	.777	1233	33.2	.56	6.79
	.719	1231	31.4	.58	5.83
	.660	1231	32.2	.57	5.58
	.598	1238	32.8	.59	4.90
	.531	1233	33.9	.55	4.83
	.459	1238	34.6	.57	4.13
	.377	1243	37.8	.56	3.80
	dense phase	.928	1228	30.8	.57
.876		1231	31.2	.58	7.02
.824		1228	30.3	.58	6.43
.769		1233	32.4	.57	6.44
.713		1231	30.9	.58	5.60
.654		1238	32.3	.60	5.23
.593		1233	31.6	.58	4.76
.527		1241	33.6	.60	4.40
.456		1243	33.8	.60	3.78

Table A.9 Experimental results (Run # 9)

	$d_p \times 10^2$ (m)	$T_p$ (K)	$R_c \times 10^4$ (kg/m <sup>2</sup> s)	$\phi$	Sh
bubbling region	.958	1238	33.7	.58	8.24
	.903	1241	33.2	.60	7.38
	.848	1238	32.9	.59	6.98
	.761	1240	33.2	.60	6.22
	.638	1244	33.9	.61	5.23
	.539	1243	33.7	.61	4.45
	.465	1248	36.5	.60	4.22
	.382	1251	37.7	.60	3.58

Table A.10 Experimental results (Run # 10)

	$d_p \times 10^2$ (m)	$T_p$ (K)	$R_c \times 10^4$ (kg/m <sup>2</sup> s)	$\phi$	Sh
bubbling region	.958	1236	34.5	.57	8.59
	.874	1235	33.3	.57	7.56
	.788	1235	33.1	.58	6.67
	.645	1243	35.0	.59	5.89
	.445	1248	37.5	.59	4.23

Table A.11 Experimental results (Run # 11)

	$d_p \times 10^2$ (m)	$T_p$ (K)	$R_c \times 10^4$ (kg/m <sup>2</sup> s)	$\phi$	Sh
dilute phase	.933	1211	15.7	.73	2.97
	.822	1213	15.1	.75	2.46
	.783	1213	14.8	.75	2.29
	.710	1213	12.4	.79	1.65
	.674	1213	13.6	.77	1.76
	.593	1218	13.6	.79	1.52
	.530	1218	14.9	.76	1.54
	dense phase	.972	1220	6.9	.89
.891		1223	5.2	.92	.74
.809		1233	5.3	.93	.68
.770		1233	4.5	.94	.55
.734		1233	4.6	.94	.53
.696		1233	4.6	.94	.50
.658		1233	4.6	.94	.48
.616		1243	5.1	.94	.49
.571		1243	5.1	.94	.46
.522		1248	5.7	.94	.47

Table A.12 Experimental results (Run # 12)

	$d_p \times 10^2$ (m)	$T_p$ (K)	$R_c \times 10^4$ (kg/m <sup>2</sup> s)	$\phi$	Sh
dilute phase	.976	1208	10.2	.82	1.80
	.930	1208	8.7	.84	1.43
	.886	1208	8.8	.84	1.37
	.841	1208	9.0	.84	1.34
	.794	1210	9.2	.84	1.28
	.747	1210	8.6	.85	1.12
	.672	1208	9.3	.83	1.11
	.559	1212	10.2	.83	1.02
	.434	1213	14.4	.76	1.22
	.334	1216	15.4	.75	1.02
	dense phase	.983	1221	5.4	.92
.910		1225	6.0	.91	.90
.863		1220	6.7	.90	.96
.830		1223	6.2	.91	.84
.760		1223	6.4	.91	.79
.645		1225	7.0	.90	.75
.572		1228	7.7	.89	.73
.526		1243	7.5	.91	.64
.475		1227	8.9	.87	.71
.331		1228	11.9	.83	.70

Table A.13 Experimental results (Run # 13)

	$d_p \times 10^2$ (m)	$T_p$ (K)	$R_c \times 10^4$ (kg/m <sup>2</sup> s)	$\phi$	Sh
dilute	.976	1203	9.8	.87	1.14
phase	.909	1205	7.3	.87	1.13
	.834	1206	7.0	.87	1.00
	.753	1206	8.2	.85	1.07
	.710	1206	7.8	.86	.95
	.665	1206	8.7	.84	1.02
	.562	1209	9.1	.84	.91
	.507	1211	9.2	.84	.82
	.438	1211	11.4	.89	.91
	.352	1213	13.5	.77	.91
dense	.986	1209	6.5	.89	1.06
phase	.921	1213	7.1	.88	1.10
	.850	1214	7.3	.88	1.04
	.771	1212	7.9	.87	1.05
	.727	1212	8.6	.85	1.08
	.633	1216	8.4	.86	.91
	.580	1213	9.9	.83	1.03
	.519	1215	10.0	.84	.92
	.450	1218	11.5	.82	.94
	.377	1218	14.1	.78	1.01

Table A.14 Experimental results (Run # 14)

	$d_p \times 10^2$ (m)	$T_p$ (K)	$R_c \times 10^4$ (kg/m <sup>2</sup> s)	$\phi$	Sh
dilute	.997	1213	18.4	.69	3.94
phase	.929	1215	18.9	.69	3.78
	.833	1213	19.1	.68	3.47
	.758	1215	19.9	.67	3.31
	.704	1213	20.0	.66	3.15
	.649	1213	19.4	.68	2.76
	.593	1211	19.0	.67	2.49
	.534	1212	20.2	.66	2.44
	.467	1208	22.3	.60	2.56
	.386	1213	26.1	.56	2.66
dense	.966	1220	7.4	.89	1.20
phase	.873	1226	5.9	.91	.84
	.776	1223	5.7	.92	.72
	.730	1241	5.7	.93	.67
	.684	1236	5.6	.93	.62
	.581	1241	6.3	.92	.59
	.458	1241	7.3	.91	.54
	.376	1239	8.7	.89	.55

Table A.15 Experimental results (Run # 15)

	$d_p \times 10^2$ (m)	$T_p$ (K)	$R_c \times 10^4$ (kg/m <sup>2</sup> s)	$\phi$	Sh
dilute phase	.977	1200	8.5	.83	1.48
	.885	1205	9.4	.83	1.49
	.798	1201	8.5	.83	1.21
	.750	1198	9.4	.81	1.30
	.644	1205	10.1	.81	1.19
	.583	1204	10.9	.80	1.18
	.518	1206	10.8	.80	1.03
	.445	1208	11.9	.70	1.00
	.358	1210	13.3	.77	.92
	dense phase	.957	1215	6.5	.89
.878		1209	6.5	.89	.95
.790		1214	7.0	.88	.93
.733		1213	7.6	.87	.94
.693		1218	7.1	.89	.82
.651		1221	8.0	.88	.88
.553		1215	8.9	.85	.86
.500		1223	8.6	.87	.73
.439		1224	9.7	.86	.74
.366		1224	11.5	.83	.75

Table A.16 Experimental results (Run # 16)

	$d_p \times 10^2$ (m)	$T_p$ (K)	$R_c \times 10^4$ (kg/m <sup>2</sup> s)	$\phi$	Sh	
dilute phase	.978	1200	7.7	.85	1.31	
	.904	1202	6.8	.87	1.06	
	.872	1202	6.8	.87	1.02	
	.801	1203	7.0	.87	.96	
	.746	1203	6.7	.87	.85	
	.709	1203	7.1	.87	.86	
	.641	1204	8.5	.84	.96	
	.566	1205	8.8	.84	.89	
	.508	1205	10.1	.81	.93	
	.441	1208	10.6	.80	.86	
	.358	1208	13.4	.76	.94	
	dense phase	.985	1209	6.2	.89	1.03
		.899	1212	6.3	.89	.94
.835		1212	6.2	.89	.86	
.770		1213	6.3	.89	.81	
.702		1211	6.7	.88	.79	
.625		1217	6.8	.89	.70	
.537		1213	7.4	.88	.68	
.488		1213	8.3	.86	.69	
.432		1216	8.9	.86	.67	

Table A.17 Experimental results (Run # 17)

	$d_p \times 10^2$ (m)	$T_p$ (K)	$R_c \times 10^4$ (kg/m <sup>2</sup> s)	$\phi$	Sh
dilute phase	.955	1228	28.0	.61	6.50
	.900	1222	25.4	.62	5.49
	.858	1220	25.0	.62	5.17
	.766	1216	26.8	.57	5.31
	.664	1211	27.8	.51	5.23
	.610	1208	28.1	.50	5.11
	.554	1215	28.8	.53	4.47
	.492	1215	31.3	.49	4.68
	.423	1218	32.6	.49	4.20
	dense phase	.957	1204	6.8	.87
.904		1200	7.0	.86	1.10
.860		1200	6.7	.87	.99
.811		1200	6.2	.88	.83
.760		1202	6.8	.87	.88
.647		1202	7.3	.86	.81
.583		1202	7.5	.86	.76
.508		1202	8.9	.83	.80
.421		1204	9.2	.83	.68

Table A.18 Experimental results (Run # 18)

	$d_p \times 10^2$ (m)	$T_p$ (K)	$R_c \times 10^4$ (kg/m <sup>2</sup> s)	$\phi$	Sh
dilute phase	.994	1188	15.0	.65	3.39
	.890	1192	14.0	.69	2.66
	.853	1193	14.6	.69	2.70
	.764	1194	14.9	.68	2.38
	.691	1194	13.8	.71	2.00
	.654	1195	12.3	.74	1.61
	.619	1195	12.2	.74	1.50
	.584	1194	12.0	.75	1.39
	.510	1194	11.6	.75	1.17
	.472	1194	11.5	.73	1.19
dense phase	.972	1186	13.3	.69	2.80
	.924	1186	12.9	.70	2.54
	.859	1189	13.0	.70	2.36
	.810	1189	12.6	.71	2.13
	.713	1189	11.6	.74	1.67
	.665	1191	11.7	.74	1.56
	.578	1191	12.0	.73	1.41
	.521	1192	13.7	.70	1.50

Table A.19 Experimental results (Run # 19)

	$d_p \times 10^2$ (m)	$T_p$ (K)	$R_c \times 10^4$ (kg/m <sup>2</sup> s)	$\phi$	Sh
dilute phase	.959	1191	11.8	.74	2.27
	.864	1192	12.4	.73	2.18
	.772	1191	11.0	.76	1.66
	.722	1192	11.4	.75	1.62
	.624	1192	11.5	.75	1.43
	.567	1194	11.8	.75	1.33
	.503	1195	13.1	.72	1.35
	.430	1198	13.9	.72	1.24
	dense phase	.949	1191	12.6	.72
.901		1193	10.8	.77	1.88
.856		1193	10.6	.77	1.74
.751		1193	10.6	.77	1.53
.700		1190	11.9	.73	1.68
.643		1191	12.4	.73	1.63
.580		1191	13.5	.70	1.66
.511		1194	13.7	.71	1.47
.435		1196	14.4	.70	1.33

Table A.20 Experimental results (Run # 20)

	$d_p \times 10^2$ (m)	$T_p$ (K)	$R_c \times 10^4$ (kg/m <sup>2</sup> s)	$\phi$	Sh
dilute phase	.971	1285	58.8	.57	14.82
	.885	1293	59.8	.60	13.07
	.796	1293	61.6	.59	12.33
	.743	1298	57.7	.64	10.00
	.631	1303	62.0	.63	9.22
	.572	1305	57.8	.66	7.42
	.510	1313	63.9	.66	7.38
	.444	1318	60.6	.69	5.70
	.373	1308	65.5	.63	5.76
	.293	1318	63.2	.68	4.06
	dense phase	.937	1243	26.8	.69
.881		1243	27.3	.68	5.24
.834		1245	28.2	.68	5.20
.787		1245	26.3	.70	4.39
.740		1249	26.9	.71	4.18
.693		1253	24.3	.75	3.33
.636		1253	24.1	.75	3.04
.563		1256	25.6	.74	2.88
.481		1256	27.3	.73	2.69
.394		1256	25.4	.74	1.99

Table A.21 Experimental results (Run # 21)

	$d_p \times 10^2$ (m)	$T_p$ (K)	$R_c \times 10^4$ (kg/m <sup>2</sup> s)	$\phi$	Sh
dilute phase	.957	1258	48.5	.52	13.16
	.871	1256	45.6	.54	10.80
	.783	1258	46.6	.54	9.98
	.721	1260	46.4	.55	8.90
	.657	1256	46.1	.56	7.95
	.587	1266	50.2	.55	7.96
	.514	1266	46.5	.58	6.09
	.436	1268	50.5	.56	5.86
	.348	1268	50.9	.55	4.75
	dense phase	.976	1234	35.5	.53
.890		1237	35.6	.55	8.49
.846		1239	34.6	.58	7.39
.705		1246	35.2	.58	6.37
.656		1241	35.9	.57	6.14
.604		1241	36.6	.57	5.74
.551		1241	34.3	.59	4.77
.486		1241	37.5	.55	4.91
.400		1241	39.8	.51	4.51
.313		1241	39.5	.53	3.50

Table A.22 Experimental results (Run # 22)

	$d_p \times 10^2$ (m)	$T_p$ (K)	$R_c \times 10^4$ (kg/m <sup>2</sup> s)	$\phi$	Sh
dilute phase	.969	1246	43.6	.51	12.30
	.908	1248	42.6	.53	10.84
	.853	1253	44.6	.54	10.56
	.733	1253	43.8	.54	8.76
	.671	1261	46.6	.56	8.31
	.604	1261	46.1	.56	7.36
	.535	1268	47.0	.59	6.35
	.464	1266	43.4	.61	4.88
	.384	1273	51.4	.57	5.11
	.293	1263	47.0	.56	3.63
dense phase	.971	1238	42.3	.47	12.85
	.852	1252	43.9	.50	11.10
	.794	1255	46.2	.53	10.27
	.734	1255	42.9	.56	8.32
	.600	1260	46.8	.55	7.57
	.528	1265	48.7	.56	6.84
	.451	1261	47.6	.55	5.81
	.369	1268	48.7	.57	4.66
	.287	1268	40.0	.53	3.21

Table A.23 Experimental results (Run # 23)

	$d_p \times 10^2$ (m)	$T_p$ (K)	$R_c \times 10^4$ (kg/m <sup>2</sup> s)	$\phi$	Sh
dilute phase	.963	1283	58.6	.57	14.85
	.915	1283	59.0	.56	14.27
	.866	1288	57.8	.59	12.50
	.815	1298	61.8	.61	12.26
	.761	1293	61.5	.59	11.76
	.645	1308	63.4	.64	9.47
	.585	1305	60.9	.64	8.22
	.520	1313	68.0	.63	8.27
	.446	1328	69.5	.68	6.76
	.365	1338	73.5	.69	5.72
dense phase	.954	1228	35.3	.51	9.88
	.896	1228	35.4	.51	9.19
	.835	1233	36.6	.52	8.76
	.773	1233	34.9	.54	7.40
	.646	1233	35.9	.54	6.68
	.610	1243	37.1	.57	5.95
	.536	1238	36.9	.54	5.42
	.454	1243	41.2	.52	5.37
	.362	1238	39.5	.51	4.16

Table A.24 Experimental results (Run # 24)

	$d_p \times 10^2$ (m)	$T_p$ (K)	$R_c \times 10^4$ (kg/m <sup>2</sup> s)	$\phi$	Sh
dilute phase	.972	1273	50.8	.58	12.65
	.907	1273	52.2	.57	12.40
	.841	1273	52.0	.57	11.42
	.771	1278	54.6	.57	10.96
	.700	1278	51.7	.59	9.06
	.626	1283	54.1	.60	8.46
	.547	1283	53.0	.61	7.08
	.459	1291	58.9	.60	6.68
	.357	1298	59.6	.62	5.06
	dense phase	.953	1248	40.5	.55
.902		1248	41.2	.55	10.10
.851		1248	40.5	.55	9.26
.768		1255	42.2	.57	8.74
.741		1255	42.4	.57	8.20
.683		1255	43.5	.56	7.92
.619		1260	46.7	.55	7.80
.548		1265	49.4	.55	7.27
.471		1265	49.6	.55	6.31
.379		1275	58.3	.53	6.22

Table A.25 Experimental results (Run # 25)

	$d_p \times 10^2$ (m)	$T_p$ (K)	$R_c \times 10^4$ (kg/m <sup>2</sup> s)	$\phi$	Sh
dilute phase	.965	1262	48.6	.54	12.79
	.906	1266	47.1	.58	10.98
	.849	1266	43.8	.61	9.09
	.792	1266	44.5	.67	8.71
	.732	1269	46.6	.60	8.35
	.666	1273	49.1	.59	8.20
	.593	1273	51.2	.58	7.83
	.514	1276	54.3	.56	7.33
	.426	1276	54.5	.56	6.12
	.365	1276	55.2	.56	4.85
	dense phase	.956	1253	47.6	.50
.899		1258	45.7	.55	11.06
.841		1258	46.0	.55	10.50
.782		1258	44.3	.56	9.13
.722		1262	46.2	.57	8.76
.657		1264	47.8	.56	8.30
.587		1268	48.6	.57	7.36
.511		1268	51.9	.54	7.22
.426		1268	52.2	.54	6.20
.331		1268	55.6	.56	5.34

Table A.26 Experimental results (Run # 26)

	$d_p \times 10^2$ (m)	$T_p$ (K)	$R_c \times 10^4$ (kg/m <sup>2</sup> s)	$\phi$	Sh	
dilute phase	.989	1308	70.4	.60	17.20	
	.932	1320	68.8	.66	14.50	
	.878	1313	63.1	.66	12.44	
	.823	1320	66.8	.67	12.25	
	.764	1326	68.4	.68	12.41	
	.703	1333	67.0	.71	9.88	
	.649	1338	66.0	.73	8.65	
	.574	1343	70.6	.72	8.34	
	.503	1346	69.6	.73	7.07	
	.428	1355	68.3	.76	5.71	
	.341	1363	79.8	.74	5.45	
	dense phase	.972	1240	41.8	.49	12.22
		.906	1240	39.1	.53	10.00
.839		1240	40.0	.52	9.68	
.767		1240	42.5	.48	9.99	
.681		1244	42.5	.51	8.46	
.527		1248	42.2	.53	6.27	
.407		1248	42.6	.53	5.20	
.327		1270	50.9	.56	4.38	

Table A.27 Experimental results (Run # 27)

	$d_p \times 10^2$ (m)	$T_p$ (K)	$R_c \times 10^4$ (kg/m <sup>2</sup> s)	$\phi$	Sh
dilute phase	.932	1273	54.3	.55	13.82
	.874	1273	55.2	.54	13.20
	.805	1278	52.0	.59	10.50
	.735	1275	53.9	.56	10.50
	.659	1280	55.8	.57	9.56
	.579	1288	55.4	.61	7.79
	.491	1288	59.3	.58	7.40
	.391	1293	61.2	.59	6.00
dense phase	.960	1262	53.0	.50	15.05
	.878	1262	52.7	.50	13.61
	.832	1262	50.4	.53	11.80
	.765	1263	52.3	.51	11.68
	.693	1268	53.3	.53	10.29
	.617	1271	54.7	.54	9.26
	.535	1274	54.7	.56	7.83
	.448	1275	55.7	.55	6.70
	.350	1280	57.9	.56	5.40

Table A.28 Experimental results (Run # 28)

	$d_p \times 10^2$ (m)	$T_p$ (K)	$R_c \times 10^4$ (kg/m <sup>2</sup> s)	$\phi$	Sh
dilute phase	.950	1313	53.7	.71	10.64
	.906	1313	54.7	.71	10.42
	.860	1313	55.1	.70	10.00
	.813	1313	54.4	.71	9.27
	.766	1316	53.5	.72	8.44
	.720	1323	49.4	.76	6.95
	.659	1336	54.6	.77	6.86
	.581	1353	54.5	.80	5.84
	.496	1353	55.7	.80	5.12
	.399	1353	62.4	.78	4.76
	dense phase	.972	1230	26.3	.64
.932		1133	23.5	.69	4.72
.891		1239	20.7	.75	3.68
.838		1239	24.9	.69	4.31
.779		1239	20.0	.75	3.07
.723		1243	21.8	.75	3.14
.663		1243	21.4	.75	2.80
.600		1245	22.7	.74	2.73
.533		1247	22.6	.75	2.32
.455		1253	22.9	.72	2.52

Table A.29 Experimental results (Run # 29)

	$d_p \times 10^2$ (m)	$T_p$ (K)	$R_c \times 10^4$ (kg/m <sup>2</sup> s)	$\phi$	Sh
dilute phase	.922	1276	40.9	.67	8.34
	.853	1276	41.2	.67	7.80
	.782	1278	41.0	.68	7.02
	.708	1278	41.4	.67	6.67
	.628	1283	43.1	.68	5.91
	.542	1288	44.0	.69	5.12
	.442	1293	50.1	.67	4.94
	.321	1293	53.7	.64	3.57
dense phase	.965	1246	31.3	.65	6.93
	.915	1246	30.5	.66	6.32
	.864	1248	30.8	.66	5.98
	.811	1248	31.5	.65	5.82
	.756	1256	31.2	.67	5.23
	.696	1253	34.0	.65	5.45
	.633	1253	34.1	.65	4.96
	.566	1253	34.2	.64	4.47
	.493	1255	36.9	.62	4.32
	.406	1260	42.4	.59	4.31

## **REFERENCES**

References

1. Wen, C.Y., Krishinan, R., and Kalyanaraman, R., "particle Mixing near the Grid Region of Fluidized Beds," Fluidization, Grace, Matson (Ed.), Plenum Press, New York (1980).
2. Cook., M.J., Harris, W., Highly, J., and Williams, D.F., Tripartite Chem. Eng. Conf. Symp. on Fluidization I, P. 14, Montral (1968).
3. Cole, W.E., and Essenhigh, R.H., Proc. Third Intern. Conference on Fluidized bed Combustion, P. II-5-1, Ohio (1973).
4. Rowe, P.N., MacGillivray, H.J., and Cheesman, D.J., "Gas Discharge from an Orifice into a Fluidized Bed," Trans. I. Chem. E., 57, 194 (1979).
5. Avedesian, M.M., and Davidson, J.F., "Combustion of Carbon Particles in a Fluidized Bed," Trans. Intstn. Chem. Eng., 51, 121 (1973).
6. Ross, I.B., and Davidson, J.F., "The Combustion of Carbon Particles in a Fluidized Bed," Trans. I. Chem E., 60, 108 (1982).
7. La Nauze, R.D., and Jung, K., "The Kinetics of Combustion of Petroleum Coke Particles in a Fluidized-Bed Combustor," 19th Symp. (int.) Combustion, pp. 1087-1092, Pittsburg, (1982).
8. La Nauze, R.D., Jung, K., and Kastl, J., "Mass Transfer to Larger Particles in Fluidized Beds of Smaller Particles," Chem. Eng. Sci., 39, 1623, (1984).
9. Prins, W., Casteleijn, T.P., Draijer, W., and Van Swaaij, W.P.M., "Mass Transfer from a Freely Moving Single Sphere to the Dense Phase of a Gas Fluidized Bed of Inert Particles," Chem. Eng. Sci., 40, 481 (1985).
10. Horio, M., and Wen, C.Y., "Simulation of Fluidized Bed Combustors: Part I. Combustion Efficiency and Temperature Profile," AIChE Symp. Ser., 74, No. 176, 101 (1978).
11. Saxena, S.C., and Rehmat, A., 6th Int Conf. Fluidized Bed Combustion, Atlanta, Georgia, Vol. III, 1138-1149 (1980).
12. Bosov, V., Markhevka, T.K., Melik-Akhazarov, T.K., and Orochko, D.I., "Investigation of the Structure of a Nonuniform Fluidized Bed," Intern. Chem. Eng., 9, 263 (1969).
13. Behie, L.A., and Kehoe, P., "The Grid Region in a Fluidized Bed Reactor," AIChE J., 19, 1070 (1973).
14. Merry, J.M.D., "Fluid and Particle Entrainment into Vertical Jets in Fluidized Beds," AIChE J., 21, 507 (1975).

15. Oki, K., Ishida, M., and Shirai, T., "The Behavior of Jets and Particles near the Gas Distributor Grid in a Three Dimensional Fluidized Bed," Fluidization, Grace, Mastten (Eds), Plenum Press, New York (1980).
16. Wen, C.Y., Deole, N.R., and Chen, L.H., "A Study of Jets in a Three-Dimensional Gas Fluidized Bed, " Powder Technol., 31, 175 (1982).
17. Massimila, L., Fluidization, Davidson, Harrison, Clift (Eds.), 2nd Ed., Academic Press, London (1985).
18. Yates, J.G., Rowe, P.N., and Cheeseman, D.J., "Gas Entry Effects in Fluidized Bed Reactors," AIChE J., 30, 890 (1984).
19. Davidson, J.F., and Harrison, D., Fluidized Particles, Cambridge University Press, Cambridge (1963).
20. Ghadiri, M., and Clift, R., "Jet Penetration into a Fluidized Bed at High Temperatures, " Ind. Eng. Chem. Fundam., 19, 440 (1980).
21. Yang, W.C., and Keairns, D.L., "Design and Operating Parameters for a Fluidized Bed Agglomerating Combustor/Gasifier," Fluidization, Davidson, Keairns (Eds.), Cambridge University Press, 208 (1978).
22. Wen, C.Y., Horio, M., Krishnan, R., and Rengarajan, P., Proceedings of the Second Pacific Chemical Engineering Conf., AIChE, P. 1182, New York (1977).
23. Song, J.C., Yutani, N., and Fan, L.T., "Transient Axial Solid and Gas Temperature Profiles in the Grid Zone of a Gas-Solid Fluidized Bed," Ind. Eng. Chem. Fundam., 23, 170 (1984).
24. Zenz, F.A., Fluidization, Davidson, Harrison (Eds.), Academic Press, London and New York (1971).
25. Filla, M., Massimilla, L., and Vaccaro, S., "Gas Jets in Fluidized Beds and Spouts: A Comparison of Experimental Behavior and Models," Can. J. Chem. Eng., 61, 370 (1983).
26. Hirato, M., Miyamoto, T., Tomuro, J., Yoshioka, S., Kiuch, N., and Ishibashi, Y., "Behavior of Particles and Bubbles in the Fluidized Bed," Fluidization (Science and Technology), Kwauk, Kunii (Eds.), Science Press, Beijing (1982).
27. Ishida, M., Hatano, H., and Sugawara, T., "The Behavior of Gas and Particles around a Nozzle in a three Dimensional Fluidized Bed," Fluidization (Science and Technology), Kwauk, Kunii (Eds.), Science Press, Beijing (1982).

28. Behie, L.A., "Momentum, Heat and Mass transfer from a Grid Jet in a Large Gas Fluidized Bed," Ph.D. dissertation, Univ. Western Ontario, London, Canada (1972).
29. Kunii, D., "Importance of Dispersed Solids in Bubbles for Exothermic Reactions," AICHE Symposium Ser., 69, No. 128, 24 (1974).
30. Grace, J.R., and De Lasa, H.I., "Reaction Near the Grid in Fluidized Beds," AICHE J., 24, 364 (1978).
31. Yang, X., Horne, D.G., Yates, J.G., and Rowe, P.N., "Distributor-Zone Reactions in a Gas-Fluidized Bed," AICHE Symposium Ser., 80, No. 241,41 (1985).
32. Patrose, B., and Caram, H.S., "A Grid Jet in a Fluidized Bed Combustor," Presented at 76th Annual AIChE Meeting, San Francisco, CA, November (1984).
33. Ranz, W.E., and Marshall, W.R., Jr., "Evaporation from Drops," Chem. Eng. Prog., 48, 141 (1952).
34. La Nauze, R.D., "Fundamentals of Coal Combustion in Fluidized Beds," Chem. Eng. Res. Des., 63, 3 (1985).
35. Laurendeau, N.M., "Heterogenous Kinetics of Coal Char Gasification and Combustion," Prog. Energy Combust. Sci., 4, 221 (1978).
36. Howard, J.B., Williams, G.C., and Fine, D.H., "Kinetics of Carbonmonoxide Oxidation in Postflame gases," Proceedings of the 14th International Symposium on Combustion, pp 975-986 (1972).
37. Caram, H.S., and Amundson, N.R., "Diffusion and Reaction in a Stagnant Boundary Layer about a Carbon Particle," Ind. Eng. Chem. Fund., 16, 171 (1977).
38. Basu, P.J., Broughton, J., and Elliott, D.E., "Combustion of Single Coal Particles in Fluidized Beds," Inst. Fuel Symp. Ser., 1, A3.1 (1975).
39. Ross, I.B., Patel, M.S., and Davidson, J.F., "The Temperature of Burning Carbon Particles in Fluidized Beds," Trans. I. Chem. E., 59, 83 (1981).
40. Tomczek, J. and Remarczyk, L., "The mode of Combustion of Coal in a Fluidized Bed," Can. J. Chem. E., 64, 871 (1986).
41. Smith, I.W., "The Intrinsic Reactivity of Carbons to Oxygen," Fuel, 57, 409 (1978).
42. Smith, I.W., "The Combustion Rates of Coal Chars: A Review," 19th Symp. (Int.) on Combustion, The Combustion Institute, pp. 1045-1065 (1982).

43. Knowlton, T.M., and Hirsan, I., "The Effect of Pressure on Jet Penetration in Semi-Cylindrical Gas-Fluidized Beds," Fluidization, Grace, Matsen (Eds.), Plenum Press, New York (1980).
44. Andrei, M.A., Sarofim, A.F., and Beer, J.M., "Time-Resolved Burnout of Coal Particles in a Fluidized bed," Combustion and Flame, 61, 17 (1985).
45. Basu, P., "Burning Rate of Carbon in Fluidized Beds," Fuel, 56, 390 (1977).
46. Wen, C.Y., and Yu, Y.H., "Mechanics of Fluidization," Chem. Eng. Prog. Symp. Ser., 62, 100 (1966).
47. Babu, S.P., Shah, B., and Talwalkar, A., "Fluidization Correlations for Coal Gasification Material - Minimum Fluidization Velocity and Fluidized Bed Expansion Ratio," AIChE Symp. Ser., 74, No. 176, 176 (1978).
48. Richardson, J.F., and Da St. Jeronimo, M.A., Chem. Eng. Sci., 34, 1419 (1979).
49. Zheng, Z.X., Yamazaki, R., and Jimbo, G., Kagaku Kogaku Ronbunshu, 11, 115 (1985).
50. Bin, A.K., "Minimum Fluidization Velocity at Elevated Temperatures and Pressures," Can. J. Chem. Eng., 64, 854 (1986).
51. Ergun, S., "Fluid Flow through Packed Columns," Chem. Eng. Prog. 48 (2), 89 (1952).
52. Stubington, J.F., Barrett, D., and Lowry, G., "On the minimum fluidizing velocity of coal-derived chars at elevated temperatures," Chem Eng. Sci., 39, 1516 (1984).
53. Mathur, A., Saxena, S.C., and Zhang, Z.F., "Hydrodynamic Characteristics of Gas-Fluidized Beds over a Broad Temperature Range," Powder Technol., 47, 247 (1986).
54. Field, M.A., Gill, D.W., Morgan, B.B., Hawksley, P.G.W., "Combustion of Pulverized Coal," BCURA, Leatherhead, England (1967).
55. Zenz, F.A., Inst. Chem. Eng. Symp. Ser., 30, 136 (1968).
56. Lefroy, G.A., and Davidson, J.F., "The Mechanics of Spouted Beds," Trans. I. Chem. E., 47, T120 (1969).
57. Fakhimi, S., Sohrabi, S., and Harrison, D., "Entrance Effects at a Multi-Orifice Distributor in Gas-Fluidized Beds," Can. J. Chem. Eng., 61, 364 (1983).

58. Tamarin, A.I., "Mass Transfer between the Gas and Solid Particles in a Fluidized Bed," J. Eng. Phys., 41, 1346 (1981).
59. Guedes De Carvalho, J.R.F., and Coelho, M.A.N., "Comments on Mass Transfer to Large Particles in Fluidized Beds of Smaller Particles," Chem. Eng. Sci., 41, 209 (1986).
60. Nishimura, Y., and Ishii, T., "An analysis of Transport Phenomena of Multi-Solid Particle Systems at Higher Reynolds Numbers by a Standard Karman-Pohlhausen method - II Mass Transfer," Chem. Eng. Sci., 35, 1205 (1980).
61. Kunii, D., and Suzuki, M., "Particle -to-Fluid Heat and Mass Transfer in Packed Beds of Fine Particles," Int. J. Heat Mass Transfer, 10, 845 (1967).
62. Bar-Ilan, M., and Resniek, W., "Gas Phase Mass Transfer in Fixed Beds at Low Reynolds Numbers," Ind. Eng. Chem., 49, 313 (1957).
63. Nelson, P.A., and Galloway T.R., "Particle-to-Fluid Heat and Mass Transfer in Dense Systems of Fine Particles," Chem. Eng. Sci., 30, 1 (1975).
64. Pfeffer, R., and Happel, J., "An Analytical Study of Heat and Mass Transfer in Multiparticle Systems at Low Reynolds Numbers," AIChE J., 10, 605 (1964).
65. Nishimura, Y., and Ishii, T., "An Analysis of Transport Phenomena for Multi-Solid Particle Systems at Higher Reynolds Numbers by a Standard Karman-Pohlhausen Method - I, Momentum Transfer," Chem. Eng. Sci., 35, 1195 (1980).
66. Basu, p., "The Effect of Radial Distribution of Voidage on the Burning Rate of a Carbon Sphere in a Fluidized Bed," Chem. Eng. Commun., 39, 297 (1985).
67. Whitaker, S., "Forced Convection Heat Transfer Correlations for Flow in Physics, Past Flat Plates, Single Cylinders, Simple Species, and for Flow in Packed Bed and Tube Bundles," AIChE J., 18, 361 (1972).
68. Morgan, III, M.H., Day, J.Y., and Littman, H., "Spout Voidage Distribution, Stability and Particle Circulation Rates in Spouted Beds of Coarse Particles-I. Theory," Chem. Eng. Sci., 40, 1367 (1985).
69. Mamuro, T., and Hattori, H., "Flow Pattern of Fluid in Spouted Beds," J. Chem. Eng. Japan, 1, 1 (1968); correction, J. Chem. Eng. Japan, 3, 119 (1970).

70. Epstein, N., Lim, C.J., and Mathur, K.B., "Data and Models for Flow Distribution and Pressure Drop in Spouted Beds," Can. J. Chem. Eng., 56, 436 (1978).
71. Epstein, N., and Levine, S., "Non-Darcy Flow and Pressure Distribution in a Spouted Bed," Proc. Second Eng. Foundation Conf. on Fluidization, p.98, Cambridge Univ. Press, (1978).
72. Richardson, J.F., and Jeronimo, M.A. da S., "Velocity - Voidage Relations for Sedimentation and Fluidization," Chem. Eng. Sci., 34, 1419 (1979).
73. Yokogawa, A., Ogino, E., and Yoshii, N., Trans. Japan Soc. Mech. Engrs., 38, 148 (1972).
74. Grbarčić, Z.B., Vuković, D.V., Zdanski, F.K., and Littman, H., "Fluid Flow Pattern, Minimum Spouting Velocity and Pressure Drop in Spouted Beds," Can. J. Chem. Eng., 54, 33 (1976).
75. Horio, M., Kiyota, H., and Muchi, I., "Particle Movement on a Perforated Plate Distributor of Fluidized Bed," J. Chem. Eng. Japan, 13, 137 (1980).
76. Graca, J.R., and Lim, C.J., "Permanent Jet Formation in Beds of Particulate Solids," Can. J. Chem. Eng., 65, 160 (1987).
77. Quereshi, A.E., and Creasy, D.E., "Fluidized Bed Gas Distributors," Powder Technol., 22, 113 (1979).
78. Geldart, D., and Baeyens, J., "The Design of Distributors for Gas-Fluidized Beds," Powder Technol., 42, 67 (1985).
79. Kunii, D., and Levenspiel, O., Fluidization Engineering, p76, John Wiley & Sons, Inc., (1969).
80. Fujita, S., Kagaku Kogaku, 28, 251 (1964).

MICHIGAN STATE UNIV. LIBRARIES



31293000540843